Nonlinear Spectroscopy of Solids at THz Frequencies

Author: **Soheil Zibod**

Supervised by: Prof. Ksenia Dolgaleva

Thesis submitted to the University of Ottawa in partial fulfillment
of the requirements for the degree of Doctor of Philosophy

School of Electrical Engineering and Computer Science
Faculty of Engineering
University of Ottawa

To my mom,

the symbol of love and dedication

ACKNOWLEDGMENTS

I would like to express my utmost gratitude to my supervisor Prof. Ksenia Dolgaleva for providing me with the opportunity to do my research under her supervision. Her constructive comments and suggestions were always helpful towards my progress. I will always appreciate her unwavering support and patience.

I am very thankful to Prof. Robert Boyd for his guidance and insightful comments. I found his comments and suggestions extremely helpful in different stages of my work.

I would like to thank Prof, Jean-Michel Ménard for his valuable inputs to the projects and during review process.

I also would like to thank my former colleague and friend, Dr. Payman Rasekh for building the intense THz setup and training me on the experimental setup and measurements. His useful comments and helps were instrumental to the progress of this work.

Furthermore, I would like to thank Dr. Murat Yildirim, whom I also had a brief collaboration at the beginning of my PhD. projects, and Dr. Mikko J. Huttunen for their significant contribution to this project before I joined this research group.

Also, I would like to express my appreciation to my friend and former colleague , Dr. Mohammad Karimi, for the countless interesting discussions and help. Furthermore, I would like to thank my fellow teammates, Sina Aghili, Rania Mahjoub, and Athulya Thulaseedharan, for all the great support.

I am grateful to my friend of 20 years, Dr. Mehran Sadeghi for his support and all these great years of friendship. Furthermore, I would like to thank my good friend and colleague, Neda Boroumand for all the support and interesting discussions.

Last but foremost, I am extremely grateful to my family. My mom for her ultimate love and sacrifice. My dad for his great encouragement. My middle brother, Sina, for all the support and love and positiveness. And my oldest brother, Roozbeh, for all the support, encouragement and his great interest in my work and his passion for engineering.

ABSTRACT

This doctoral dissertation focuses on the nonlinear spectroscopy of solids at terahertz frequencies. In this study, the nonlinear propagation of broadband terahertz (THz) pulses through solids is theoretically and experimentally investigated.

The experimental observation of a very strong nonlinear response in crystalline quartz in the THz frequency region through THz time-domain spectroscopy (THz-TDS) is reported. A previously developed theoretical model, describing the nonlinear optical interactions, is modified and predicts a very large nonlinear refractive index equal to $5.17 \times 10^{-14}\ \mathrm{m}^2\ \mathrm{W}^{-1}$. The frequency analysis of the time-domain response reveals a nonlinear refractive index on the order of $10^{-13}\ \mathrm{m}^2\ \mathrm{W}^{-1}$ in addition to a fifth-order nonlinear susceptibility with a negative real part.

Moreover, a simple method to model the propagation of a broadband THz pulse in a nonlinear medium with a dispersion of the nonlinear refractive index is presented. This method uses a spectral solution to the wave equation based on Fourier analysis. Using the same model, an expression to extract the nonlinear refractive index dispersion for broadband sources is derived. This model factors out the dependence of the experimental data on the spectral shape of the THz pulse. Furthermore, the model takes the effect of the absorption spectral profile of the material into account. As the next step, the proposed method is applied on the experimental data from the nonlinear spectroscopy of BK7 glass. In addition to its high value of the nonlinear Kerr coefficient equal to $4 \times 10^{-14}\ \mathrm{m}^2\ \mathrm{W}^{-1}$, BK7 glass is of a great interest due to its absorption profile unique to the borosilicate glass family.

Finally, a theoretical study on the relationship between the THz nonlinear refractive index and the THz-induced third-order susceptibility sensed by the optical probe is presented. This analysis explains the scaling factor in the translation of the THz nonlinear refractive index to the optical regime in the phenomena such as terahertz-induced Kerr effect in optical probe setups and terahertz field-induced second-harmonic (TFISH) generation, which is of a great importance for the measurement consistency in different frequency regions.

List of Publications

- **S. Zibod**, P. Rasekh, M. Yildrim, W. Cui, R. Bhardwaj, J.-M. Ménard, R. W. Boyd, and K. Dolgaleva, “Strong nonlinear response in crystalline quartz at thz frequencies,” Advanced Optical Materials, vol. 11, no. 15, p. 2202343, 2023.

  Contribution: Measurements, data analysis, theoretical modeling and writing the manuscript.

  ** Dr. Payman Rasekh had a pivotal role in this project by developing the intense THz setup and also training me on the experimental works.

- **S. Zibod**, R. Bhardwaj, J.-M. Ménard, R. W. Boyd, and K. Dolgaleva, “Broadband THz Pulse Propagation in Nonlinear Medium: Dispersion of The Nonlinear Refractive Index,” 2024, (Manuscript under preparation).

  Contribution: Measurements, data analysis, theoretical modeling and writing the manuscript.

- B. Zhou, M. Rasmussen, **S. Zibod**, S. Yan, N. Noori, O. Nagy, Y. Ding, S. Lange, K. Dolgaleva, R. Boyd, and P. Uhd Jepsen, “Measurement of the dispersion of $\chi(3)$ of SiO2 and SiN across the THz and far-infrared frequency bands,” Laser and Photonics Reviews, Jul 2024

  Contribution: Theoretical modeling and writing the corresponding part in the manuscript.

- F. Blanchard, J. E. Nkeck, L. Guiramand, **S. Zibod**, K. Dolgaleva, T. Arikawa, and K. Tanaka, “Two-dimensional space–time terahertz memory in bulk srtio3,” Optica, vol. 9, pp. 980–986, Sep 2022.

Contribution: Studying the molecular dynamics of STO, answering the reviewer comments and writing the part about the crystallography and the response of different crystals.

TABLE OF CONTENTS

APPENDIX

LIST OF TABLES

LIST OF FIGURES

Chapter 1

INTRODUCTION

Terahertz (THz) frequency range is the electromagnetic spectrum window located between far-infrared and microwave frequency ranges. It is associated with the frequency range of 0.1 THz to 10 THz, corresponding to the wavelength range of 3 mm to 30 microns, as shown in Fig. 1.1.

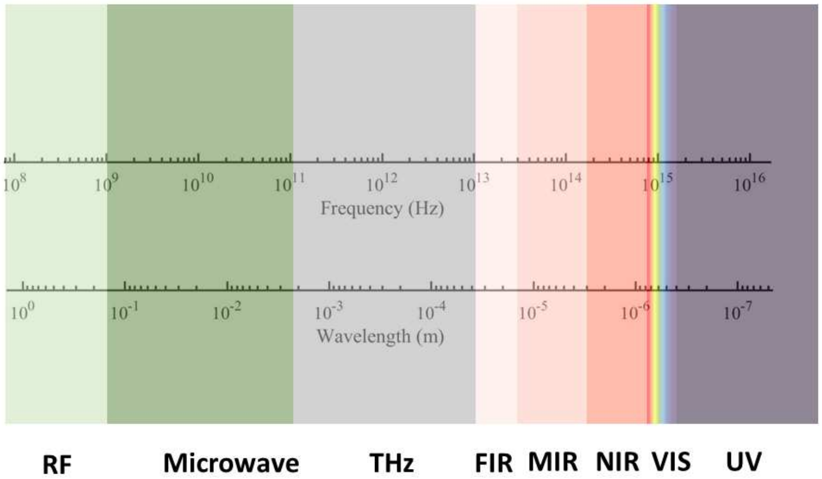

Figure 1.1: THz band in electromagnetic spectrum.

Thanks to certain properties of the THz waves such as low photon energy, transparency to most dielectrics and the strong absorption in molecules such as water, it has different applications in non-destructive testing of biological tissues, security and inspection of pharmaceutical and agricultural products [1, 2, 3, 4, 5]. Despite inheriting some of its features from microwave and optical ranges, THz waves do not fit into either of the two categories [6]. For instance, microwave frequencies are usually generated through oscillations of carriers in electrical components, though traditional radio frequency sources cannot exceed several hundreds of GHz. On the other hand, light is usually emitted through the excitation of electrons to higher energy states and their relaxation to lower states. However, at the THz frequency range, the photon energy is smaller than the thermal energy at the room temperature, and it is indistinguishable from thermal relaxation. Thus, it requires unique techniques for both generation and detection.

1.1 **THz Generation Techniques**

There are three main techniques for generating THz waves. The first one is THz generation based on illuminating a DC-biased photoconductive (PC) antenna by a laser beam, as shown in Fig. 1.2. The ultrashort laser pulse hits the semiconductor area beneath the antenna gap and excites the electrons to the conduction band, where they are accelerated via a bias field before recombination. This photocurrent in turn emits electromagnetic radiation with a duration of a few hundred femtoseconds to a few picoseconds, depending on the characteristic recombination rate of the substrate [7, 8, 9]. The most common semiconductor used for PC antenna is GaAs, where the combination of high carrier mobility and and short carrier lifetime enable a strong and wideband THz emission, though the THz bandwidth is limited by the phonon resonances at 8.5 THz [10].

The second technique is THz generation inside the plasma, as depicted in Fig. 1.3. A part of the pump beam is frequency-doubled in a second-harmonic generation (SHG)

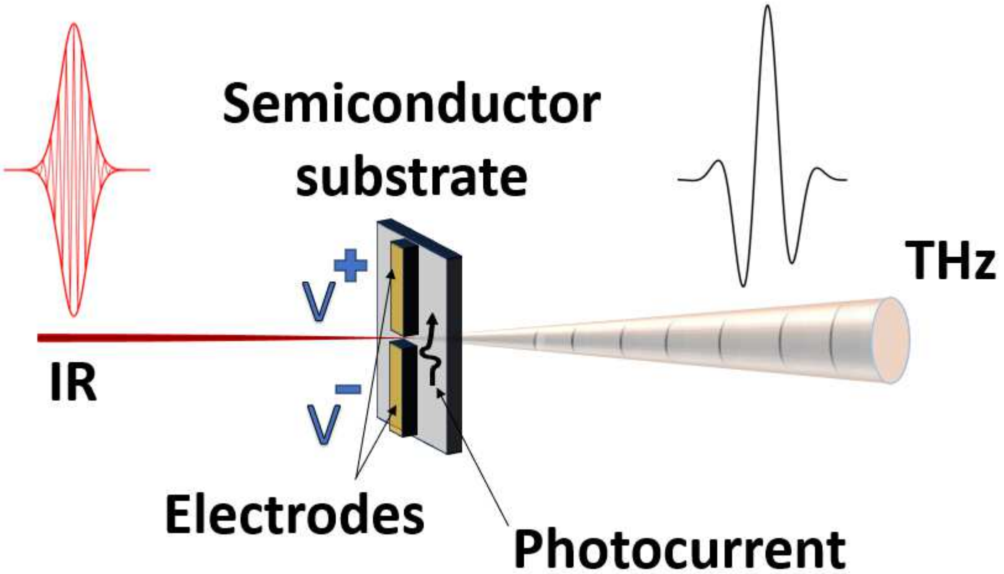

Figure 1.2: THz generation using photoconductive antenna (PCA). The semiconductor substrate is DC-biased under the two electrodes. Then, the biased region between the electrodes is illuminated with an ultrashort laser pulse. The generated electrons are accelerated in the DC field and create a current. The photocurrent radiates an electromagnetic pulse in THz region with a duration of a few hundred femtoseconds to a few picoseconds before the carrier recombination happens.

crystal. Then, the residual fundamental beam alongside the second harmonic is tightly focused to an intensity sufficient for air ionization, forming the plasma region for THz generation [11, 12]. The main mechanism behind the THz generation is the transient photocurrent of the ionizing electrons as the result of the superposition of the fundamental and second harmonic waves [13]. In this method, the THz generation is based on the four-wave mixing process of the fundamental beam and its second harmonic in the ionized plasma. The generated ultra-short THz pulse can have a bandwidth up to 150 THz [14, 15].

The third technique to generate THz radiation is through optical rectification (OR)

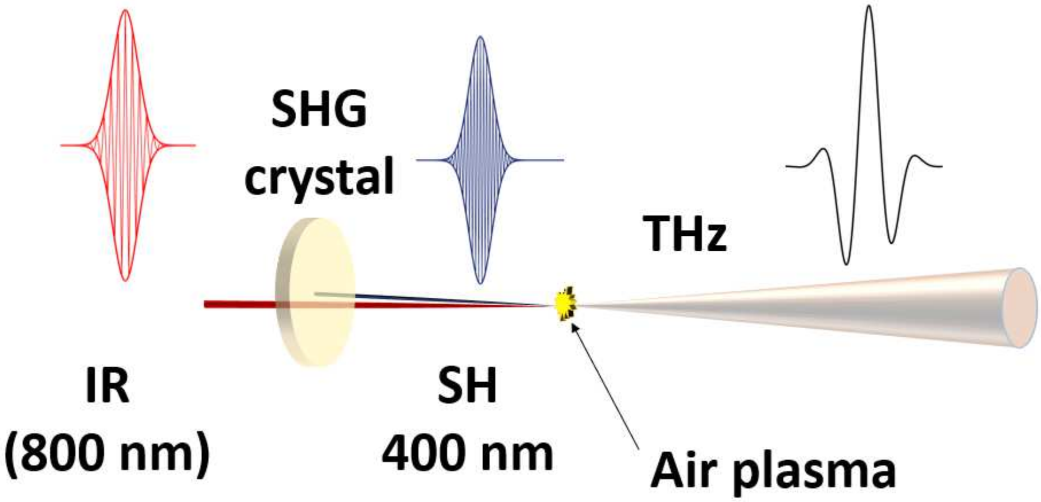

Figure 1.3: THz generation from air plasma. IR (800 nm) beam passes through an SHG crystal such as Beta Barium Borate (BBO) and generates the second harmonic (400 nm). Then, both the fundamental and second-harmonic beams are tightly focused so that the air is ionized. In the plasma, the four-wave mixing of the fundamental and second-harmonic pulses generates an elecromagnetic pulse in the THz spectrum.

in non-centrosymmetric crystals such as ZnTe, InP and GaP [6, 13, 16]. The nonlinear polarization induced by OR could be expressed as [13]

$$P_i^{(2)} = \sum_{j,k} \varepsilon_0 \chi_{i,j,k}^{(2)}(0, \omega, -\omega) E_j(\omega) E_k^*(\omega), \tag{1.1}$$

where i, j, k represent the Cartesian components of the nonlinear polarization and the driving fields. Depending on the crystal symmetry, many of the susceptibility tensor elements are zero. Consequently, the nonzero elements of the tensor determine the crystal orientation at which the intensity of the generated THz field is maximum.

To achieve an efficient nonlinear process, in this case the generation of the THz radiation as described in Eq. (1.1), the phase-matching condition should be met between the infrared (IR) driving field and the generated THz field. For the two frequency components of the IR pulse, ω_1 and ω_2, the energy and momentum conservations are given as

$$\omega_1 - \omega_2 = \Omega_{\mathrm{THz}}, \tag{1.2a}$$

$$k_1 - k_2 = k_{\mathrm{THz}}. \tag{1.2b}$$

Dividing Eq. (1.2a) by Eq. (1.2b), we obtain:

$$\frac{\omega_1 - \omega_2}{k_1 - k_2} = \frac{\Omega_{\mathrm{THz}}}{k_{\mathrm{THz}}}, \tag{1.3}$$

which means that the phase velocity of the THz field, $v_{\mathrm{ph}}^{\mathrm{THz}} = \frac{\Omega_{\mathrm{THz}}}{\mathrm{k_{THz}}}$, equals to the group velocity of the optical pulse, $v_g^{\mathrm{Opt}} = \frac{\mathrm{d}\omega_{\mathrm{Opt}}}{d\mathrm{k}_{\mathrm{Opt}}}$. This implies that, in order to achieve a field build-up, the THz field must propagate with the speed of the optical pulse envelope. For instance, for ZnTe, this condition is met at 812 nm and 1.69 THz [13]. Thus, the amplitude of the generated THz increases linearly as the THz field co-propagates with the optical beam in the crystal, as shown in Fig. 1.4. For a larger field amplitude, one may choose a generation crystal with a larger effective nonlinear coefficient than ZnTe ($d_{\mathrm{eff}} = 68.5\ \mathrm{pm/V}$), such as $\mathrm{LiNbO_3}$ with an effective coefficient of $d_{\mathrm{eff}} = 168\ \mathrm{pm/V}$ [17]. However, due to the large mismatch between the THz refractive index and optical group index, in a standard collinear geometry, the generated THz radiation propagates along a cone with an angle of $\Theta_c = \cos^{-1}\frac{v_{\mathrm{THz}}}{v_g}$, with a limited conversion efficiency. To achieve the index matching, the pulse-front tilting technique is implemented, where the intensity fronts of the pump beam are tilted after deflecting from a diffraction grating and passing through two cylindrical lenses, as shown in Fig. 1.5.

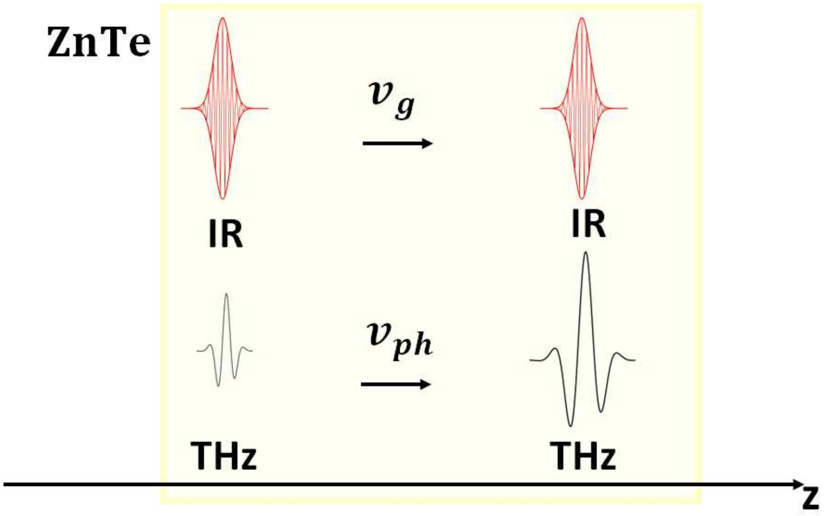

Figure 1.4: THz generation in ZnTe crystal. Phase-matching condition is achieved at 812 nm and 1.69 THz. The amplitude of the THz wave increases as it copropagates with the optical pulse.

The tilting angle γ is chosen in a way to satisfy the phase-matching condition described in Eq. (1.3): $v_g^{\text{Opt}} \cos\gamma = v_{\text{ph}}^{\text{THz}}$. In the crystal, the generated THz radiation propagates perpendicular to the tilted fronts of the optical beam and its amplitude builds up as it propagates through the crystal.The bandwidth of the THz radiation depends on the the THz absorption spectrum in the generation crystal, and on the dispersion. The THz pulse generated by optical rectification in most crystals have a bandwidth of 3 THz. However, GaP crystal enables a pulse bandwidth of up to 10 THz [18, 19]. Furthermore, it has been shown that optical rectification in organic nonlinear crystals such as diethylaminosulfur trifluoride (DAST) can generate THz pulses with a bandwidth up to 180 THz [20].

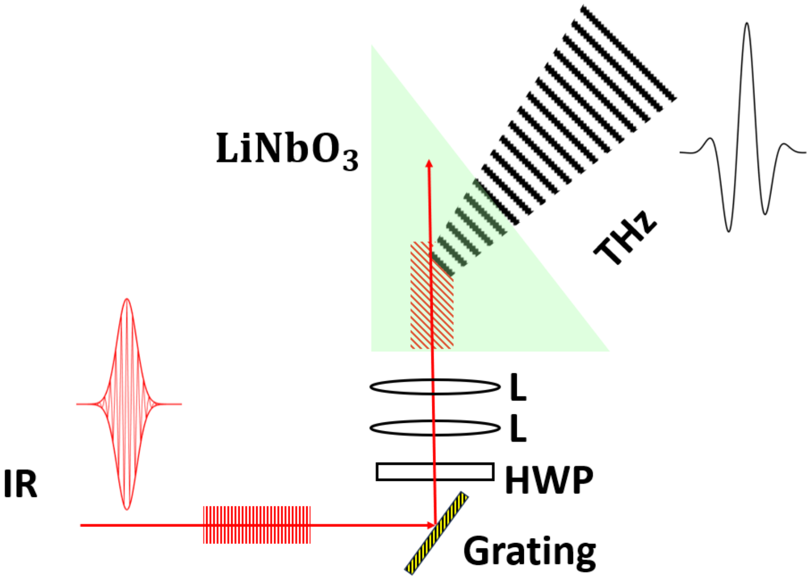

Figure 1.5: THz generation in $\mathrm{LiNbO_3}$ crystal. Phase-matching condition is achieved using pulse-front tilting technique using a grating, a half-wave plate and a pair of lenses. The tilt angle is designed to satisfy the phase match between optical pump and THz field. HWP: Half-wave plate. L: Lens

1.2 THz Detection Techniques

The three main THz detection schemes are based on mechanisms closely related to that of generation schemes. The first method is PC sampling. In this technique, the THz beam is focused on the PC antenna gap where no DC bias voltage is applied on the electrodes. A transient voltage is induced by THz pulse across the gap. Then an ultrashort optical probe pulse is also applied on the gap, co-propagates with the THz beam inside the substrate and generates carriers, as shown in Fig. 1.6. By sweeping the overlap time along the THz pulse duration via a delay stage, we can sample the THz pulse at different points of the signal by measuring the THz-induced photocurrent signal at the electrodes [7]. GaAs-based antenna has a detection bandwidth of up to 8 THz. [21].

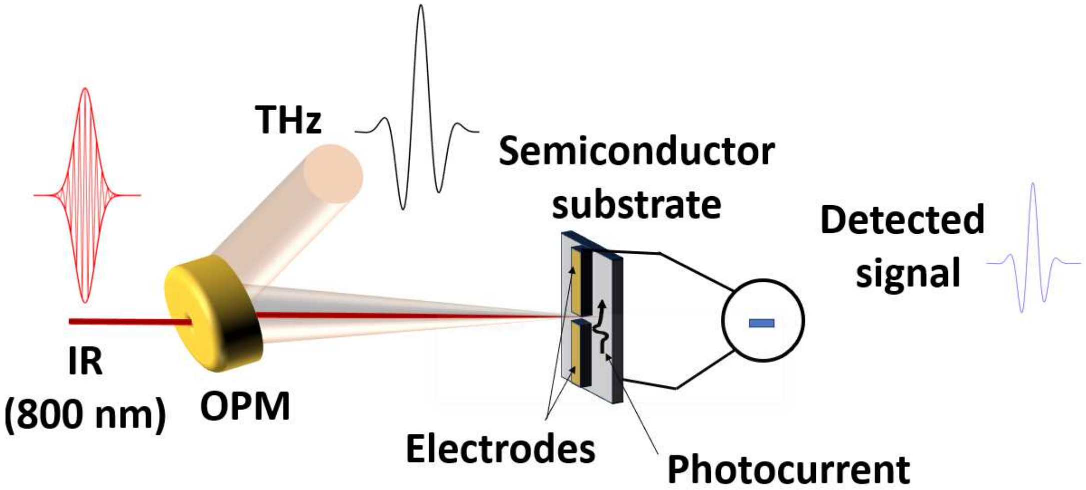

Figure 1.6: THz pulse detection based on photo-conductive sampling. The THz pulse is focused in the gap between the electrodes, where there is no bias DC voltage. An ultrashort optical pulse illuminates the gap and generates carriers. The THz field acts as the bias voltage and accelerate the carriers to create a photocurrent proportional to the THz pulse. We can sample different points of the THz temporal waveform by changing the delay between the ultrashort optical pulse and the THz pulse. Finally, the photocurrent is recorded at the electrodes. OPM: Off-axis parabolic mirror.

The second method, air-biased coherent detection (ABCD), is based on the second-harmonic generation in air plasma. In this method, the optical field is tightly focused to ionize the air and create a plasma region. As the THz pulse passes through the plasma region, the SHG of the optical beam occurs through the third-order nonlinear process between THz field and the fundamental field, as shown in Fig. 1.7. The generated second harmonic is related to the THz field as [22]:

$$E_{2\omega} \propto \chi^{(3)}_{xxxx} E_{THz} E_{\omega} E_{\omega}, \tag{1.4}$$

where, E_{ω} ,$E_{2\omega}$ $\chi^{(3)}_{xxxx}$ are, fundamental wave, second harmonic wave and third-

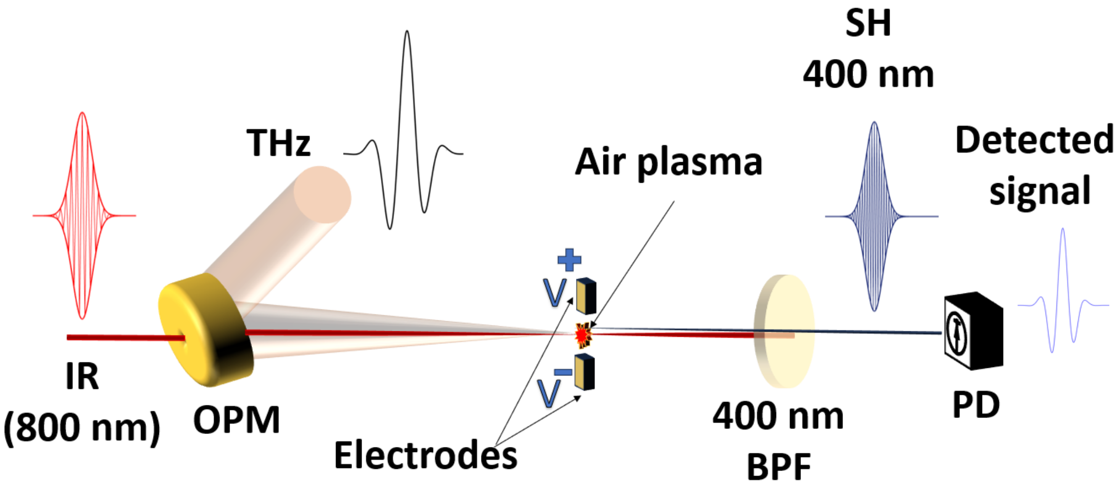

Figure 1.7: THz detection in an air-biased coherent detection (ABCD). The IR (800 nm) beam is tightly focused to create a plasma in the biased region between the electrodes. The THz pulse is also focused in the ionized region. The second harmonic (SH) (400 nm) generation happens in a FWM process where the intensity is proportional to the THz field. After the fundamental beam is filtered out with a band-pass filter, the SH intensity is measured by a photodetector. OPM: Off-axis parabolic mirror; BPF: Band-pass filter; PD: Photodetector.

order nonlinear susceptibility of the plasma, respectively. From Eq. (1.4) we can see that the intensity of the second harmonic beam is proportional to the intensity of the THz field, $I_{2\omega} \propto E^2_{\mathrm{THz}}$. It means that when the second harmonic beam is detected by the photodetector, the phase information of the THz is lost and the detection in incoherent.

For a coherent detection, an external bias voltage is introduced to the plasma area. Thus, Eq. (1.4) is modified into [22]:

$$E_{2\omega} \propto \chi^{(3)}_{xxxx}(E_{THz} + E_{bias})E_\omega E_\omega, \tag{1.5}$$

The generated second-harmonic intensity is quadratically proportional to the sum of the THz field and the bias field, $I_{2\omega} \propto (E_{THz} + E_{bias})^2$. By a proper modulation of the bias field, we can isolate the desired linear term $I_{2\omega} \propto E_{THz}E_{bias}$ from the other terms [22]. Thus, we can extract the THz field from the measured intensity. Thanks to the non-absorbing and non-dispersive medium, the generation and the detection processes with extremely large bandwidth are attainable in air plasma, and are only limited by the properties of the laser pulse [22]. The detection bandwidth of 150 THz has been reported for the ABCD method [14].

The third method of the THz pulse detection is electro-optic (EO) sampling which is based on the linear electro-optic effect in a non-centrosymmetric crystal such as ZnTe. The propagation of the THz pulse through the detection crystal causes a birefringence to a co-propogating optical pulse. This phase difference between the two polarization components is proportional to the strength of the THz field, $\Gamma \propto E_{\mathrm{THz}}$ [13]. As the optical probe beam co-propagates with the THz pulse in the detection crystal, the two perpendicular polarizations experience different phase shifts. Then, this phase difference is translated into the probe beam ellipticity after passing through the quarter-wave plate (QWP). A Wollaston prism splits the beam into its two polarizations with the intensity difference proportional to the beam ellipticity. Using the Jones matrix formalism, we have:

$$\begin{aligned}\begin{bmatrix} E_X \\ E_Y \end{bmatrix} &= \begin{bmatrix} 1 & -1 \\ -1 & 1 \end{bmatrix}\begin{bmatrix} 1 & 0 \\ 0 & j \end{bmatrix}\begin{bmatrix} e^{j\Gamma} & 0 \\ 0 & 1 \end{bmatrix}\begin{bmatrix} 1 \\ 1 \end{bmatrix} \\ &= \begin{bmatrix} (\cos(\Gamma/2) - \sin(\Gamma/2)) - j(\cos(\Gamma/2) - \sin(\Gamma/2)) \\ -(\cos(\Gamma/2) + \sin(\Gamma/2)) + j(\cos(\Gamma/2) + \sin(\Gamma/2)) \end{bmatrix}. \end{aligned} \tag{1.6}$$

Finally, the differential signal which is proportional to the THz pulse amplitude is detected using a pair of balanced photodetectors, as shown below:

$$I_Y - I_X \propto |E_Y|^2 - |E_X|^2 =$$
$$= 2\left[\left(\cos(\Gamma/2) + \sin(\Gamma/2)\right)^2 - \left(\cos(\Gamma/2) - \sin(\Gamma/2)\right)^2\right] \propto \sin(\Gamma). \quad (1.7)$$

If $|\Gamma| \ll 1$, then $\sin(\Gamma) \approx \Gamma$. This condition ensures that the detection process is linear. Thus, $I_Y - I_X \propto \Gamma \propto E_{\mathrm{THz}}$. Fig. 1.8 shows the detection scheme.

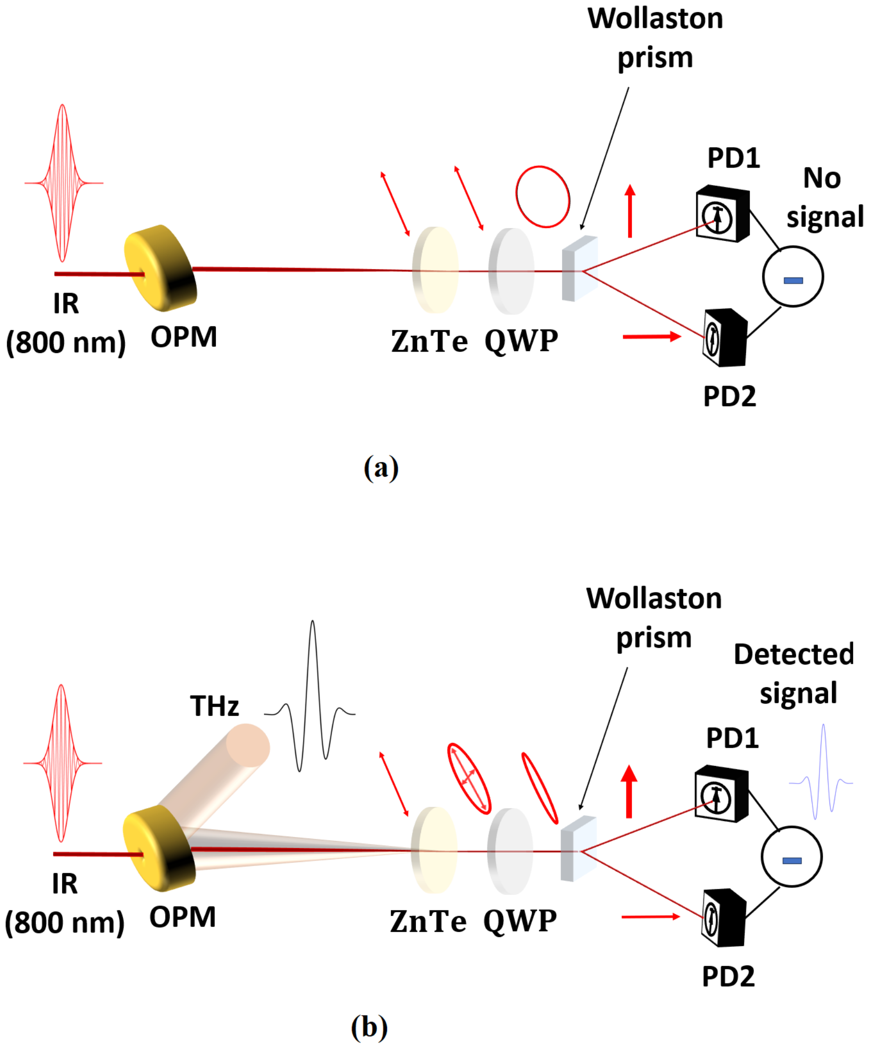

Figure 1.8: The schematic of the THz pulse detection based on electro-optic sampling. (a) Without the THz field: The linearly polarized probe beam passes through the detection crystal without sensing any birefringence. Then, via the quarter-wave plate, the linear polarization of the beam is converted to circular. Thus, the beams with the orthogonal polarizations at the output of the Wollaston prism have equal intensities, meaning that the detected signal is zero. (b) With the THz field: The presence of the THz pulse inside the detection crystal causes a birefringence. The phase difference caused by the birefringence is translated into the beam ellipticity. Thus, the beams at the output of Wollaston prism have different intensities. Thus, the THz signal which is proportional to this intensity difference is detected at the output of the balanced photodetectors. OPM: Off-axis parabolic mirror; QWP: Quarter-wave plate; PD: Photodetector.

The THz generation and detection methods and their bandwidths are summarized in Table 1.1.

THz generation technique		THz detection technique	
Technique	Bandwidth (THz)	Technique	Bandwidth (THz)
PC Antenna (GaAs)	6 [8, 9, 10]	**PC sampling** (GaAs)	8 [21]
OR		**EO sampling**	
ZnTe	3 [16]	ZnTe	4[23]
GaP	10 [19]	GaP	7 [24]
LiNbO3	3 [17, 25]		
DAST	180 [20]		
Air plasma	150 [14]	**ABCD**	150 [14]

Table 1.1: Different techniques of THz generation and detection and their respective bandwidths

1.3 **THz Nonlinear Optics**

The introduction of intense THz sources with electric field peak values as large as $1\ \mathrm{MV/cm}$ [25] using optical rectification in $\mathrm{LiNbO_3}$ has made the study of the nonlinear behaviour of materials in the THz frequency range possible.

The high intensity THz fields cause strong effects such as impact ionisation and intervalley scattering in semiconductors [26]. Thus, it can be used to study the carrier dynamics in semiconductors and consequently to develop the nonlinear terahertz metamaterials by manipulating the carrier dynamics in semiconductors [27].

Furthermore, the vibrational modes of the majority of solids and large molecules lie in

THz spectrum range [28]. The coupling between the intense THz field and these vibrational modes gives valuable information about the light matter interactions in this frequency range. Moreover, thanks to the strong THz-phonon couplings, intense THz pulses induce strong nonlinear responses in solids and liquids [29].

Finally, two-dimensional materials such as graphene, due to the Dirac electrons in their band structure, demonstrate a very large nonlinear response that is used to generate THz high-harmonics [30].

1.4 THz Time-Domain Spectroscopy

THz time-domain spectroscopy (THz-TDS) is a useful tool to characterize the optical response of different materials and distinguishing them, as several fundamental physical processes such as rotational transitions of molecules, lattice vibrational modes in solids and organic compounds and intraband transitions in semiconductors occur in this frequency range [13]. As a result, it has been used in applications such as security [31], biomedical sensing [32, 33], spectroscopy and imaging [7], and communications [34]. Furthermore, THz-TDS systems are used for monitoring production processes [35], art conservation [36], and material characterization [37]. In THz-TDS, a single-cycle THz pulse with a duration of a few picoseconds propagates through the sample. Using a very short optical pulse and sweeping it along the duration of THz pulse in the detection scheme, we are able to resolve a time-domain signal. The time-domain measurement of the real signal makes it possible to simultaneously obtain the amplitude and phase response of the sample. Thus, one can calculate the optical properties, such as refractive index and absorption coefficient, of a sample material with respect to the ref-

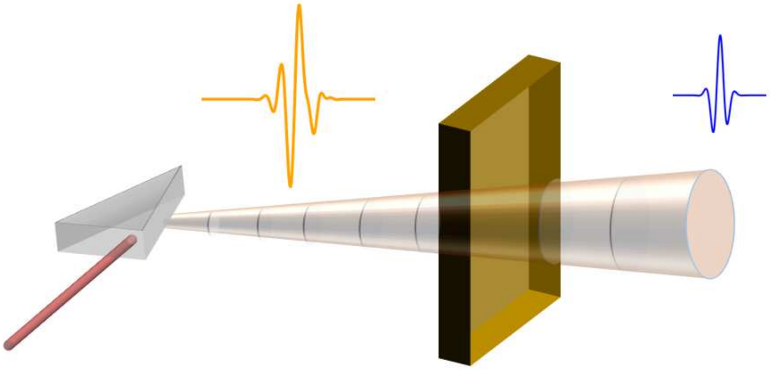

Figure 1.9: Transmission THz-TDS. As the THz field propagates through the sample, both the amplitude and temporal profile of the pulse change. Since the time-domain signal is related to the frequency domain via Fourier analysis, recording the temporal waveform of the THz pulse gives the full information about the spectral response of the sample.

erence response (e.g., of free space) [7]. Fig. (1.9) illustrates the concept of transmission THz-TDS.

1.5 THz-TDS Data Analysis

As highlighted in previous sections, THz-TDS provides the spectral response of the the material despite the fact that the THz signals are recorded in time domain. Thus, time domain and frequency domain are related to each other via Fourier transform:

$$\mathcal{F}[f(t)] = \int_{-\infty}^{\infty} f(t)e^{-j\omega t}\mathrm{d}t. \tag{1.8}$$

Fig. 1.10 illustrates the general concept of THz-TDS. The analysis could be performed for both transmission and reflection measurements, although this work focuses on the former. The input field, $E_{\text{in}}(\omega)$, is normally incident on a sample with a thickness d and a complex-valued refractive index $\tilde{n}(\omega) = n(\omega) + j\kappa(\omega)$. By applying the electromagnetic field at the interface between any two media at normal incidence, the reflected electric field and transmitted field are related to the incident field by Fresnel's coefficients [38]:

$$r = \frac{E_{r1}(\omega)}{E_{in}(\omega)} = \frac{\tilde{n}(\omega) - 1}{\tilde{n}(\omega) + 1}; \tag{1.9}$$

$$t = \frac{E_t(\omega)}{E_{in}(\omega)} = \frac{2\tilde{n}(\omega)}{\tilde{n}(\omega) + 1} = 1 + r \tag{1.10}$$

In general, Fresnel's coefficients are complex-valued; however, if the sample has a small extinction coefficient, we can use the real part of the complex refractive index to calculate the Fresnel's coefficients. From the Fig. 1.10, one can easily conclude that the input field passes through two interfaces and a propagation inside the sample before exiting the second interface. In other words, the output field is related to the input field as [7]:

$$\frac{E_{\text{out}}(\omega)}{E_{\text{in}}(\omega)} = t_{12}t_{21}e^{jn\omega d/c}e^{-\alpha d/2} = \frac{2n}{n+1} \times \frac{2}{n+1}e^{jn\omega d/c}e^{-\alpha d/2}, \tag{1.11}$$

where t_{12} and t_{21} are the transmission coefficients from medium 1 to 2 and from medium 2 to 1, respectively. In order to characterize the sample, we need to compare the output field to a known reference signal, for instance the transmitted field in the absence of any sample. The reference signal can be simply calculated from Eq. (1.11) by setting

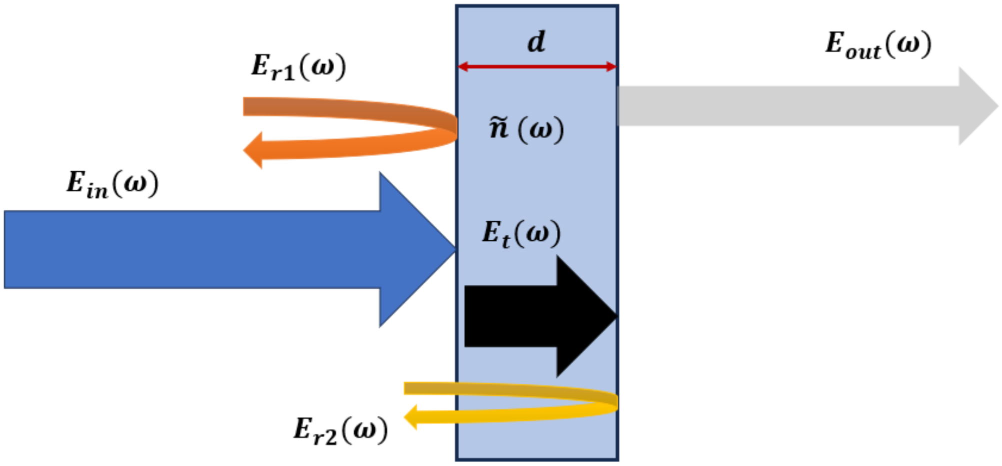

Figure 1.10: Schematic geometry of spectroscopy of a sample at normal incidence. The input field experiences two Fresnel's reflections at the interfaces before and after the propagation inside the sample before exiting the second interface.

the refractive index to 1 and the absorption to 0. Now we can characterize the material by dividing the sample signal by the reference signal. This complex-valued ratio is the spectral response of the sample:

$$\frac{E_{\text{out}}(\omega)}{E_{\text{ref}}(\omega)} = \frac{4n}{(n+1)^2} e^{j(n-1)\omega d/c} e^{-\alpha d/2} = T(\omega) e^{(j\Delta\phi)}. \tag{1.12}$$

The complex-valued response is expressed as an amplitude response multiplied by a phase response. The optical parameters of the sample could be extracted from the spectral response:

$$n(\omega) = 1 + \frac{\Delta\phi(\omega)c}{\omega d}; \tag{1.13}$$

$$\alpha(\omega) = -\frac{2}{d} \ln\left(\frac{(n+1)^2}{4n} T(\omega)\right). \tag{1.14}$$

It is useful to point out that these equations are derived with the assumption of no interference from the signal echoes caused by multiple internal reflections inside the samples, so we can safely truncate the signal without any information loss or distortion in the response. The minimum thickness that satisfies this condition is calculated as

$$\tau < 2\frac{dn}{c} \Longleftrightarrow d > \frac{c\tau}{2n}. \tag{1.15}$$

It means that, for a fixed pulse duration τ, the minimum thickness to avoid echo interference is equal to half the distance equivalent to the pulse duration inside the sample. In other words, the pulse duration should be less than the round-trip time of the light propagation inside the sample. Otherwise, the echoes interfere and overlap with a part of the main signal. This interference is called Fabry-Pérot effect. This effect needs to be dealt with properly; otherwise, there would be distortions and fluctuations in the spectral response. Eq. (1.12) needs to be modified by introducing a Fabry-Pérot correction factor, FP, calculated as [39]:

$$FP = \sum_{m=0}^{M} \left(r_{21} e^{(j\omega nd/c)} e^{-\alpha d/2} \right)^{2m}. \tag{1.16}$$

This correction factor calculates the total phase and amplitude of the first M round-trips inside the sample, including the main signal, $m = 0$. Each round-trip has two similar reflections r_{21} at the boundaries, two propagation phases and two propagation losses. Thus, Eq. (1.12) is modified as

$$\frac{E_{\text{out}}(\omega)}{E_{\text{ref}}(\omega)} = FP \times \frac{4n}{(n+1)^2} e^{j(n-1)\omega d/c} e^{-\alpha d/2} = FP \times T(\omega) e^{(j\Delta\phi)}. \tag{1.17}$$

If the scan duration is sufficiently long to cover most reflections, then $M \to \infty$. Thus, for a long scan measurement, the Fabry-Pérot coefficient is given by

$$FP_{\mathrm{tot}} = \sum_{m=0}^{\infty} \left(r_{21} e^{(j\omega n d/c)} e^{-\alpha d/2} \right)^{2m} = \frac{1}{1 - \left(r_{21} e^{(j\omega n d/c)} e^{-\alpha d/2} \right)^{2}}, \tag{1.18}$$

where $\mathrm{FP}_{\mathrm{tot}}$ is the correction factor that includes all of the reflections in the output signal.

1.6 THz Nonlinear Spectroscopy

When an intense field is applied to a nonlinear material, its refractive index is modified by an intensity-dependent term according to

$$n = n_0 + n_2 I, \tag{1.19}$$

where n_0 is the linear refractive index, I is the field intensity and n_2 is the nonlinear refractive index. As the field propagates through the sample, it accumulates a phase. For intense fields, in addition to the phase corresponding to the linear propagation, it acquires a phase proportional to the field's intensity:

$$\Delta\phi = \underbrace{n_0 k_0 L}_{\text{Linear phase}} + \underbrace{n_2 I k_0 L}_{\text{Nonlinear phase}} . \tag{1.20}$$

From the Fourier analysis, we know that the phase in the Fourier-domain is equivalent to the delay in the time-domain, according to $f(t - \tau) \overset{F}{\leftrightarrow} F(\omega) e^{-i\tau\omega}$. Thus, the accumulated phase is equivalent to a delay in time domain. As a result, for a material with a positive n_2, we expect that the higher the intensity of the applied field is, the more phase it acquires and, consequently, the larger the delay experienced by THz pulse. THz-TDS enables us to simultaneously measure the phase and amplitude response. For the nonlinear spectroscopy, we calculate the nonlinear phase as the differential phase of the intense THz signal with respect to the response of the lowest signal level:

$$\Delta\phi_{\mathrm{NL}} = \phi_{\mathrm{t}} - \phi_{\mathrm{low}} = n_2 I k_0 L, \tag{1.21}$$

where $\Delta\phi_{\mathrm{NL}}$, ϕ_{t} and ϕ_{low} are the nonlinear phase difference, the total phase response of the measurement and the total phase response of the measurement with the lowest THz field amplitude, respectively.

In a similar fashion, the total absorption is expressed as the sum of the linear absorption and the intensity-dependent nonlinear absorption according to

$$\alpha(\omega) = \alpha_0(\omega) + \alpha_2(\omega) I, \tag{1.22}$$

where α, α_0, and α_2 are the total absorption coefficient, linear absorption coefficient and two-photon absorption coefficient, respectively.

In the process of calculating the nonlinear coefficients, two important considerations should be pointed out. First, since the nonlinear phase and absorption are intensity-dependent, the intensity should be calculated accurately. As one can see from Fig. 1.10, the propagation happens between the two Fresnel's reflections, meaning that the effective field intensity for the nonlinear phase and absorption is the electric field after the first reflection. Second, due to the dependence of the nonlinear phase and absorption on the intensity, one should take the effect of the field decay inside the sample into account.

This would be of significance to the samples with a notable absorption. In Chapter 3, we will show that, assuming an insignificant field evolution inside the sample, the effective field of the nonlinear effects is calculated by applying an average absorption equal to the half of the sample thickness. In other words, we should replace the $\mathrm{E}(\omega)$ with $\mathrm{E}(\omega)e^{(-\frac{\alpha d}{4})}$. We should note that the absorption coefficient is usually defined as the decay rate with respect to the intensity, not the field. Thus, the decay rate with respect to the field is one half compared to that with respect to the intensity.

1.7 **Existing Studies on the THz Nonlinear Optics**

1.7.1 THz Induced Nonlinear Effects

THz-TDS enables simultaneous measurement of the magnitude and phase of the THz signal through the linear electro-optic effect, representing a suitable technique for measuring the complex refractive index of a material at the THz frequencies [16]. The recent development of intense THz pulse generation techniques opens the door to studying nonlinear behavior of different materials in the THz region [17]. Nonlinear effects such as THz-induced impact ionisation and inter-valley scattering in semiconductors [26, 40, 41, 42, 43], THz high-harmonic generation by hot carriers [44, 30, 45, 46], and THz-induced ferroelectricity and collective coherence control have been demonstrated [40, 47, 48]. A very large third-order nonlinearity has been reported for water vapor [49] where the stepwise multiphoton transitions in water molecules lead to a third-order susceptibility of $\chi^{(3)} = (0.4 + 6i) \times 10^{2}\ \mathrm{m}^{2}\ \mathrm{V}^{-2}$.

Extreme THz-induced Kerr effects have been reported for different liquids [50, 51, 52, 53, 54], where the nonlinear refractive indices can be several orders of magnitude larger than their values in the optical regime. THz-induced Kerr effect has also been used to demonstrate a transient orientation of dipole moments in liquid water and also the effect of cation and anions on the total polarizability anisotropy of aqueous ionic solutions [55, 56]. THz-induced Kerr effects have been observed in amorphous chalcogenide glasses such as arsenic trisulfide and arsenic triselenide [57]. Kerr-like nonlinearitiy induced by a strong THz field has been reported in ZnTe, where the combination of THz generation and linear electro-optic effect reveals a THz-induced Kerr effect in optical frequencies using Z-scan technique [58].

THz-induced Kerr-type birefringence has been investigated in the common optical window and substrate materials such as diamond, sapphire and magnesium oxide in a THz pump-optical probe configuration [59]. Z-cut quartz has also been explored and exhibits a birefringence due to a linear electro-optic effect.

Crystalline quartz has been used to efficiently generate intense broadband pulses and also in broadband electro-optic sampling for the frequencies up to 8 THz [60, 61]. Furthermore, it has been theoretically predicted that crystals can demonstrate an extremely large nonlinear refractive index at the the THz frequency range [62]. Crystalline solids such as quartz are predicted to show THz nonlinear refractive indices that exceed the optical values by several orders of magnitude. Z-scan measurements of ZnSe crystal at the THz frequencies has shown a nonlinear refractive index of $n_2 = 4 \times 10^{-11}\ \mathrm{cm}^2\ \mathrm{W}^{-1}$ [63].

The majority of the THz-induced nonlinear refractive index measurement studies, using both Z-scan technique and THz-TDS, are based on optical probe beams, resulting in the measurement of the THz-induced third-order susceptibility in the form of $\chi^{(3)} = (\omega_{\mathrm{opt}}, \omega_{\mathrm{opt}}, \Omega_{\mathrm{THz}}, -\Omega_{\mathrm{THz}})$. Moreover, THz Z-scan has been shown to be prone to error for thick samples [64]. However, there has not been any experimental demonstration of THz-induced intensity-dependent refractive index using THz-TDS in a THz pump-THz probe measurement scheme reported to date, to the best of our knowledge. In Chapter 2 of the thesis, we report on the measurement of n_2 in crystal quartz using THz pump and THz probe technique.

1.7.2 Modelling of THz Pulse Propagation in Nonlinear Medium

Different numerical models for the propagation of ultrashort optical pulses in nonlinear medium have been proposed [65]. These models are categorized under two main groups: envelope-based models and carrier-resolving models where the latter is more suitable for ultrashort pulses of which the bandwidth is significant compared to central frequency. An envelope-based model has been proposed to model the self-phase modulation and frequency generation for THz few-cycle pulses in a nonlinear dispersive medium [66], where their presented model is used to compare the effect of linear dispersion and nonlinear effects in different length scales on the envelope evolution,in the paraxial regime. Another method based on unidirectional pulse propagation equation (UPPE) has been used to study the effects of dispersion, diffraction and time-varying nonlinear refraction in the non-paraxial regime [67].

1.7.3 Measurement of the Nonlinear Refractive Index at THz Frequencies

There are several techniques developed to measure nonlinear refractive index in both optical and THz regimes. Z-scan technique has been used to measure THz-induced third-order susceptibility in the schemes with an optical [58] or a THz probe beam [50]. However, as mentioned earlier, the accuracy of Z-scan at THz frequencies declines with the increase of the sample thickness [64]. Similarly, the measurement of the THz-induced n_2 is carried out in THz-TDS systems in two ways. In the first configuration, THz-induced index change is measured in the optical regime through the recording of THz Kerr-signal [51, 59]. In the second configuration, the nonlinear effect induced by the THz field is sensed by the THz field as it propagates through the sample. In other words, the THz beam acts as both pump and probe simultaneously. The studies in Chapter 2 and Chapter 3 are based on this configuration. Of the works studying this configuration, full-phase extraction of n_2 is the most common approach. In the works [49, 68], another method is used for the extraction of n_2 around the sharp resonances of water vapor at THz frequencies. In this method, in order to estimate the value of n_2 for each resonance, the phase response has been normalized by the spectral density of the signal around the same resonance. However, in these two approaches, the dependence of the calculated n_2 dispersion on the pulse spectral content has not been explored. Thus, it is of a great interest to derive an expression that takes the THz pulse spectral shape into account in the calculation process. In Chapter 3 of the thesis, we develop such a theoretical model capable of describing nonlinear interaction under broadband THz excitation. Furthermore, the model allows one to extract the dispersion of the nonlinear refractive index at the THz frequency range.

1.7.4 *THz-Induced Third-Order Susceptibilities*

In addition to the two THz-field induced nonlinear effects mentioned earlier, there is yet another third-order nonlinear THz effect such as THz field-induced second-harmonic (TFISH) generation. In this effect, a THz field induces an SHG at optical frequencies, and the associated nonlinear susceptibility can be described as $\chi^{(3)}(2\omega_{\mathrm{Opt}}+\omega_{\mathrm{THz}}, \omega_{\mathrm{Opt}}, \omega_{\mathrm{Opt}}, \omega_{\mathrm{THz}})$. The measurement of the nonlinear susceptibility responsible for the TFISH in a Z-scan setup shows that its value for chalcogenide glasses is more than three orders of magnitude larger than the corresponding value of the reference sample, $\mathrm{SiO_2}$. This can be attributed to the strong nonlinear response of Se contained in chalcogenide glasses [69]. The reported nonlinear susceptibility values for each group of the nonlinear THz interactions are categorized and shown in Table 1.2. In Chapter 4 of the thesis, we establish a relationship between these three groups of the nonlinear processes. This effort is of great importance for the measurement consistency of the nonlinear coefficients in different frequency ranges. Also, in a collaboration with Prof. Jepsen's group at DTU, we predict the value of the TFISH for $\mathrm{SiO_2}$ at its resonance frequency (see Chapter 4 of the thesis) that is verified by their experimental work [74].

1.8 **Thesis Layout**

The current Introduction chapter provides the background for all the aspects of ”THz Nonlinear Time-Domain Spectroscopy”. We start with the introduction of the THz spectral range and different methods of generation and detection of the THz waves. Then,

THz-induced nonlinearity					
THz probe		Optical probe			
THz nonlinear refractive index		THz-induced Kerr		TFISH	
Material	$n_2(\mathrm{m}^2/\mathrm{W})$	Material	$n_2(\mathrm{m}^2/\mathrm{W})$	Material	$\chi^{(3)}(\mathrm{m}^2/\mathrm{V}^2)$
Water [50, 52, 70]	7×10^{-14}	$\mathrm{CS_2}$[51]	4.4×10^{-18}	$\mathrm{As_2S_3}$[69]	3.4×10^{-19}
Ethanol[50]	6×10^{-13}	Benzene [51]	5.6×10^{-19}	Si [71]	2×10^{-18}
α-pinene [50]	3×10^{-13}	$\mathrm{CCl_4}$ [51]	2.7×10^{-19}	$\mathrm{SiO_2}$ [71]	2.8×10^{-22}
Water vapor [70]	0.6×10^{-14}	$\mathrm{CCl_3}$ [51]	1×10^{-19}		
Si [72]	1.2×10^{-16}	$\mathrm{CH_2I_2}$ [51]	1.4×10^{-18}		
		$\mathrm{As_2S_3}$[57]	3.4×10^{-18}		
		$\mathrm{As_2Se_3}$[57]	1.7×10^{-18}		
		Diamond [59]	3×10^{-20}		
		ZnTe [58]	1×10^{-17}		
		GaP [73]	1.7×10^{-17}		

Table 1.2: The reported values for the THz nonlinear refractive index, THz-induced Kerr effect, and TFISH

we introduce the the concept of THz-TDS in a transmission geometry and extend it to the nonlinear regime.

In Chapter 2, we modify a previously developed theoretical model for the nonlinear refractive index of crystalline quartz. Next, we report on the experimental observation of a very strong nonlinear response in crystalline quartz in the terahertz (THz) frequency region through THz time-domain spectroscopy (THz-TDS).

In Chapter 3, we propose a simple method to analyze the propagation of intense THz pulses in a nonlinear medium via Fourier analysis. Using the same method we derive an expression for the extraction of the nonlinear refractive index dispersion from the nonlinear phase spectrum.

In Chapter 4, we attempt to establish a theoretical relationship between three different THz-induced third-order nonlinear effects: THz nonlinear refraction, THz-induced Kerr effect and THz field-induced second-harmonic generation (TFISH).

Finally, in Chapter 5, we summarize the studied concepts and draw conclusions.

Chapter 2

STRONG NONLINEAR RESPONSE OF CRYSTALLINE QUARTZ AT THE THZ FREQUENCIES

2.1 **Introduction**

A recent theoretical study has predicted that at the THz frequencies crystals could demonstrate giant nonlinear responses as a result of the strong coupling between the THz radiation and vibrational modes in solids [62]. Furthermore, several experimental reports have demonstrated a similar strong coupling in different liquids that leads to the nonlinear refractive indices several orders of magnitude larger than the typical n_2 values in the optical regime [50, 52, 53, 54]. Moreover, another experimental work reported an extreme nonlinear response for the water vapor at the THz frequencies, that is attributed to the vibrational-rotational transitions [49].

In this chapter, we report on the experimental observation of very strong nonlinear interactions in crystalline quartz in the THz regime. First, a theoretical model for the nonlinear refractive index of quartz at the THz frequencies is presented [62]. This model relies on the classical anharmonic oscillator, where the nonlinear refractive index is given as a sum of contributions from different vibrational modes. As predicted by the model, the value of the nonlinear refractive index at the lower frequencies exceeds its typical values in the visible range by several orders of magnitude. Then, we perform nonlinear THz-TDS on a 1-mm-thick z-cut quartz sample. The time-domain analysis of the collected data demonstrates an increased delay, experienced by the pulse as it propagates through the sample, with increasing THz beam intensity. However, the growth rate of the delay decreases with the further intensity increase, revealing a phase saturation process. Further, the analysis in the Fourier domain shows an increase in the nonlinear phase and nonlinear absorption with the increase of the THz field intensity. At higher signal levels, however, the nonlinear phase grows with the field intensity increase at a declining pace, whereas the nonlinear absorption tends to increase more rapidly. The data analysis revealed extremely large values of the nonlinear refractive index and fifth-order susceptibility, where the latter has a negative real part. The results of this research were published in Advanced Optical Materials journal.

Publication: **S. Zibod**, P. Rasekh, M. Yildrim, W. Cui, R. Bhardwaj, J.-M. Ménard, R. W. Boyd, and K. Dolgaleva, "Strong nonlinear response in crystalline quartz at thz frequen- cies," Advanced Optical Materials, vol. 11, no. 15, p. 2202343, 2023.

2.2 Theory

An extremely large refractive index has been theoretically predicted for quartz in the THz regime, where the nonlinear refractive index was predicted to be several orders of magnitude larger than its typical visible and near-infrared values [62]. The model is based on the equation of motion of a classical anharmonic oscillator:

$$\ddot{x} + 2\gamma\dot{x} + \omega_0^2 x + ax^2 + bx^3 = \alpha E, \tag{2.1}$$

where x is the ion displacement from the equilibrium position, γ is damping factor, ω_0 is the resonance frequency, E is the applied field and a and b are the second- and third-order nonlinear coefficients, respectively. The parameter α on the right-hand side of Eq. (4.1) is determined as $\alpha = q/m$, where q and m are the effective electric coupling strength and effective reduced mass of the vibrational mode, respectively. After applying perturbation theory and performing some algebraic operations [62], the relationship between the complex nonlinear refractive index and the resonance parameters takes the form

$$\tilde{\bar{n}}_2 = \frac{\pi q N}{\tilde{n}_0} \frac{\alpha^3}{(\omega_0^2 - \omega^2 - 2\gamma i \omega)^4} \times \left[2a^2 \frac{3\omega_0^2 - 8\omega^2 - 8\gamma i \omega}{\omega_0^2(\omega_0^2 - 4\omega^2 - 4\gamma i \omega)} + 3b \right]. \tag{2.2}$$

Here N is the atomic density, and $\tilde{n}_0$ is the linear refractive index. Among the two terms, the term related to the second-order nonlinearity is two orders of magnitude larger than the contribution coming from the third-order nonlinear coefficient b. This can be attributed to the fact that the cascaded processes are usually much stronger than the direct higher-order processes. The nonlinear coefficient a is related to the known parameters of the crystal through

$$a = -\frac{a_1 m \omega_0^4}{k_B} \alpha_T, \tag{2.3}$$

where a_1 is the lattice constant, k_B is Boltzmann constant and α_T is the thermal expansion coefficient. With the assumption of a single dominant vibrational mode at 37.2 THz and ignoring the much weaker resonances at lower frequencies, one can evaluate the nonlinear refractive index of crystalline quartz at very low frequencies to be $\bar{n}_2^{\omega \ll \omega_0} \approx 2.21 \times 10^{-9}$ esu or, equivalently, $4.42 \times 10^{-16}\ \mathrm{m}^2\ \mathrm{W}^{-1}$ [62].

However, the strong vibrational resonance at 37.2 THz is not the only resonance contributing to the vibrational n_2. There are several other resonances at lower frequencies, among which are the ones at 3.9 THz and 7.9 THz [75]. To take the contribution of these additional resonances into consideration, we modify Eq. (2.2) into the form

$$\bar{n}_2 = \frac{\pi q N \alpha^3}{\tilde{n}_0} \sum_{j=1}^{3} \frac{1}{(\omega_{0,j}^2 - \omega^2 - 2\gamma i\omega)^4} \times \left[2a_j^2 \frac{3\omega_{0,j}^2 - 8\omega^2 - 8\gamma i\omega}{\omega_{0,j}^2(\omega_{0,j}^2 - 4\omega^2 - 4\gamma i\omega)} + 3b_j \right]. \quad (2.4)$$

In this modified equation, the nonlinear refractive index is now given as a sum of the contributions from the three resonances: the strong resonance at 37.2 THz, and the weaker resonances at 3.9 THz and 7.9 THz. Cross-interactions between the phonon resonances, as it was previously reported in the case of second-harmonic generation in the mid-infrared frequency range, could be considered to refine the theoretical model, but it is beyond the scope of this work [76]. Eq. (2.3) shows that the second-order nonlinear coefficient is proportional to ω_0^4, meaning that the resonant value of the nonlinear coefficient for the dominant resonance is, for instance, approximately 500 times larger than that for the resonance at 7.9 THz.

Fig. 2.1 shows the dispersion of the nonlinear refractive index caused by the dominant resonance and the resonances at 7.9 THz and 3.9 THz. The top inset of the figure resolves the value of n_2 at around low-frequency resonances. The comparison indicates that the nonlinear refractive index at the dominant resonance at 37.2 THz is approximately 20 times larger than the one at the stronger resonance of the two lower-frequency resonances.

Substituting Eq. (2.3) into Eq. (2.4), we can see that the contributions of different resonances to the nonlinear refractive index at very low frequencies are proportional to $1/\omega_0^2$. Consequently, at much lower frequencies (1 THz and below), the contributions from the resonances at 7.9 THz and 3.9 THz are approximately 20 times larger and 100

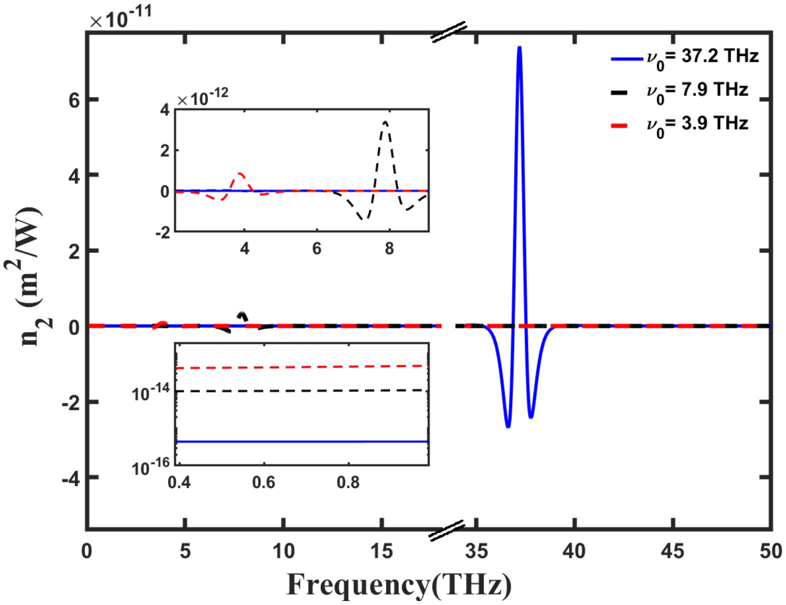

Figure 2.1: Theoretical modelling of the nonlinear refractive index caused by the dominant resonance at 37.2 THz (blue solid lines) and the resonances at 7.9 THz (black dashed lines) and 3.9 THz (red dashed lines) in quartz. The top inset resolves the values of the nonlinear refractive indices at around the low-frequency resonances. The bottom inset shows the contribution from three resonances at the lower frequencies (1 THz and lower).

times larger than the one at 37.2 THz, respectively, as shown in the bottom inset of Fig. 2.1. The contributions of the three resonances to the nonlinear refractive index are listed in Table 2.1. The table clearly demonstrates that the dominant contributions to the nonlinear refractive index at very low frequencies are from the resonances at 7.9 THz and 3.9 THz: $n_2^{\omega \ll \omega_0} \approx 5.17 \times 10^{-14}\ \mathrm{m}^2\ \mathrm{W}^{-1}$.

2.3 Experiment

The intense THz radiation is generated in an optical rectification process in lithium niobate ($\mathrm{LiNbO_3}$), where the pulse-front tilting technique is used to make the process

ω_0 (THz)	$n_2^{\omega \ll \omega_0}$ (m^2 W^{-1})	$n_2^{\omega \approx \omega_0}$ (m^2 W^{-1})
3.9	4.17×10^{-14}	8.38×10^{-13}
7.9	9.98×10^{-15}	3.35×10^{-12}
37.2	4.42×10^{-16}	7.40×10^{-11}

Table 2.1: The contribution to the nonlinear refractive index. The comparison indicates that the nonlinear refractive index at the dominant resonance at 37.2 THz is approximately 20 times larger than the one at the stronger resonance of the two lower-frequency resonances. However, at much lower frequencies (1 THz and below), the contributions from the resonances at 7.9 THz and 3.9 THz are approximately 20 times larger and 100 times larger than the one at 37.2 THz, respectively.

phase-matched and efficient [17]. The setup schematic is depicted in Fig. 2.2. The beam, coming from a 800-nm Ti:sapphire laser with a pulse duration of 45 fs and repetition rate of 1 kHz, is split into the pump and probe paths. In the pump path, the beam diffracts from a grating and, after passing through two cylindrical lenses, propagates through the generation crystal. The generated THz radiation is collimated and focused with several gold off-axis parabolic mirrors. A pair of wire-grid polarizers is also used to control the THz field amplitude during the measurements.

In the probe path, the near-infrared (NIR) probe and THz beams co-propagate inside the 200-μm-thick ZnTe detection crystal. A delay stage is also used to change the overlap time between the THz and probe beams, so that one can measure different points of the THz pulse. As the THz pulse propagates through the detection crystal, the refractive index experienced by the probe beam is modified through the linear electro-optic effect, resulting in a birefringence in the crystal. The phase difference induced by the birefringence is then converted into the beam's ellipticity via a quarter-wave plate. A Wollaston

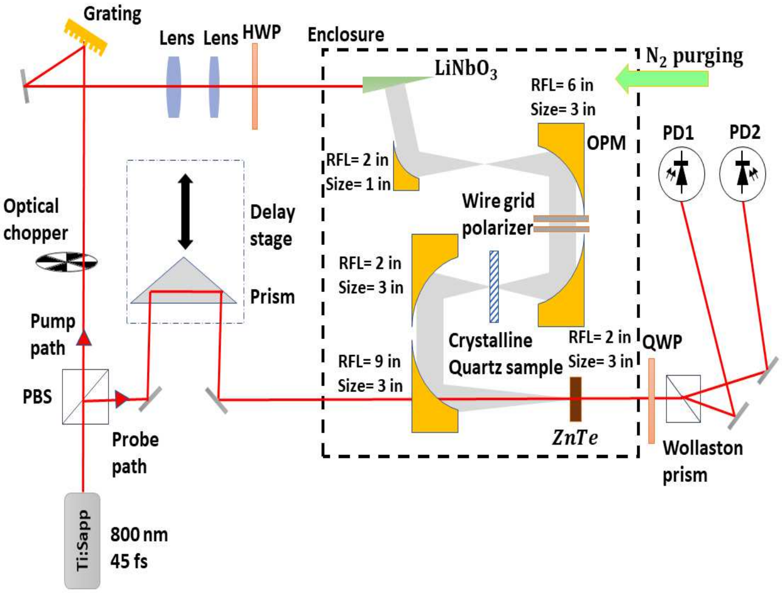

Figure 2.2: The schematic of THz-TDS experimental setup. The 800-nm beam is split into pump and probe paths. The phase-matching condition required for the generation of intense THz field in $\mathrm{LiNbO_3}$ crystal is achieved through the pulse-front tilting technique. OPM: Off-axis parabolic mirror; HWP: Half-wave plate; QWP: Quarter-wave plate; PD: Photodetector; RFL:Reflective focal length.

prism splits the beam into two components of which their intensity difference is proportional to the beam ellipticity. Finally, a pair of balanced photodetectors connected to the lock-in amplifier is used to detect the differential signal. The peak amplitude of the electric field is estimated to be 225 $\mathrm{kV\ cm^{-1}}$ at the focal position where we place the 1-mm z-cut quartz sample. To eliminate the water-vapor absorption, the part of the setup where the THz beam is generated and propagates is enclosed and purged with nitrogen. Different field amplitudes are obtained by rotating the first wire-grid polarizer and keeping the second one fixed.

2.4 **Results and Discussion**

In Fig. 2.3 (a), we show the time-domain signals for different THz field amplitudes for both free-space and crystalline quartz. One can observe an increase in the time delay experienced by the pulse in the crystal quartz with an increase of the THz field amplitude. The inset in Fig. 2.3 (a) clearly demonstrates this observation. In contrast, the free-space THz time-domain signal does not exhibit such a delay increase.

Fig. 2.3 (b) shows the average time shift for each of the THz field amplitude levels compared to the lowest-level amplitude, where the average time shift for each level is calculated as

$$t_{\mathrm{av}}^{i} = \frac{1}{N}\sum_{k}^{N} t(V_i = V_k) - t(V_{\mathrm{low}} = V_k). \tag{2.5}$$

Here t_{av}^{i} is the average time shift, N is the number of data points, V_i is the i-th signal and V_{low} is the lowest-level signal. The analysis is performed over the main lobe, the interval between the first two minima, highlighted in the inset of Fig. 2.3 (a), as it represents most of the THz spectral content. We can see that, with the field intensity increase, THz pulse experiences more delay with respect to the lowest-intensity pulse. However, at higher intensities, the growth slope declines, which indicates the presence of the saturation effect. From the pulse duration of $\tau_d \approx 2.5$ ps, one can estimate the nonlinear refractive index by approximating the signal with its main frequency component $f \approx 1/\tau_{\mathrm{d}} = 0.4$ THz. We can relate the nonlinear refractive index to the slope of the linear region of the figure through $n_2 = (\Delta t_{\mathrm{av}}/\Delta I)cd^{-1}$, where $d = 1$ mm is the thickness of the sample. Thus, the nonlinear refractive index is calculated to be $n_2 = 7.5\times10^{-14}\ \mathrm{m}^2\ \mathrm{W}^{-1}$. At higher intensities, the saturation effect limits the the refractive index change, reducing the nonlinear refractive index to smaller values. Thus, the delay increases at a slower pace with the further increase of the intensity. Fig. 2.4 (a) shows the spectral density for the quartz sample and free space in the frequency range between 0.3 and 2 THz, where the fast Fourier transform (FFT) performed on the time-domain signal is depicted. We notice that as the signal level increases, the absorption, which is the difference between the free-space and quartz sample spectra after factoring out the sample's Fresnel reflections, increases. This behavior clearly indicates the presence of a nonlinear absorption process.

Fig. 2.4 (b) shows the nonlinear phase experienced by the THz signal for different intensity levels at 0.4 THz where the spectral density is maximum. It indicates that, as the THz intensity increases, the nonlinear phase cannot be expressed with a single nonlinear term, and suggests a negative higher-order nonlinearity term. Z-cut quartz is a non-centrosymmetric crystal, meaning that both the even- and odd-order susceptibilities are nonzero. However, the even-order nonlinearities are not of direct relevance in this study, as we are interested in exploring the nonlinearities at the fundamental frequency. Nevertheless, the even-order nonlinearities can contribute to the self-action effects in a cascaded manner [62]. The differential nonlinear phase for the higher THz field amplitudes in a sample with a thickness of d is related to the intensity by

$$\phi_i^{\mathrm{NL}}(\omega) = \phi_i(\omega) - \phi_{\mathrm{low}}(\omega) \ = n_2(\omega) I_i \frac{\omega}{c} d + n_4(\omega) I_i^2 \frac{\omega}{c} d. \tag{2.6}$$

Here ϕ_i is the total phase of the i-th signal and ϕ_{low} is the phase experienced by the lowest-level signal, used as the linear response of the material, n_2 and n_4 are the nonlinear refractive index coefficients associated with the third-order and fifth-order nonlinear

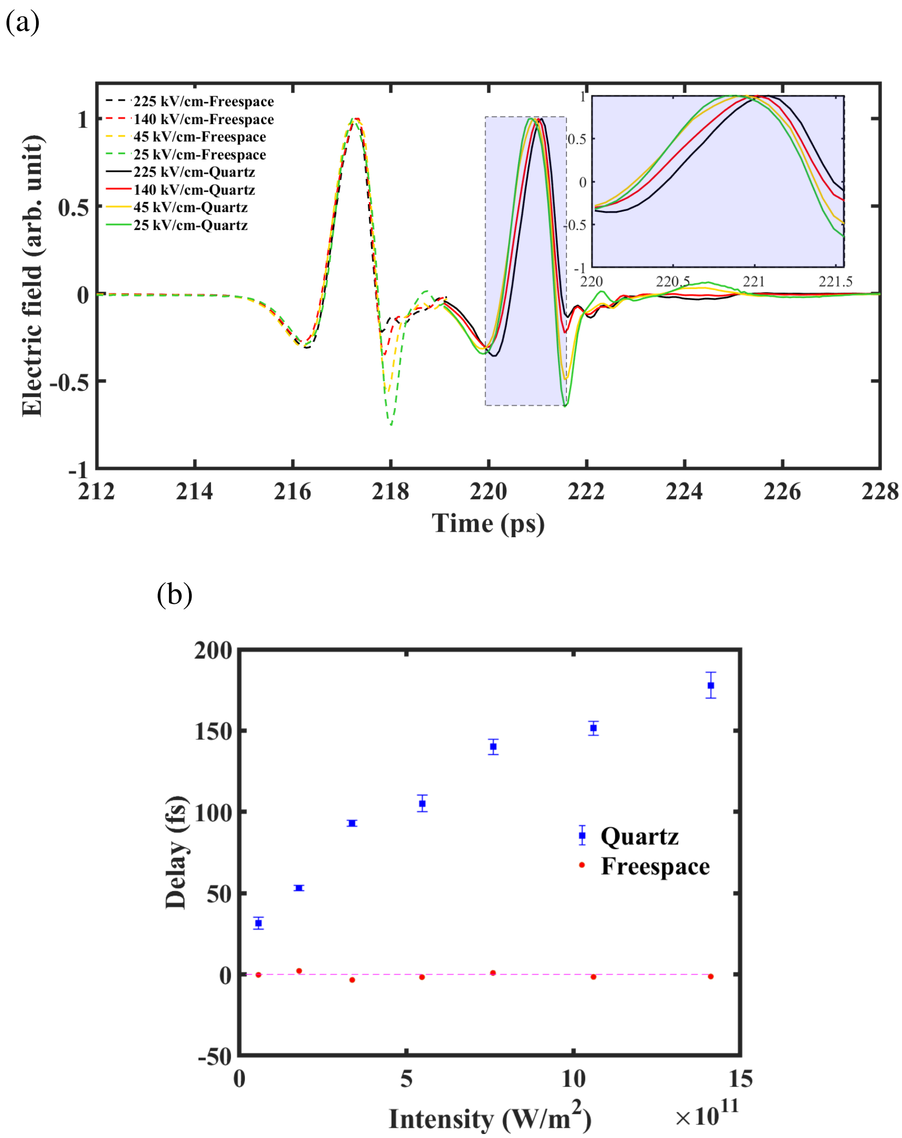

Figure 2.3: (a) THz time-domain signal in free space (dashed lines) and crystalline quartz (solid lines) for different intensity levels. The inset shows the delay increase with the growth of the THz amplitude. (b) The average time shift in free space (red) and in crystalline quartz (blue) for different intensity levels.

susceptibilities, respectively, and I_i is the peak intensity of the i-th level signal. By observation of Fig. 2.4 (b), one can conclude that a negative n_4 effect is likely to be

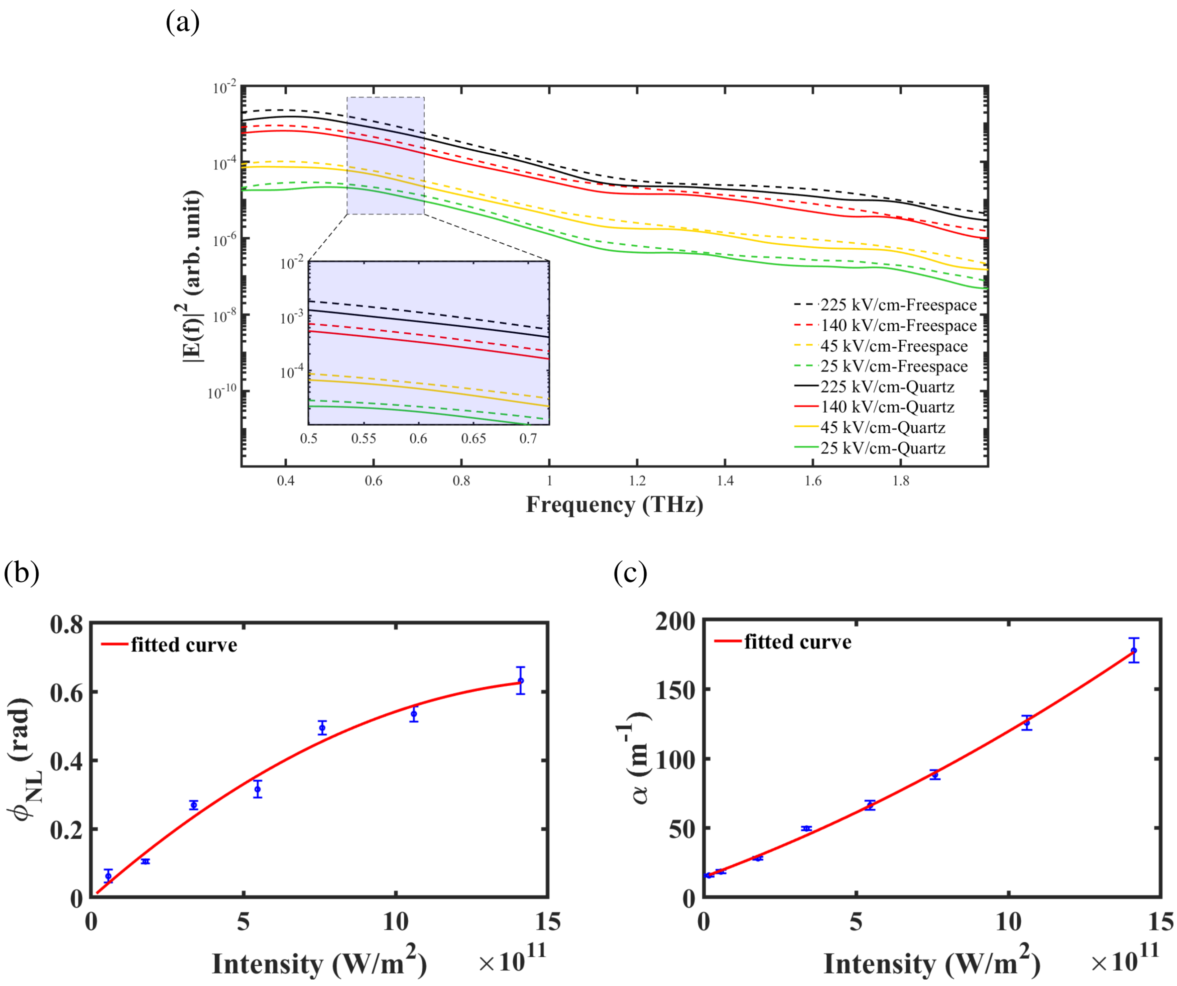

Figure 2.4: (a) Signal spectral density for free-space (dashed lines) and quartz (solid lines). The difference between the free-space and quartz signals increases with an increase in the signal level. (b) Nonlinear phase experienced by the signal of different amplitude at 0.4 THz. (c) Absorption coefficient for each signal level at 0.4 THz.

contributing to the intensity dependence of the nonlinear phase shift.

The absorption coefficient of crystalline quartz, measured as a function of the THz intensity, is depicted in Fig. 2.4 (c). We can see that at lower intensities, the absorption coefficient increases linearly with respect to the field intensity. However, at higher intensities, a quadratic term also reveals itself. The absorption coefficient of the material can be expressed as

$$\alpha(\omega) = \alpha_0(\omega) + \alpha_2(\omega) I_i + \alpha_4(\omega) I_i^2, \tag{2.7}$$

where α, α_0, α_2, and α_4 are the total absorption coefficient, linear absorption coefficient, two-photon absorption coefficient and three-photon absorption coefficient, respectively. We calculate the value of n_2 to be $n_2 = (9.0 \pm 1.4) \times 10^{-14}\ \mathrm{m^2\ W^{-1}}$. This value is 20% greater than the value estimated from the time-domain analysis of n_2 at 0.4 THz as the main frequency component of the signal. This difference is potentially rooted in approximating the signal with a single-frequency component. In fact, the frequencies with lower amplitudes experience smaller nonlinear delay and reduce the average time shift calculated in the time domain. Furthermore, the measured value exceeds the theoretically predicted value by a factor of 1.74. This difference arises from the fact that the calculations carried out theoretically were based on the assumption that the field is monochromatic. However, the THz field used in the experiment is a short wide-band pulse. Consequently, there are contributions to the nonlinear phase shift at 0.4 THz from different frequencies, resulting in the higher value of ϕ^{NL}. Furthermore, the data analysis reveals the values of other nonlinear coefficients: $n_4 = (-2.7 \pm 1.0) \times 10^{-26}\ \mathrm{m^4\ W^{-2}}$, $\alpha_2 = (8.1 \pm 0.9) \times 10^{-11}\ \mathrm{m\ W^{-1}}$ and $\alpha_4 = (2.4 \pm 0.6) \times 10^{-23}\ \mathrm{m^3\ W^{-2}}$. The real and imaginary parts of the third-order and fifth-order nonlinear susceptibilities are related to these nonlinear coefficients as:

$$\Re(\chi^{(3)}) = \frac{4}{3} n_0^2 \varepsilon_0 c n_2, \tag{2.8a}$$

$$\Im(\chi^{(3)}) = \frac{2}{3} n_0^2 \varepsilon_0 \frac{c^2}{\omega} \alpha_2, \tag{2.8b}$$

$$\Re(\chi^{(5)}) = \frac{8}{5} n_0^3 \varepsilon_0^2 c^2 n_4, \tag{2.8c}$$

$$\Im(\chi^{(5)}) = \frac{4}{5} n_0^3 \varepsilon_0^2 \frac{c^3}{\omega} \alpha_4. \tag{2.8d}$$

Thus, the complex third-order and fifth-order nonlinear susceptibilities are found as $\chi^{(3)} = (1.4\times10^{-15} + i7.5\times10^{-17})$ m^2 V^{-2} and $\chi^{(5)} = (-2.7\times10^{-30} + i1.5\times10^{-31})$ m^4 V^{-4}, respectively. These measurements confirm the presence of an extremely large nonlinear refractive index at lower THz frequencies.

This extreme behavior agrees with the theoretical modelling presented in Section 2 for the lower frequency regime. However, in order to examine the presented model in a wide spectrum, specially in the vicinity of the phonon resonances, one may need to excite the sample at these frequencies, which is beyond the spectral range provided by our source. The sources based on DAST organic crystals or two-color air plasma generation can be used to cover a wider spectral range.

Another challenge that requires a special treatment when pumping at the resonance frequencies is the strong absorption that may prevent the observation of any signal. Moreover, the absorption rapidly reduces the field strength, preventing the propagation of the nonlinear driving field. As a solution to this challenge, one may need to convert the setup to a reflection geometry as implemented previously for the case of the second-harmonic generation in quartz at the THz frequencies [76].

2.5 Conclusions

We have observed a strong nonlinear response of crystalline quartz in the THz region. The experimental results confirm the theoretical predictions made earlier, with an amendment to the theory by including additional vibrational resonances.

Further, time-domain spectroscopy reveals that the observed nonlinear behavior results from a complex interplay of the third- and fifth-order susceptibilities, where the real part shows a positive third-order and a negative fifth-order contributions. Furthermore, the measured nonlinear refractive index of $n_2 = 9.0 \times 10^{-14}\ \mathrm{m}^2\ \mathrm{W}^{-1}$ at 0.4 THz is seven orders of magnitude larger than the nonlinear refractive index of fused silica measured in the visible region. We attribute this large nonlinearity to the contributions from the vibrational modes in the crystal. Numerical evaluation of Eq. (2.4) reveals that the vibrational modes at 3.9 and 7.9 THz are the primary contributions to this large nonlinear response, despite the fact that the strong resonance at 37.2 THz might be expected to be the origin of the large optical nonlinearity. Including these lower-frequency resonances allowed us to obtain a correct order-of-magnitude agreement between the theory and experiment. The slight difference in the values of the measured and predicted n_2 (a factor of 1.74) is rooted in the fact that the spectrum of the THz radiation is wide-band, and the contribution of different spectral components is possible. This difference is a motivation for the exploration aimed at pushing the analysis beyond the approximation of a monochromatic radiation – the necessary measure in the extremely wide-band THz frequency range.

Chapter 3

BROADBAND THZ PULSE PROPAGATION IN NONLINEAR MEDIUM: DISPERSION OF THE NONLINEAR REFRACTIVE INDEX

3.1 **Introduction**

THz nonlinear TDS allows one to measure the material response to an intense single-cycle ultrashort THz pulse. This ultrashort pulse has a wideband spectrum. For example, a THz field with the pulse duration of 2 ps has a spectral content centered around 0.5 THz and extending up to 1 THz. Thus, exploring the dependence of the experimental data on the spectral shape of the THz pulse is of a great interest for a precise characterization of the material in the THz region.

This chapter studies the effect of the nonlinear dispersion in the THz-TDS measurement of the nonlinear refractive index. A simple model for the propagation of ultrashort THz pulse in a nonlinear medium is proposed. This model is a spectral solution to the wave equation based on Fourier analysis under the slowly evolving wave approximation (SEWA) condition [77]. The result of the simulations for a quartz sample has a good agreement with the experimental results previously presented in Chapter 2. In addition, we analyse the effect of nonlinear refraction on the delay experienced by the THz pulse. Next, using this pulse propagation model, we simulate an intense THz pulse propagation in an arbitrary medium. We define this medium with a significant absorption and a nonlinear refractive index dispersion with a linear profile. The goal is to calculate the nonlinear refractive index dispersion from the phase response of this simulation and obtain the n_2 dispersion defined for the medium initially. To accomplish this, we derive an expression to calculate the exact dispersion of the nonlinear refractive index from the phase response and successfully extract the n_2 dispersion. Comparing this expression to the existing calculation methods based on monochromatic approximation and sharp resonances, we conclude the effectiveness of this method to factor out the effect of the input pulse spectral shape from the phase data for an accurate calculation of n_2 dispersion. Finally, we apply the proposed method to our experimental results of the nonlinear time-domain spectroscopy of the BK7, a material with a considerable nonlinear response and an absorption profile unique to the chalcogenide and borosilicate glass families. This work enables a precise calculation of the nonlinear refractive index by factoring out the pulse spectral shape from the nonlinear phase response.

Publication: **S. Zibod**, R. Bhardwaj, J.-M. Ménard, R. W. Boyd, and K. Dolgaleva, "Broadband THz Pulse Propagation in Nonlinear Medium: Dispersion of The Nonlinear Refractive Index," 2024, (Manuscript under preparation).

3.2 Numerical Simulation of Pulse Propagation in a Nonlinear Medium

To model the pulse propagation accurately, one needs to choose the proper approximation for the solution to the Maxwell's equations. For single-cycle pulses, slowly varying envelope approximation (SVEA) is not valid, and computationally complex carrier-resolved methods such as unidirectional pulse propagation equation (UPPE) are used [49, 65]. If the backward propagation is negligible, the wave equation is simplified to forward Maxwell's equations (FME) [65],

$$\frac{\partial E(\omega)}{\partial z} = ik(\omega)E(\omega) + \frac{i}{2k(\omega)}\Delta_{\perp}E(\omega) + \frac{i\omega P(\omega)}{2n(\omega)c\varepsilon_0}, \tag{3.1}$$

where the second term on the right-hand side accounts for the diffraction in transverse plane, which is ignored for the sake of simplicity. Under the SEWA condition, the equation can be solved in the spectral domain [77]. The last term of Eq. (3.1) accounts for the nonlinear refractive index contribution, $\mathrm{F}_{\mathrm{NL}}(\omega)$, and is calculated as:

$$F_{\mathrm{NL}}(\omega) = \frac{\omega P(\omega)}{2n(\omega)c\varepsilon_0} = \frac{\omega}{c}n_2(\omega)\mathcal{F}\Bigg(I(t)E(t)\Bigg) \tag{3.2}$$

. For simplicity, we consider the length of the sample in the range of $\pm z_d$ from the focus, z_d being the beam's Rayleigh length, to avoid the spurious effects of beam's divergence and diffraction [50]. This is a reasonable assumption since for a beam spot size of 1 mm in a material with a refractive index of $n \approx 2$, the Rayleigh length is $z_d \approx 2.9\,\mathrm{mm}$ and thus, most of the available optical samples fall within this range. Plugging F_{NL} into Eq. (3.1), we can rewrite the wave equation in the form:

$$\frac{\partial E(\omega)}{\partial z} = ik(\omega)E(\omega) + iF_{NL}(\omega). \tag{3.3}$$

The pulse propagation is modeled using the solution obtained via split-step Fourier method (SSFM), as explained in [78]. In this simulation, the propagation length is split into 100 segments. In each segment, the linear effects (absorption and dispersion) are applied to the input field. Then, the field is transformed back to the time domain using inverse fast Fourier transform (IFFT) with the nonlinear term applied to the field. Then, the output of each segment is the input of the next segment, and the procedure is repeated for the length of the sample, as shown in the Fig. 3.1.

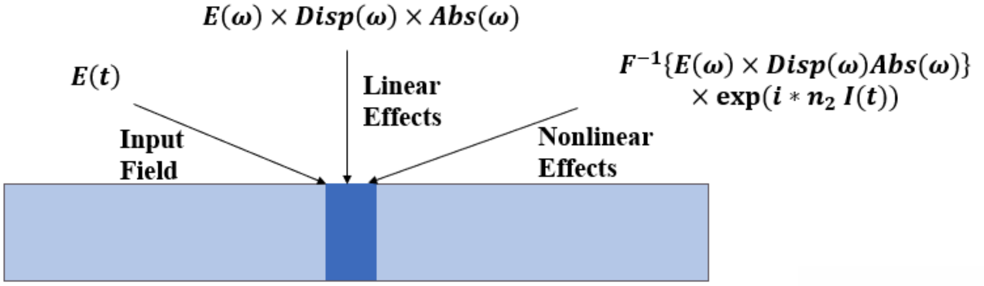

Figure 3.1: The illustration of the idea behind the split-step Fourier method (SSFM). The length of the sample is split into N segments. In each segment, the input time-domain field is transformed into the frequency domain where the linear effects, i.e. the dispersion and absorption, are applied to the field. Then, the nonlinear term is applied to the field after transforming the signal back to the time domain.

To analyze the effect of the nonlinear refraction on the propagation of the intense broadband THz pulse, we numerically simulate the pulse propagation in a medium with a nonlinear response with the strength similar to that reported for the crystal quartz [79] (see Chapter 2). Fig. (3.2) (a) displays the result of the numerical simulations of a single-cycle THz pulse with a pulse amplitude of $125\ \mathrm{kV/cm}$. The 1-mm-thick sample has a nonlinear refractive index of $n_2 = 9 \times 10^{-14}\ \mathrm{m^2/W}$. The nonlinear refractive index imposes an extra delay on the intense THz pulse in addition to the linear phase delay acquired on propagation. Similar to the propagation of a pulse inside a dispersive medium, the different field-induced nonlinear phases in different frequencies change the temporal shape of the signal. In other words, each frequency component of the field "sees" a different refractive index change. Fig. (3.2) (b) shows the nonlinear delay ex-

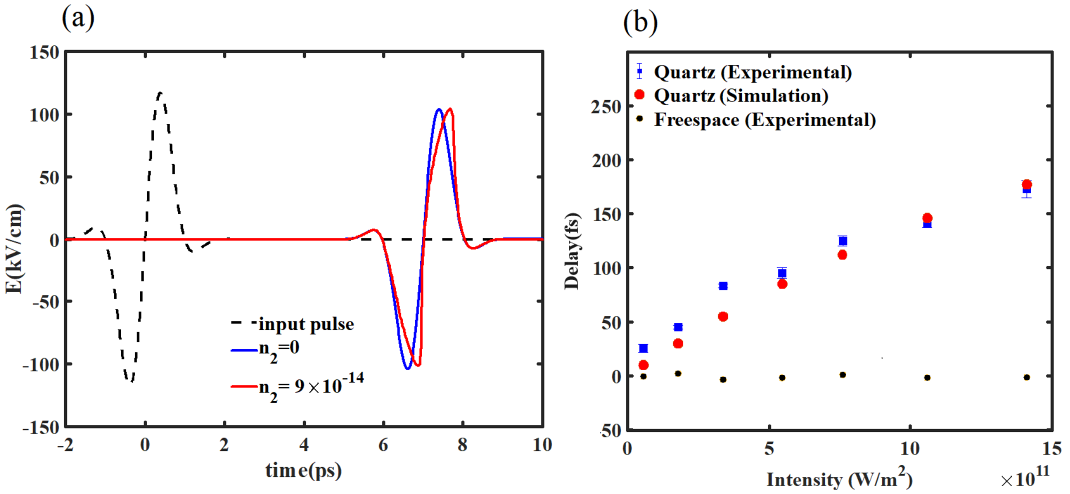

Figure 3.2: (**a**) Numerical simulation of a single-cycle THz pulse in a 1-mm quartz sample. (**b**) The average time shift experienced by the pulse in the sample (numerical simulation and experimental data).

perienced by the pulse in the simulation and the experimental data of Chapter 2 [79]. To replicate the experimental data as close as possible, the term representing the fifth-order susceptibility $\chi^{(5)} = -2.7 \times 10^{-30}$ m^4 V^{-4} is added to Eq. (3.3). We can see that the simulation result agrees with the experimental data. The slight difference between the simulations and the experimental data in Fig. 3.2 (b) can be attributed to the fact that the nonlinear refractive index and the higher-order susceptibility calculated from the experimental data are obtained at the peak frequency under the assumption of a uniform intensity profile for the whole frequency range.

Next, we introduce a dispersion profile to the nonlinear material. Fig. (3.3) (a) shows the effect of the nonlinear refractive index dispersion on the pulse propagation. The simulation is carried out for two scenarios: (i) a constant nonlinear refrac-

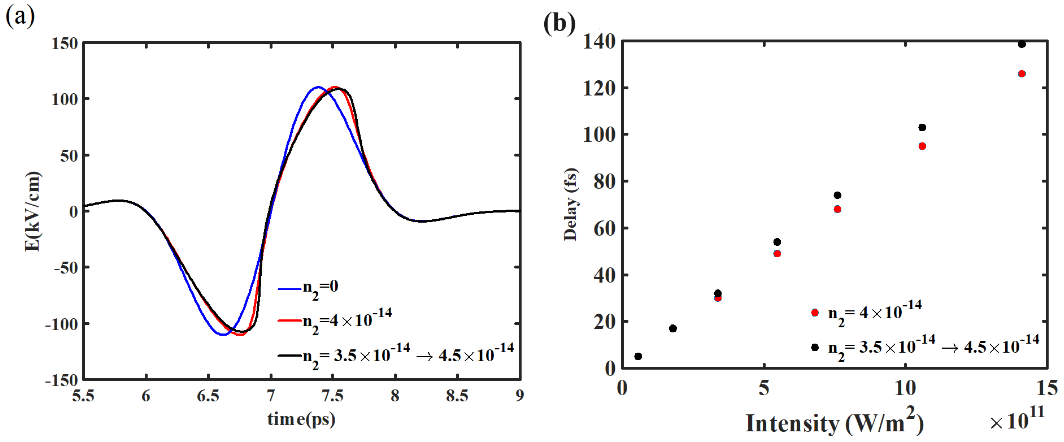

Figure 3.3: (a) Numerical simulation of single-cycle THz pulse in a 1-mm sample with and without nonlinear refractive index dispersion. (b) The average time shift experienced by the pulse in the sample simulated for the two scenarios.

tive index of $n_2 = 4 \times 10^{-14}$ m^2/W; (ii) a linearly changing from $n_2 = 3.5 \times 10^{-14}$ to $n_2 = 4.5 \times 10^{-14}$ m^2/W nonlinear refractive index in the frequency range from 0 to 1 THz. Fig. (3.3) (b) shows the nonlinear delay experienced by the pulse for different intensities with and without nonlinear refractive index dispersion. We can see that the signal experiences a larger delay in the sample with dispersion compared to the sample with a constant n_2 value. The reason is that the field contribution to the nonlinear phase is asymmetric around the peak frequency, thus causing an increased delay in comparison with the flat profile.

The nonlinear delay experienced by the pulse in Figs. (3.2) (b) and (3.3) (b) is calculated as the average time shift compared to the lowest-level signal, as explained in Chapter 2 [79]:

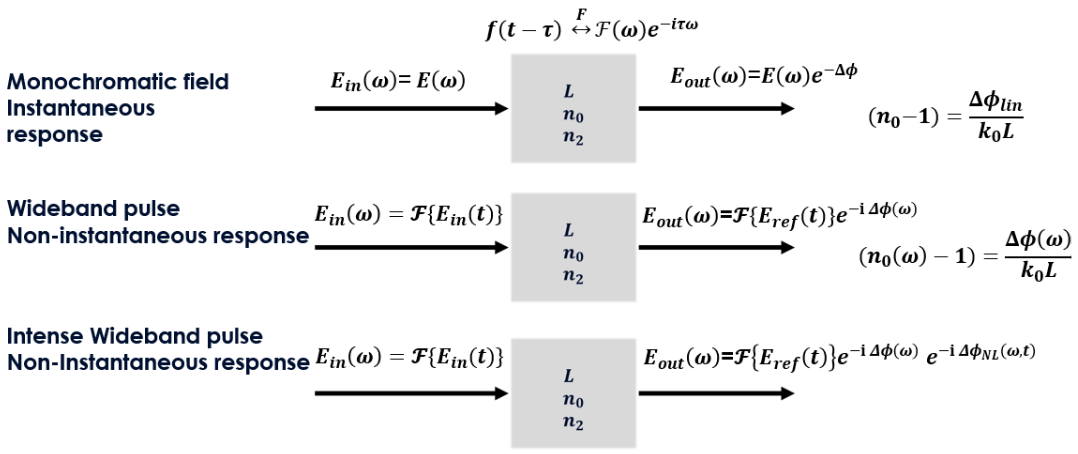

Figure 3.4: THz time-domain spectroscopy: three different cases. For the linear response, the refractive index is calculated from the accumulated phase experienced by the monochromatic field. In the case of a wideband pulse, the Fourier transform is applied, where the phase spectral response gives the refractive index dispersion. In the case of an intense wideband pulse, the field experiences a nonlinear phase shift, which is a function of both frequency and time.

$$t^i_{\mathrm{av}} = \frac{1}{N}\sum_k^N t(E_i = E_k) - t(E_{\mathrm{low}} = E_k). \tag{3.4}$$

Here t^i_{av} is the average time shift, N is the number of data points, E_i is the i-th signal and E_{low} is the lowest-level signal.

3.3 Calculating the Nonlinear Refractive Index Dispersion

The linear refractive index of a material is calculated from the accumulated phase of the signal as it propagates through the sample. In the case of a monochromatic field propagating in a medium with an instantaneous response, the refractive index is simply calculated as $n_0 - 1 = \frac{\Delta\phi_{\mathrm{lin}}}{k_0 L}$, where $\Delta\phi_{\mathrm{lin}}$ is the phase difference between the sample and reference signals. In the case of a wide-band measurement with a non-instantaneous response (dispersive medium), the field after the propagation in the sample is related to the reference signal via Fourier transform [78]:

$$E_{\mathrm{out-lin}}(\omega) = \int \int E_{\mathrm{ref}}(\omega) e^{-i\omega t} d\omega e^{-i\Delta\phi_{\mathrm{lin}}(\omega)} e^{i\omega t} \, \mathrm{d}t, \tag{3.5}$$

where $\Delta\phi_{\mathrm{lin}}(\omega) = (n_0(\omega) - 1)k_0 d$ is the linear phase difference. In the case of the propagation in a nonlinear medium, the output field is expressed as

$$E_{\mathrm{out-NL}}(\omega) = \int \int E_{\mathrm{ref}}(\omega) e^{-i\omega t} d\omega e^{-i\Delta\phi_{\mathrm{lin}}(\omega)} e^{-in_2(\omega)I(t)k_0 d} e^{i\omega t} dt. \tag{3.6}$$

As we can see, the output field experiences an additional nonlinear phase, which is a function of both frequency and time. Thus, the nonlinear refractive index cannot be extracted in a similar manner to the extraction of the linear refractive index. These three cases are summarized in Fig. 3.4.

To analyze the effect of the spectral shape of the signal on the nonlinear phase, we numerically simulate the pulse propagation in a medium with a constant nonlinear refractive index equal to $n_2 = 4 \times 10^{-14}$ m^2/W for all frequencies. An ultrashort THz pulse of 2 ps duration is illustrated in Fig. 3.5 (a) alongside the spectral content of the signal. Fig. 3.5 (b) shows the normalized nonlinear phase obtained from the numerical simulation. Since $\Delta\phi_{\mathrm{NL}}(\omega) \propto \omega \Delta n_{\mathrm{NL}}(\omega)$, the nonlinear phase normalized by the frequency gives the intensity-dependent index change for each frequency component. As can be seen from Fig. 3.5 (b), the normalized phase initially decreases with the frequency at

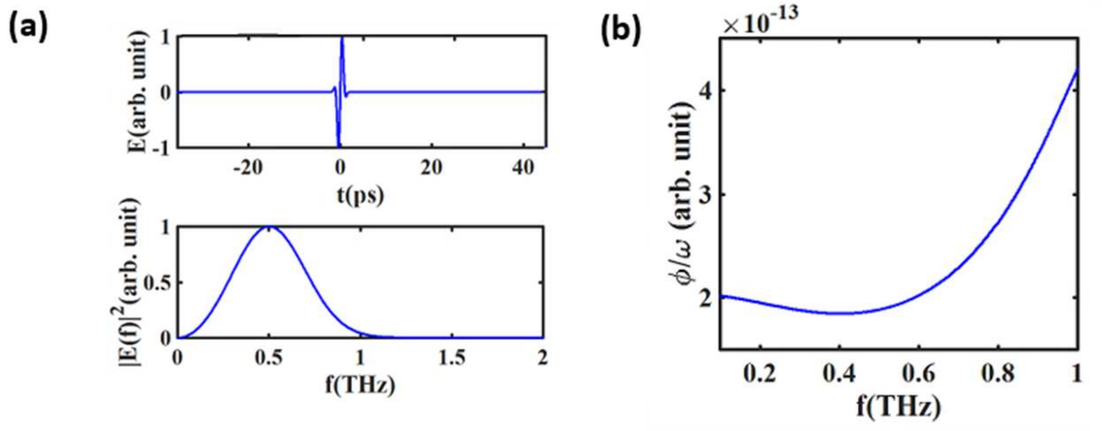

Figure 3.5: (a) Temporal and spectral profile of the input pulse. The 2-ps THz pulse has a 1-THz bandwidth centered at 0.5 THz. (b) The nonlinear phase spectrum normalized by the frequency as a measure of the field contribution to the nonlinear phase.

a very small rate and reaches its minimum at the signal peak frequency, after which it rapidly grows with a further frequency increase. The reason for this behavior is that the cubic signal which is the source of the nonlinearity in the Eq. (3.3) has a peak at a higher frequency compared to the main signal, as previously reported in the paper [66].

In the literature, there have been two approaches taken to calculate the value of the nonlinear refractive index from the phase response. The most common approach is to consider a constant intensity equal to the pulse peak intensity for all the frequencies [53]. Thus, similar to the case of a monochromatic field, the nonlinear refractive index is given by

$$n_2(\omega) = \frac{\Delta\phi_{\mathrm{NL}}}{Ik_0 d}, \tag{3.7}$$

where $\Delta\phi_{\mathrm{NL}}(\omega) = \phi_{\mathrm{tot}} - \phi_{\mathrm{lin}} = k_0(\omega)\Delta n_{\mathrm{NL}}(\omega)d$ is the phase difference between the intense signal and weak signal. We can see that the extracted nonlinear refractive index profile depends only on the phase response and does not take the effect of the spectral content of the pulse into account.

A second approach is to normalize the phase response by the spectral density of the signal in the sharp resonances [49, 68]. In this approximation, dividing the $\phi_{\mathrm{NL}}(\omega)$ by $|E(\omega)|^2$ does not directly result in a parameter with a unit similar to the unit of $|E(t)|^2$. Parseval's theorem requires that $\int_{-\infty}^{\infty} |\mathrm{E}_{\mathrm{THz}}(\mathrm{t})|^2 \, \mathrm{dt} = \int_{-\infty}^{\infty} |\mathrm{E}(\omega)|^2 \mathrm{d}\omega$, meaning that $|E(\omega)|^2$ has to be multiplied by an effective bandwidth and divided by the pulse duration to have the values and units similar to those in the time-domain, as implemented in Ref. [49, 68].

We can start our analysis by assuming that the nonlinear phase is much smaller than 1. Next, we apply Taylor's series expansion for the nonlinear term in Eq. (3.6). After some simplification, we have

$$\frac{E_{\mathrm{out-NL}}(\omega)}{E_{\mathrm{out-lin}}(\omega)} = 1 - i n_2(\omega) \frac{\mathcal{F}(E_{\mathrm{in}}^3)}{\mathcal{F}(E_{\mathrm{in}})} k_0(\omega) n_0(\omega) \varepsilon_0 c d = 1 - i \Delta\phi_{\mathrm{NL}}(\omega). \tag{3.8}$$

Rearranging the terms in Eq. (3.8), we obtain the expression for the dispersion of the nonlinear refractive index:

$$n_2(\omega) = \frac{\Delta\phi_{\mathrm{NL}}(\omega) \mathcal{F}(E(t))}{\omega d \varepsilon_0 n(\omega) \mathcal{F}(E(t)^3)}. \tag{3.9}$$

Next, we simulate THz pulse propagation in a medium with linear absorption and a nonlinear dispersion. The linear extinction coefficient for the medium is set to $\kappa = 0.01$, and the arbitrary nonlinear refractive index has a dispersion with a profile similar to the profile described in Fig. 3.3. The goal is to calculate this arbitrary n_2 dispersion

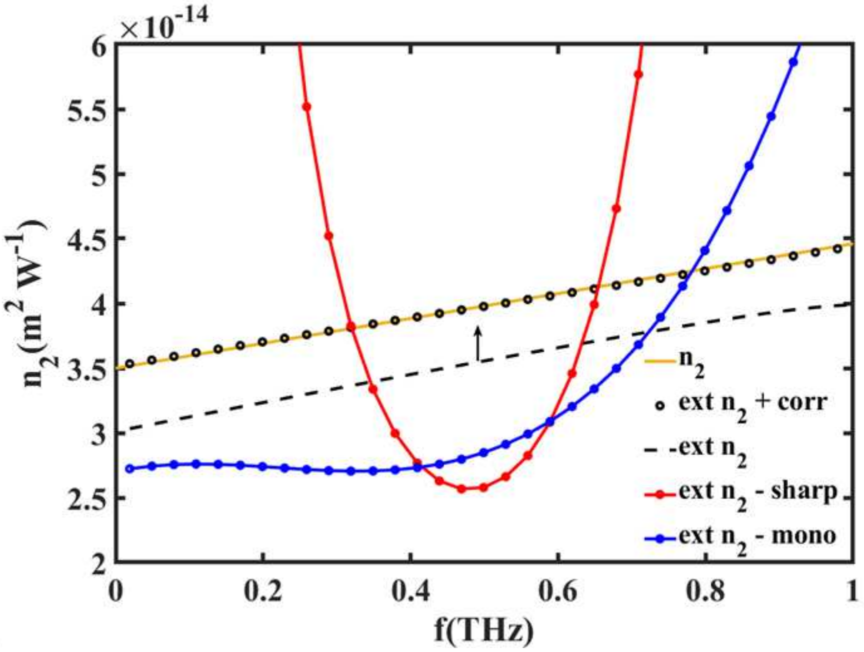

Figure 3.6: The dispersion of n_2 calculated using different methods. The graph displays the arbitrary dispersion profile (orange), monochromatic approximation (blue), sharp-resonance approximation (red), Fourier method expressed by Eq. (3.9) (dashed), and the modified Fourier method expressed by Eq. (3.12) (black circles).

from the phase response of the simulation. Next, we calculate the nonlinear refractive dispersion using the two common methods described above and the derived expression in Eq. (3.9). Fig. 3.6 compares these calculation methods for the nonlinear refractive index. The sharp-resonance (red), as expected, has the worst accuracy for a single-cycle broadband THz signal and diverges rapidly. The method has its best accuracy for the many-cycle signals where the pulse has a sufficiently narrow bandwidth or for the cases where a medium with sharp resonances, such as water vapor, is studied [49]. The monochromatic approximation (blue) ignores the field spectral profile and calculates a dispersion profile similar to the normalized nonlinear phase, shown in Fig. 3.5 (b). The dispersion calculated using Eq. (3.9) (dashed line) is smaller than the initial arbitrary profile (orange) due to the linear absorption. We may correct this shift with the introduction of an absorption term to Eq. (3.9). Assuming that the induced nonlinear phase depends only on the field amplitude, and the field evolution is not significant, we can calculate the effective absorption for the process. If we assume the absorption term to be $\mathrm{e}^{-\frac{\alpha x}{2}}$, the average absorption for the propagation length d can be calculated as

$$A_{av} = \frac{\int_0^d e^{-\frac{\alpha x}{2}} dx}{d} \approx \frac{1 - (1 - \frac{\alpha d}{2} + \frac{\alpha^2 d^2}{8})}{\frac{\alpha d}{2}} = 1 - \frac{\alpha d}{4} \approx e^{-\alpha \frac{d}{4}}. \tag{3.10}$$

Applying the average absorption to the signal, we can calculate the correction term. The electric field in Eq. (3.9) is substituted by the new field calculated as

$$E_{\text{new}}(t) = \mathcal{F}^{-1}\left(e^{-\frac{\alpha(\omega)d}{4}} \mathcal{F}\left[E(t)\right]\right). \tag{3.11}$$

Thus, the expression for the dispersion of the nonlinear refractive index is given by

$$n_2(\omega) = \frac{\Delta\phi_{\text{NL}}(\omega)\mathcal{F}(E_{\text{new}}(t))}{\omega d \varepsilon_0 n(\omega)\mathcal{F}(E_{\text{new}}(t)^3)}. \tag{3.12}$$

As can be seen from Fig. 3.5, the modified expression extracts the correct values of the nonlinear refractive index (black circles).

3.4 Extraction of n_2 Dispersion from the Experimental Data Obtained from BK7

In this section, we apply the method, developed above, to the experimental data obtained from the nonlinear THz spectroscopy of a 1-mm-thick BK7 sample. BK7 is an amorphous borosilicate glass with a refractive index of 2.51 at the THz frequencies [80]. Due to its alkali network modifiers, it exhibits a high refractive index and absorption coefficient at the THz frequencies [81], which makes it a good candidate for the nonlinear characterization such as the Kerr coefficient measurement, as it has been previously shown in a similar material family of chalcogenide glasses [57]. Due to the disorder-induced coupling of the far-IR radiation into the phonon modes in the amorphous materials, the refractive index and absorption coefficient frequency dependence is described by the power-law relation [81]:

$$n(\omega)\alpha(\omega) = K\omega^{\beta}, \tag{3.13}$$

where β is the power constant that is dependent on the glass composition and the coefficient K is a measure of disorder in the material. For BK7, the power constant is $\beta \approx 2.3$ [82, 83].

Fig. 3.7 demonstrates the temporal signal and absorption profile of BK7 for different field amplitudes. The power coefficient β is approximately 2.2. The absorption increases with an increase of the field amplitude, while the power coefficient does not show any significant change.

Fig. 3.8 (a) shows the nonlinear phase normalized by the frequency for each signal level. As can be seen from the figure, due to the BK7 absorption spectrum, the profile of the normalized phase is totally different from the phase response we previously observed in Fig. 3.5 (b), highlighting the effect of the absorption spectrum on the nonlinear phase.

We next perform the calculation of n_2 dispersion from the phase response for each intensity level via Eq. (3.12). Finally, we averaged the n_2 values calculated from all signal levels. The averaged dispersion is shown in Fig. 3.8 (b) where the error bars are the standard deviation of the averaged n_2 for different intensities. The extracted n_2 of

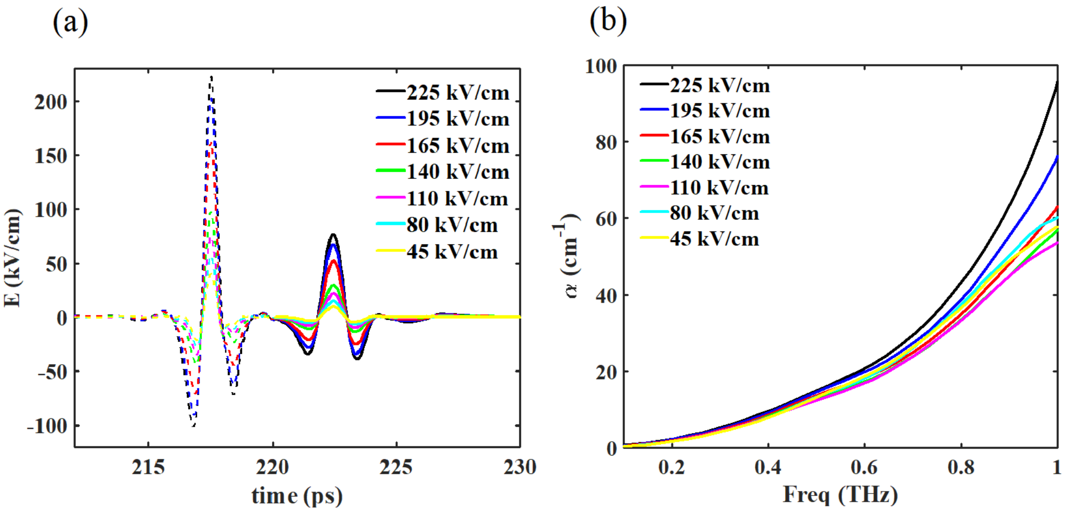

Figure 3.7: THz nonlinear time-domain spectroscopy of BK7 for different field amplitudes. (a) THz temporal signal in free space (dashed) and BK7 sample (solid) for different signal levels (b) Absorption coefficient profile for different signal levels. The power coefficient β is approximately 2.2.

BK7 is averaged over different signal levels and is estimated to be $n_2 = 4 \times 10^{-14}\,\mathrm{m}^2/\mathrm{W}$. The dispersion profile has a very small slope and appears to be relatively flat. This can be explained by the fact that the frequency range at which the nonlinear measurements have been performed lies far away from the material resonances. This is also true for the linear dispersion of BK7 and other amorphous glasses at low frequencies [81, 82].

3.5 Conclusions

In this chapter, we studied the effect of the nonlinear refractive index dispersion on the nonlinear THz-TDS. A numerical method based on Fourier analysis was presented to simulate the propagation of a wideband THz pulse in a nonlinear medium. The introduction of the dispersion profile to the nonlinear refractive index leads to a larger delay

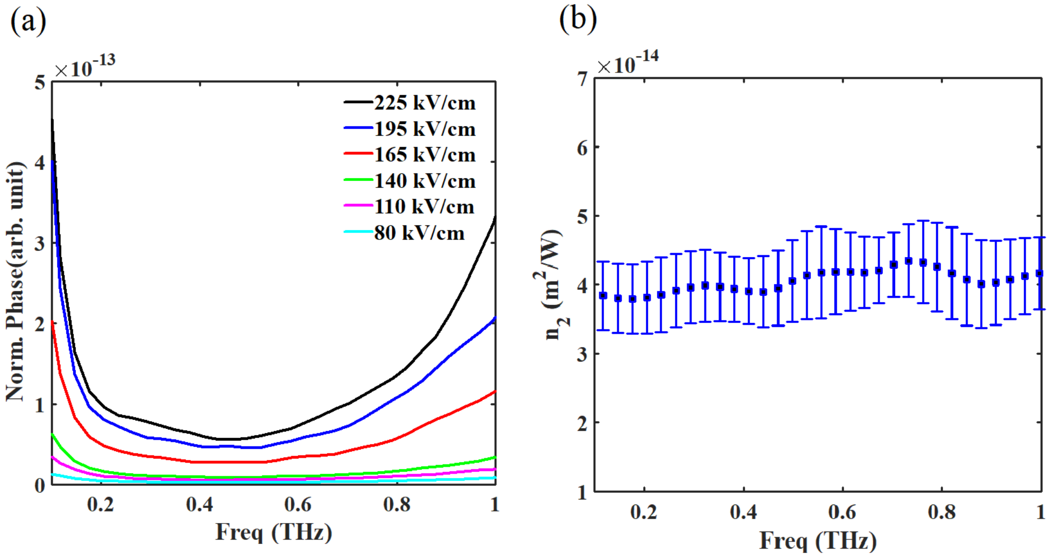

Figure 3.8: THz nonlinear response of BK7. (a) The nonlinear phase normalized by the frequency. (b) The extracted nonlinear refractive index averaged over calculated values for different intensities. The dispersion is not significant as the measurement frequency range lies within the resonance tail.

experienced by the pulse. Next, we analyzed the phase response of the sample for a constant n_2. We noticed that the nonlinear phase spectrum does not resemble the spectral shape of the signal and also differs significantly for different frequencies. Then, based on the same Fourier analysis, we derived an expression for the nonlinear dispersion and compared it with the two most common methods: monochromatic and sharp-resonance approximations. The proposed method was shown to have a much better performance for the broadband measurements. Finally, we applied the proposed method to the experimental data in BK7. In the measurement frequency range, the nonlinear refractive index has a small dispersion and is estimated to be $n_2 = 4 \times 10^{-14}\ \mathrm{m}^2/\mathrm{W}$. This study enables us to calculate the n_2 values precisely by factoring out the effect of the pulse spectrum in phase response.

Chapter 4

THZ-INDUCED MECHANISMS OF THE THIRD-ORDER NONLINEAR INTERACTIONS

4.1 Introduction

Different THz-field-induced nonlinear effects described by the third-order nonlinear susceptibility have been reported in three main categories. The first category of the observed effects is the THz-induced Kerr effect at the optical frequencies. These effects are described by the third-order susceptibility in the form of $\chi^{(3)}(\omega_{\mathrm{opt}}, \omega_{\mathrm{THz}}, -\omega_{\mathrm{THz}}, \omega_{\mathrm{opt}})$, as shown in Fig. (4.1). In this configuration, a strong THz pump beam copropagates with a weak optical beam inside the sample. The optical beam experiences a THz-induced birefringence proportional to the intensity of the THz field. Similar to electro-optic sampling, the birefringence is converted into the intensity difference after passing through a quarter-wave plate and then a polarizing beam-splitter. The differential electric signal detected in the balanced photo-detector is called Kerr signal. The temporal shape of the THz-induced Kerr signal has the intensity profile of the THz pulse with a signal peak value proportional to the square of the THz field amplitude, E_{THz}^2 [40].

The second category of the THz-induced effects is the THz field-induced second-harmonic (TFISH) generation where the associated nonlinear susceptibility takes the form $\chi^{(3)}(2\omega_{\mathrm{Opt}} + \omega_{\mathrm{THz}}, \omega_{\mathrm{Opt}}, \omega_{\mathrm{Opt}}, \omega_{\mathrm{THz}})$, as shown in Fig. 4.2. In this configuration, an optical probe beam, copropagating with the THz beam inside the sample, produces a

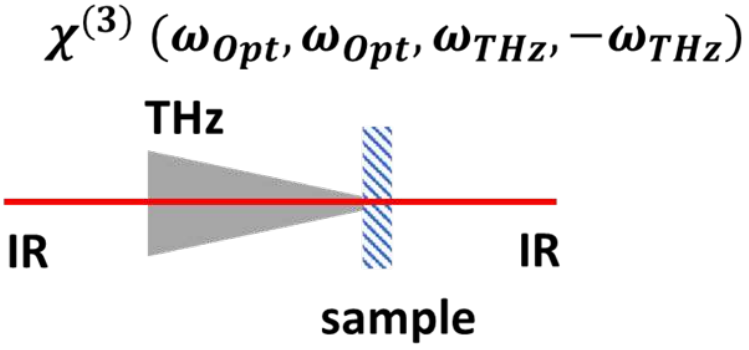

Figure 4.1: THz Kerr configuration. A strong THz pump beam copropagates with a weak optical probe beam. The optical beam experiences a THz-induced birefringence. Similar to the electro-optic sampling scheme, this birefringence is translated and detected as an electric signal using a quarter-wave plate, a polarizing beam-splitter and a pair of balanced photo-detector. The detected signal that is called Kerr signal replicates the temporal form of the field intensity with a peak value proportional to the THz beam intensity.

THz-induced second-harmonic generation. This effect is the extension of a DC electric field-induced second-harmonic generation (EFISH) [84]. Then, using a band-pass filter, the probe beam is filtered out and the second-harmonic signal is detected using a photomultiplier tube.

One can remove the sample and introduce a static bias field at the place of the sample to modify the TFISH technique for coherent detection of the THz field, in a technique known as air-biased coherent detection (ABCD) [22].

The third category of the THz-induced nonlinear effects is the nonlinear refractive index n_2 at the THz frequencies, represented by the third-order susceptibility in the form of $\chi^{(3)}(\omega_{\mathrm{THz}}, \omega_{\mathrm{THz}}, \omega_{\mathrm{THz}}, -\omega_{\mathrm{THz}})$. This group of effects is studied thoroughly in Chapter 2 and Chapter 3 and also in the published work [79]. Fig. 4.3 shows the configuration corresponding this group. The nonlinear sample is placed at the main focal point of the

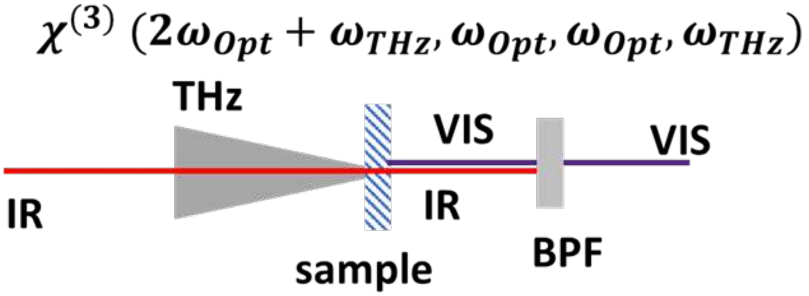

Figure 4.2: THz-field-induced second-harmonic (TFISH) generation configuration. The co-propogating optical probe and THz beams cause an optical second-harmonic generation. Next, the fundamental frequency is filtered out while the second-harmonic beam is detected in a photo-multiplier tube.

THz beam. As the intense THz beam propagates through the sample, the refractive index is modified with an intensity-dependent term. Thus, after passing through the sample, the THz frequency components have additional phases in comparison to the linear phase experienced by the lowest-level signal. In simple terms, the intensity-dependent change in the refractive index is sensed by the same THz beam. Then, the THz field is detected using the electro-optic (EO) sampling technique [85, 16]. In this technique, the THz field amplitude is decreased either by a THz-field attenuation using Si wafers or by decreasing the magnification using an off-axis parabolic mirror with a larger focal length, as shown schematically in Fig. 4.3, in order to avoid over-rotation and THz-induced nonlinear effects in the detection crystal. As we can see, in this effect the intense THz beam acts as both the pump and probe beam, and the EO sampling is only used to record the THz temporal signal.

Looking at these three categories, one could deduce that the distinguishing factor is the frequency of the probe beam. In the THz-induced Kerr effect, there is a THz-field-induced intensity-dependent refractive index sensed by the optical probe beam. In

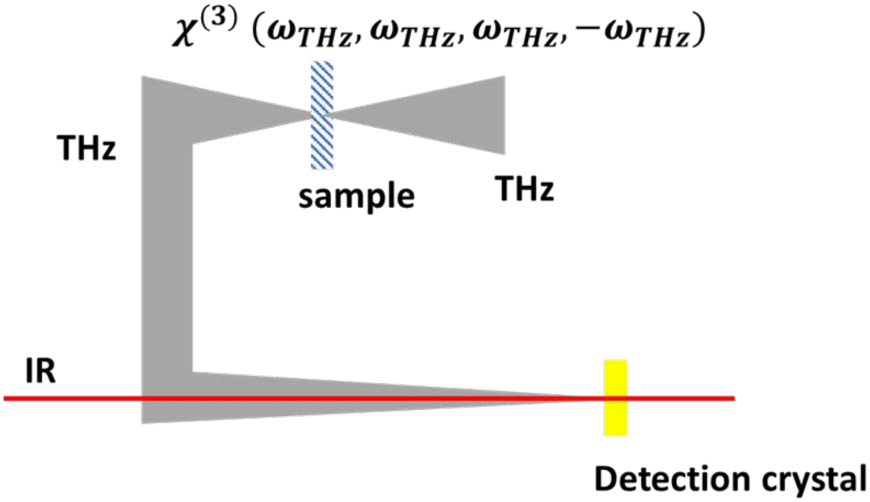

Figure 4.3: A schematic of THz nonlinear refraction. An intense THz pulse passes through a sample and experiences a nonlinear phase shift in addition to the linear phase shift, acquired by the pulse on propagation regardless of the THz intensity level. The temporal waveform of the THz pulse is detected via EO sampling.

TFISH, the THz field linearly contributes to the optical second-harmonic generation. This linear dependence of the TFISH technique on the THz field makes it possible for TFISH to be used for coherent detection of the THz field [14, 86, 87]. Thus, one can conclude that the probe frequency for this THz effect is twice the optical frequency. In the THz nonlinear refraction, the THz-induced intensity-dependent index change is sensed by the same THz field. Thus, the probe beam is at the THz frequency.

In this chapter, we explore these three groups of third-order nonlinear interactions and explain how these effects are related to each other. First, using the Lorentz oscillator model, we derive the relationship between the third-order susceptibility corresponding to the THz nonlinear refractive index and the third-order susceptibilities corresponding to the TFISH and use this model to theoretically predict the value of TFISH susceptibility of $\mathrm{SiO_2}$ at its dominant resonance frequency. Next, by using a similar approach we extend our study to the relationship between the susceptibilities representing THz nonlinear refraction and THz-induced Kerr effect. This work categorizes the third-order THz-induced nonlinear interactions based on the probe frequency and explains the dependency of the nonlinear susceptibility values on it, which is a significant contribution targeting the consistency of the reported values in the literature.

Publication: B. Zhou, M. Rasmussen, **S. Zibod**, S. Yan, N. Noori, O. Nagy, Y. Ding, S. Lange, K. Dolgaleva, R. Boyd, and P. Uhd Jepsen, "Measurement of the dispersion of $\chi(3)$ of SiO2 and SiN across the THz and far-infrared frequency bands," Laser and Photonics Reviews, Jul 2024.

4.2 THz Field-Induced Second-Harmonic Generation

This project originated from a collaboration with Prof. Jepsen's group at DTU where they requested us to adapt our theoretical model, described in Chapter 2, to validate their experimental measurement results on TFISH in solids. Their proposed novel technique is based on the solid-state biased coherent detection (SSBCD), where the measured SHG signal of the probe beam is linearly proportional to the incident THz signal [88, 89]. In the proposed method, the ratio between the TFISH signals detected in the SSBCD and

ABCD is used to extract the third-order complex susceptibility corresponding to the TFISH in a solid-state material such as $\mathrm{SiO_2}$. Using the two-color air-plasma generation method [90, 91] and SSBCD/ABCD detection scheme, the measurement is performed over an ultra-wideband range of 1-50 THz, covering the resonance frequencies of different materials in THz and Far-IR frequency ranges. The question concerned the measured value of $5.5 \times 10^{-22}\ \mathrm{m^2/V^2}$ for the susceptibility corresponding to TFISH in $\mathrm{SiO_2}$ at its dominant resonance at 37.2 THz [74].

The theoretical modeling starts with anharmonic oscillator as described in [62] and Chapter 2,

$$\ddot{x} + 2\gamma\dot{x} + \omega_0^2 x + ax^2 + bx^3 = \alpha E(t), \tag{4.1}$$

where x is the ion displacement from the equilibrium position, γ is the damping factor, ω_0 is the resonance frequency, $E(t)$ is the applied field and a and b are the second- and third-order nonlinear coefficients, respectively. For simplicity, we assume there is a dominant resonance at 37.2 THz. The parameter α on the right-hand side of Eq. (4.1) is determined as $\alpha = q/m$, where q and m are the effective electric coupling strength and effective reduced mass of the mode, respectively. We assume that the applied field is given by

$$E(t) = E_{\mathrm{THz}} e^{-i\omega_{\mathrm{THz}} t} + E_{\mathrm{Opt}} e^{-i\omega_{\mathrm{Opt}} t} + \text{c.c.}, \tag{4.2}$$

where the field has two frequency components, one in the THz range and the other one in the optical range. Applying perturbation theory and introducing the expansion parameter $0 \leq \lambda \leq 1$, we seek a solution to Eq. (4.1) in the form of the power-series expansion with respect to λ:

$$x(t) = \lambda x^{(1)}(t) + \lambda^2 x^{(2)}(t) + \lambda^3 x^{(3)}(t) + \cdots. \tag{4.3}$$

Here the first-order, second-order and third-order ion deviations are given by [92]

$$x^{(1)}(t) = x^{(1)}(\omega_{THz})e^{-i\omega_{THz}t} + x^{(1)}(\omega_{Opt})e^{-i\omega_{Opt}t} + \text{c.c.}, \tag{4.4a}$$

$$x^{(2)}(t) = \sum_p x^{(2)}(\omega_p)e^{-i\omega_p t} + \text{c.c.}, \tag{4.4b}$$

and

$$x^{(3)}(t) = \sum_q x^{(3)}(\omega_q)e^{-i\omega_q t} + \text{c.c.}, \tag{4.4c}$$

respectively. The second-order correction term oscillation has frequencies denoted by $\omega_p = \omega_j + \omega_k$, where ω_j and ω_k would take any values of $\pm\,\omega_{\text{THz}}$ and $\pm\,\omega_{\text{Opt}}$. In the same manner, $\omega_q = \omega_l + \omega_m + \omega_n$ is the oscillation frequency of the third-order correction term, where $\omega_l,\ \omega_m$ and $\omega_n$would take any values of $\pm\,\omega_{\text{THz}}$ and $\pm\,\omega_{\text{Opt}}$. After substituting x in Eq. (4.1), we sort and split the terms with respect to the power of λ into three equations:

$$\ddot{x}^{(1)} + 2\gamma\dot{x}^{(1)} + \omega_0^2 x^{(1)} = \alpha E, \tag{4.5a}$$

$$\ddot{x}^{(2)} + 2\gamma\dot{x}^{(2)} + \omega_0^2 x^{(2)} + a[x^{(1)}]^2 = 0, \tag{4.5b}$$

and

$$\ddot{x}^{(3)} + 2\gamma\dot{x}^{(3)} + \omega_0^2 x^{(3)} + 2ax^{(1)}x^{(2)} + b[x^{(1)}]^3 = 0. \tag{4.5c}$$

Eq. (4.5a) gives the steady-state solution at the fundamental frequencies in the form of

$$x^{(1)}(\omega_{\mathrm{THz}}) = \frac{\alpha E_{\mathrm{THz}}}{\omega_0^2 - \omega_{\mathrm{THz}}^2 - 2i\gamma\omega_{\mathrm{THz}}} \tag{4.6a}$$

for the THz frequency and

$$x^{(1)}(\omega_{\mathrm{Opt}}) = \frac{\alpha E_{\mathrm{Opt}}}{\omega_0^2 - \omega_{\mathrm{Opt}}^2 - 2i\gamma\omega_{\mathrm{Opt}}} \tag{4.6b}$$

for the optical frequency. Substituting Eqs. (4.6a) and (4.6b) into Eq. (4.5b), we find the second-order correction terms for the components oscillating at the frequencies $2\omega_{\mathrm{THz}}$ and $2\omega_{\mathrm{Opt}}$:

$$x^{(2)}(2\omega_{\mathrm{THz}}) = -\frac{a\alpha^2 E_{\mathrm{THz}}^2}{(\omega_0^2 - \omega_{\mathrm{THz}}^2 - 2i\gamma\omega_{\mathrm{THz}})^2(\omega_0^2 - 4\omega_{\mathrm{THz}}^2 - 4i\gamma\omega_{\mathrm{THz}})} \tag{4.7a}$$

and

$$x^{(2)}(2\omega_{\mathrm{Opt}}) = -\frac{a\alpha^2 E_{\mathrm{Opt}}^2}{(\omega_0^2 - \omega_{\mathrm{Opt}}^2 - 2i\gamma\omega_{\mathrm{Opt}})^2(\omega_0^2 - 4\omega_{\mathrm{Opt}}^2 - 4i\gamma\omega_{\mathrm{Opt}})}. \tag{4.7b}$$

The optical rectification terms at zero frequency induced by the THz and optical beams are described as

$$x^{(2)}(0, \omega_{\mathrm{THz}}, -\omega_{\mathrm{THz}}) = -2\frac{a\alpha^2 E_{\mathrm{THz}}^2}{(\omega_0^2 - \omega_{\mathrm{THz}}^2 - 2i\gamma\omega_{\mathrm{THz}})(\omega_0^2 - \omega_{\mathrm{THz}}^2 + 2i\gamma\omega_{\mathrm{THz}})\omega_0^2} \tag{4.8a}$$

and

$$x^{(2)}(0, \omega_{\mathrm{Opt}}, -\omega_{\mathrm{Opt}}) = -2\frac{a\alpha^2 E_{\mathrm{Opt}}^2}{(\omega_0^2 - \omega_{\mathrm{Opt}}^2 - 2i\gamma\omega_{\mathrm{Opt}})(\omega_0^2 - \omega_{\mathrm{Opt}}^2 + 2i\gamma\omega_{\mathrm{Opt}})\omega_0^2}, \tag{4.8b}$$

respectively. Finally, the solution at frequencies $\omega_{\mathrm{Opt}} \pm \omega_{\mathrm{THz}}$ is given by

$$x^{(2)}(\omega_{\mathrm{Opt}} \pm \omega_{\mathrm{THz}}) = -2\frac{a\alpha^2 E_{\mathrm{Opt}} E_{\mathrm{THz}}}{(\omega_0^2 - \omega_{\mathrm{Opt}}^2 - 2i\gamma\omega_{\mathrm{Opt}})^2(\omega_0^2 - \omega_{\mathrm{THz}}^2 \mp 2i\gamma\omega_{\mathrm{THz}})}, \tag{4.9}$$

where the approximation $\omega_{\mathrm{Opt}} \pm \omega_{\mathrm{THz}} \approx \omega_{\mathrm{Opt}}$ was applied.

Knowing all the second-order correction terms, we plug $x^{(2)}(t)$ into Eq. (4.5c) and find the third-order correction-terms. There are many frequency components resulting from the third-order processes described in Eq. (4.5c). However, there are only two frequencies of direct interest to this study, ω_{THz} and $2\omega_{\mathrm{Opt}} + \omega_{\mathrm{THz}}$:

$$\begin{aligned}
x^{(3)}(\omega_{\mathrm{THz}}) = {} & \Bigg[\frac{2a^2\alpha^3}{(\omega_0^2 - \omega_{\mathrm{THz}}^2 - 2i\gamma\omega_{\mathrm{THz}})^3(\omega_0^2 - \omega_{\mathrm{THz}}^2 + 2i\gamma\omega_{\mathrm{THz}})} \frac{(3\omega_0^2 - 8\omega_{\mathrm{THz}}^2 - 8i\gamma\omega_{\mathrm{THz}})}{\omega_0^2(\omega_0^2 - 4\omega_{\mathrm{THz}}^2 - 4i\gamma\omega_{\mathrm{THz}})} \\
& + \frac{3b\alpha^3}{(\omega_0^2 - \omega_{\mathrm{THz}}^2 - 2i\gamma\omega_{\mathrm{THz}})^3(\omega_0^2 - \omega_{\mathrm{THz}}^2 + 2i\gamma\omega_{\mathrm{THz}})} \Bigg] |E_{\mathrm{THz}}|^2 E_{\mathrm{THz}} \\
& + \Bigg[\frac{4a^2\alpha^3(2\omega_0^2 - \omega_{\mathrm{Opt}}^2 - 2i\gamma\omega_{\mathrm{Opt}})}{\omega_0^2(\omega_0^2 - \omega_{\mathrm{THz}}^2 - 2i\gamma\omega_{\mathrm{THz}})^2(\omega_0^2 - \omega_{\mathrm{Opt}}^2 - 2i\gamma\omega_{\mathrm{Opt}})^2(\omega_0^2 - \omega_{\mathrm{Opt}}^2 + 2i\gamma\omega_{\mathrm{Opt}})} \\
& + \frac{3b\alpha^3}{(\omega_0^2 - \omega_{\mathrm{Opt}}^2 + 2i\gamma\omega_{\mathrm{Opt}})(\omega_0^2 - \omega_{Opt}^2 - 2i\gamma\omega_{\mathrm{Opt}})} \\
& \times \frac{1}{(\omega_0^2 - \omega_{\mathrm{THz}}^2 - 2i\gamma\omega_{\mathrm{THz}})^2} \Bigg] |E_{\mathrm{Opt}}|^2 E_{\mathrm{THz}}; \qquad (4.10)
\end{aligned}$$

$$\begin{aligned}
x^{(3)}(2\omega_{\mathrm{Opt}} + \omega_{\mathrm{THz}}) = {} & \Bigg[\frac{2a^2\alpha^3}{(\omega_0^2 - \omega_{\mathrm{THz}}^2 - 2i\gamma\omega_{\mathrm{THz}})(\omega_0^2 - \omega_{\mathrm{Opt}}^2 - 2i\gamma\omega_{\mathrm{Opt}})^3} \\
& \times \frac{(3\omega_0^2 - 9\omega_{\mathrm{Opt}}^2 - 10i\gamma\omega_{\mathrm{Opt}})}{(\omega_0^2 - 4\omega_{\mathrm{Opt}}^2 - 4i\gamma\omega_{\mathrm{Opt}})^2} \\
& + \frac{3b\alpha^3}{(\omega_0^2 - \omega_{\mathrm{Opt}}^2 - 2i\gamma\omega_{\mathrm{Opt}})^2(\omega_0^2 - 4\omega_{\mathrm{Opt}}^2 - 4i\gamma\omega_{\mathrm{Opt}})} \\
& \times \frac{1}{(\omega_0^2 - \omega_{\mathrm{THz}}^2 - 2i\gamma\omega_{\mathrm{THz}})} \Bigg] E_{\mathrm{THz}} E_{\mathrm{Opt}}^2. \qquad (4.11)
\end{aligned}$$

In Eq. (4.10), the first bracket represents the THz-induced correction term, while the second bracket shows the optically induced nonlinear term, which could be ignored with controlling the intensity of the probe beam. The relationship between the nonlinear susceptibility and deviation is given by

$$P_{\mathrm{NL}} = Nqx^{(3)} = 3\chi^{(3)}|E|^2E. \tag{4.12}$$

Thus, the nonlinear susceptibility can be expressed as

$$\chi^{(3)}(\omega_{\mathrm{THz}}, \omega_{\mathrm{THz}}, -\omega_{\mathrm{THz}}, \omega_{\mathrm{THz}}) = \frac{qN}{3} \frac{\alpha^3}{(\omega_0^2 - \omega_{\mathrm{THz}}^2 - 2i\gamma\omega_{\mathrm{THz}})^3(\omega_0^2 - \omega_{\mathrm{THz}}^2 + 2i\gamma\omega_{\mathrm{THz}})} \tag{4.13}$$

$$\left[2a^2 \frac{(3\omega_0^2 - 8\omega_{\mathrm{THz}}^2 - 8i\gamma\omega_{\mathrm{THz}})}{\omega_0^2(\omega_0^2 - 4\omega_{\mathrm{THz}}^2 - 4i\gamma\omega_{\mathrm{THz}})} + 3b\right].$$

The calculation of a is straightforward and presented in [62]. The direct-process contribution to the susceptibility at low frequencies is given by

$$\chi_{\mathrm{Direct}}^{(3)\omega\ll\omega_0} = \frac{qN}{3}\frac{3b\alpha^3}{\omega_0^8} = \frac{n_0}{3\pi}n_{2,v}^{(2)} = -\frac{2N|\mu|^4}{3\hbar^3\omega_0^3}, \tag{4.14}$$

where the dipole moment μ is related to the linear susceptibility via [92]

$$\chi^{(1)} = \frac{N}{3\hbar}\sum_n |\mu_n a|^2 \left[\frac{1}{(\omega_{na} - \omega) - i\gamma} + \frac{1}{(\omega_{na} + \omega) + i\gamma}\right]. \tag{4.15}$$

In the low-frequency regime, Eq. (4.15) can be simplified as

$$\chi^{(1),\omega\ll\omega_0} = \frac{2N|\mu|^2}{3\hbar\omega_0}. \tag{4.16}$$

Plugging Eq. (4.16) into (4.13) and replacing $\chi^{(1)\omega\ll\omega_0}$ with $\frac{1}{4\pi}\left[(n_0^{\omega\ll\omega_0})^2 - 1\right]$, where

$n_0^{\omega\ll\omega_0}$ is calculated as presented in [62], we obtain:

$$\begin{aligned}\chi_{\text{Direct}}^{(3)\omega\ll\omega_0} &= \frac{qN}{3}\frac{3b\alpha^3}{\omega_0^8} = -\frac{3(\chi^{(1)\omega\ll\omega_0})^2}{2N\hbar\omega_0} \\ &= -\frac{3\left[(n_0^{\omega\ll\omega_0})^2-1\right]^2}{2N\hbar\omega_0(4\pi)^2} = -\frac{3\left[(n_0^{\omega\ll\omega_0})^2-1\right]^2}{32N\hbar\omega_0\pi^2}.\end{aligned} \tag{4.17}$$

For THz frequencies $\omega_{\text{THz}} \ll \omega_0$, the ratio between the second term, describing the direct process, and the first term, describing the cascaded process, in the first bracket is found as

$$\begin{aligned}\frac{\chi^{(3)}(\omega_{\text{THz}})_{\text{Direct}}}{\chi^{(3)}(\omega_{\text{THz}})_{\text{Cascaded}}} &= \frac{3b}{2a^2}\frac{\omega_0^2(\omega_0^2-4\omega_{\text{THz}}^2-4i\gamma\omega_{\text{THz}})}{(3\omega_0^2-8\omega_{\text{THz}}^2-8i\gamma\omega_{\text{THz}})}\Bigg|_{(\omega_{\text{THz}}\ll\omega_0)} \\ &= \frac{b\omega_0^2}{2a^2} = \frac{-3.27\times10^{-11}}{2.24\times10^{-9}} \approx -0.015.\end{aligned} \tag{4.18}$$

It is implied that at the THz frequencies $\omega_{\text{THz}} \ll \omega_0$, and the direct contribution could be neglected with respect to the cascaded process. However, in the vicinity of the resonance frequency, one has to take into account the direct contribution, and Eq. (4.15) takes the general form

$$\begin{aligned}\chi^{(1)}(\omega) &= \frac{2N|\mu|^2\omega_0}{3\hbar(\omega_0^2-\omega^2-2i\gamma\omega)} = \chi^{(1)\omega\ll\omega_0}\frac{\omega_0^2}{(\omega_0^2-\omega^2-2i\gamma\omega)} \\ &= \frac{1}{4\pi}\left[(n_0^{\omega\ll\omega_0})^2-1\right]\frac{\omega_0^2}{(\omega_0^2-\omega^2-2i\gamma\omega)}.\end{aligned} \tag{4.19}$$

Substituting Eq. (4.19) into Eq. (4.17), we obtain:

$$\left(\frac{qN}{3}\right)3b\alpha^3 = -\frac{3(\chi^{(1)})^2}{2N\hbar\omega_0} = -\frac{3\left[(n_0^{\omega\ll\omega_0})^2-1\right]^2}{32N\hbar\pi^2}\frac{\omega_0^{11}}{(\omega_0^2-\omega^2-2i\gamma\omega)^2}. \tag{4.20}$$

The third-order susceptibility as a function of frequency can be calculated by substituting Eq. (4.20) into Eq. (4.13):

$$\begin{aligned}
\chi^{(3)}(\omega_{\mathrm{THz}},\omega_{\mathrm{THz}},-\omega_{\mathrm{THz}},\omega_{\mathrm{THz}}) &= \frac{1}{(\omega_0^2-\omega_{\mathrm{THz}}^2-2i\gamma\omega_{\mathrm{THz}})^3(\omega_0^2-\omega_{\mathrm{THz}}^2+2i\gamma\omega_{\mathrm{THz}})} \\
&\left[\frac{qN\alpha^3}{3}\times 2a^2\frac{(3\omega_0^2-8\omega_{\mathrm{THz}}^2-8i\gamma\omega_{\mathrm{THz}})}{\omega_0^2(\omega_0^2-4\omega_{\mathrm{THz}}^2-4i\gamma\omega_{\mathrm{THz}})}+\frac{qN\alpha^3}{3}\times 3b\right] \\
&= \frac{1}{(\omega_0^2-\omega_{\mathrm{THz}}^2-2i\gamma\omega_{\mathrm{THz}})^3(\omega_0^2-\omega_{\mathrm{THz}}^2+2i\gamma\omega_{\mathrm{THz}})} \\
&\left[\frac{qN\alpha^3}{3}\times 2a^2\frac{(3\omega_0^2-8\omega_{\mathrm{THz}}^2-8i\gamma\omega_{\mathrm{THz}})}{\omega_0^2(\omega_0^2-4\omega_{\mathrm{THz}}^2-4i\gamma\omega_{\mathrm{THz}})}\right. \\
&\left.-\frac{3\left[(n_0^{\omega\ll\omega_0})^2-1\right]^2}{32N\hbar\pi^2}\frac{\omega_0^{11}}{(\omega_0^2-\omega_{\mathrm{THz}}^2-2i\gamma\omega_{\mathrm{THz}})^2}\right].
\end{aligned} \tag{4.21}$$

Using Eqs. (4.11) and (4.20), one can write the nonlinear susceptibility corresponding to the THz-field-induced SHG as

$$\begin{aligned}
\chi^{(3)}(2\omega_{\mathrm{Opt}}+\omega_{\mathrm{THz}}) &= \left[\frac{qN}{3}\frac{2a^2\alpha^3}{(\omega_0^2-\omega_{\mathrm{THz}}^2-2i\gamma\omega_{\mathrm{THz}})(\omega_0^2-\omega_{\mathrm{Opt}}^2-2i\gamma\omega_{\mathrm{Opt}})^3}\right. \\
&\times\frac{(3\omega_0^2-9\omega_{\mathrm{Opt}}^2-10i\gamma\omega_{\mathrm{Opt}})}{(\omega_0^2-4\omega_{Opt}^2-4i\gamma\omega_{\mathrm{Opt}})^2}+\frac{qN}{3}\frac{3b\alpha^3}{(\omega_0^2-\omega_{\mathrm{THz}}^2-2i\gamma\omega_{\mathrm{THz}})(\omega_0^2-\omega_{\mathrm{Opt}}^2-2i\gamma\omega_{\mathrm{Opt}})^2} \\
&\left.\times\frac{1}{(\omega_0^2-4\omega_{\mathrm{Opt}}^2-4i\gamma\omega_{\mathrm{Opt}})}\right] \\
&= \left[\frac{qN}{3}\frac{2a^2\alpha^3}{(\omega_0^2-\omega_{\mathrm{THz}}^2-2i\gamma\omega_{\mathrm{THz}})}\frac{9}{16\omega_{Opt}^8}+\frac{3\left[(n_0^{\omega\ll\omega_0})^2-1\right]^2}{32N\hbar\pi^2}\frac{\omega_0^{11}}{(\omega_0^2-\omega_{\mathrm{THz}}^2-2i\gamma\omega)^2}\right. \\
&\left.\times\frac{1}{4\omega_{\mathrm{Opt}}^6(\omega_0^2-\omega_{\mathrm{THz}}^2-2i\gamma\omega_{\mathrm{THz}})}\right].
\end{aligned} \tag{4.22}$$

In Fig. 4.4, the absolute value of the third-order susceptibilities obtained from Eqs. (4.21) and (4.22) are plotted on a semi-log scale. The damping frequency is set equal to $\gamma = \frac{1}{2}\Gamma = 5\times 10^{12}\,\mathrm{rad/s}$.

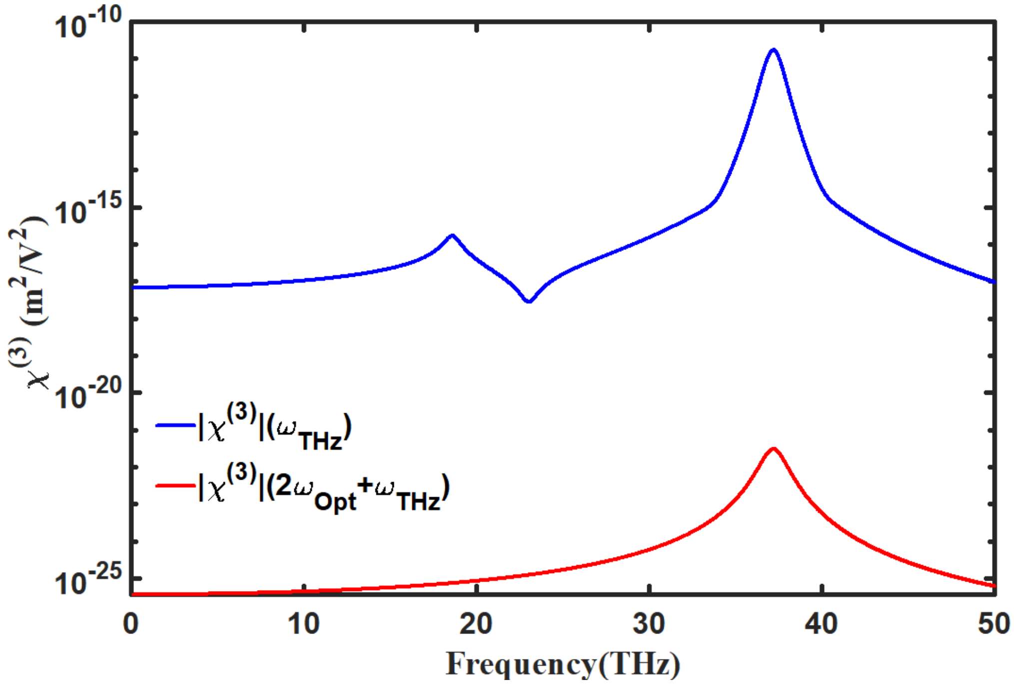

Figure 4.4: Third-order susceptibility corresponding to the self-action effects (blue) and the third-order susceptibility corresponding to the TFISH (red). For TFISH, the value at low frequency is scaled down by a factor proportional to $\omega_0^8/\omega_{\mathrm{Opt}}^8$. However, at the resonance, it is scaled down by a factor proportional to the product of the factors $\omega_0^6/\omega_{\mathrm{Opt}}^6$ and $1/\mathrm{Q}^3$, where Q is the resonance quality factor.

As can be seen from the figure, the value of the TFISH susceptibility at low frequencies is related to the susceptibility corresponding to self-action effects with a factor proportional to $\omega_0^8/\omega_{\mathrm{Opt}}^8$. The reason is that the dominant term at low frequencies is the term related to the cascaded process (first term) in both THz self-action process and TFISH. For TFISH, four resonance factors disappear compared to the expression describing THz self-action in Eq. (4.21), thus, the factor of $(1/\omega_0^2)^4$ is replaced by a factor of $(1/\omega_{\mathrm{Opt}}^2)^4$.

However, the dominant term for both THz self-action and TFISH at resonance frequency is the direct term corresponding to b. For TFISH, three resonance factors disappear compared to THz self-action, thus, the factor of $(1/\omega_0^2)^3$ is replaced by a factor of $(1/\omega_{\mathrm{Opt}}^2)^3$. However, there is another factor of $(1/\mathrm{Q})^3$, where Q is the resonance quality factor calculated as $\mathrm{Q} = \omega_0/\Gamma$, due to missing three enhancement factors at resonance frequency. As expected, the resonance related to the two-photon absorption in THz self-action spectrum at around 18 THz is not replicated in TFISH spectrum and the dominant resonance at 37.2 THz is much broader compared to the THz self-action.

In Fig. 4.5, we plotted the absolute value, real and imaginary parts of the nonlinear susceptibilities obtained from Eqs. (4.21) and (4.22) for the THz self-action and TFISH, respectively.

As the final step, we included the lower-strength lower-frequency resonances in our model. Similar to the approach presented in Chapter 2, we obtain a linear sum of the three individual resonances, assuming that there is no cross-talk between them. Thus, Eqs. (4.21) and (4.22) become modified to include the two additional resonances as follows:

$$
\begin{aligned}
\chi^{(3)}(\omega_{\mathrm{THz}}, \omega_{\mathrm{THz}}, -\omega_{\mathrm{THz}}, \omega_{\mathrm{THz}}) &= \sum_{k=1}^{3} \chi_k^{(3)}(\omega_{\mathrm{THz}}, \omega_{\mathrm{THz}}, -\omega_{\mathrm{THz}}, \omega_{\mathrm{THz}}) \\
&= \sum_{k=1}^{3} \left[\frac{qN\alpha^3}{3} \times 2a_k^2 \frac{(3\omega_{0,k}^2 - 8\omega_{\mathrm{THz}}^2 - 8i\gamma_k\omega_{\mathrm{THz}})}{\omega_{0,k}^2(\omega_{0,k}^2 - 4\omega_{\mathrm{THz}}^2 - 4i\gamma_k\omega_{\mathrm{THz}})} \right. \\
&\left. - \frac{3\left[(n_{0,k}^{\omega\ll\omega_{0,k}})^2 - 1\right]^2}{32N\hbar\pi^2} \frac{\omega_{0,k}^{11}}{(\omega_{0,k}^2 - \omega_{\mathrm{THz}}^2 - 2i\gamma_k\omega_{\mathrm{THz}})^2} \right];
\end{aligned}
\tag{4.23}
$$

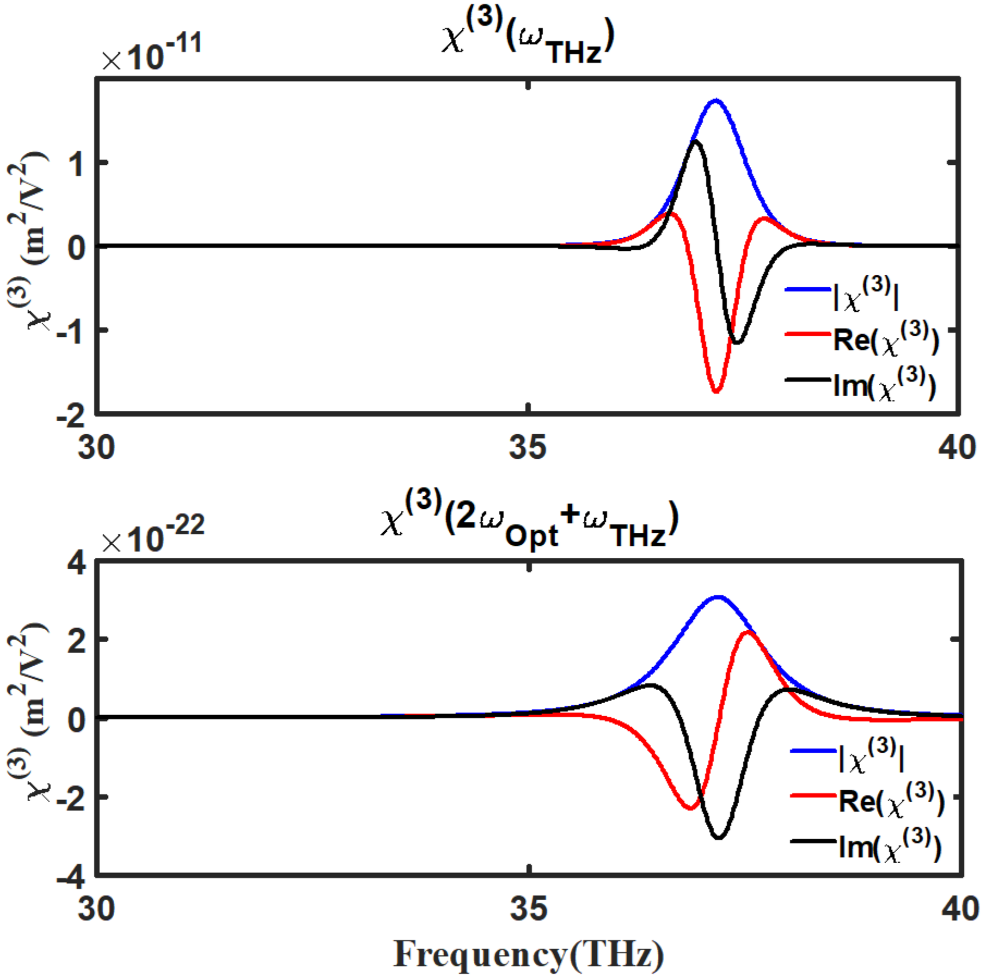

Figure 4.5: The absolute value, real and imaginary parts of the nonlinear susceptibility describing the THz self-action (top) and TFISH (bottom)

$$
\begin{aligned}
\chi^{(3)}(2\omega_{\mathrm{Opt}}+\omega_{\mathrm{THz}}) &= \sum_{k=1}^{3}\chi_k^{(3)}(2\omega_{\mathrm{Opt}}+\omega_{\mathrm{THz}}) = \\
&\sum_{k=1}^{3}\Bigg[\frac{qN\alpha^3}{3}\frac{2a_k^2}{(\omega_{0,k}^2-\omega_{\mathrm{THz}}^2-2i\gamma_k\omega_{\mathrm{THz}})}\frac{9}{16\omega_{\mathrm{Opt}}^8} \\
&+\frac{3\big[(n_{0,k}^{\omega\ll\omega_{0,k}})^2-1\big]^2}{32N\hbar\pi^2}\frac{\omega_{0,k}^{11}}{(\omega_{0,k}^2-\omega_{\mathrm{THz}}^2-2i\gamma_k\omega_{\mathrm{THz}})^2} \\
&\times\frac{1\quad 71}{4\omega_{\mathrm{Opt}}^6(\omega_{0,k}^2-\omega_{\mathrm{THz}}^2-2i\gamma_k\omega_{\mathrm{THz}})}\Bigg].
\end{aligned}
\tag{4.24}
$$

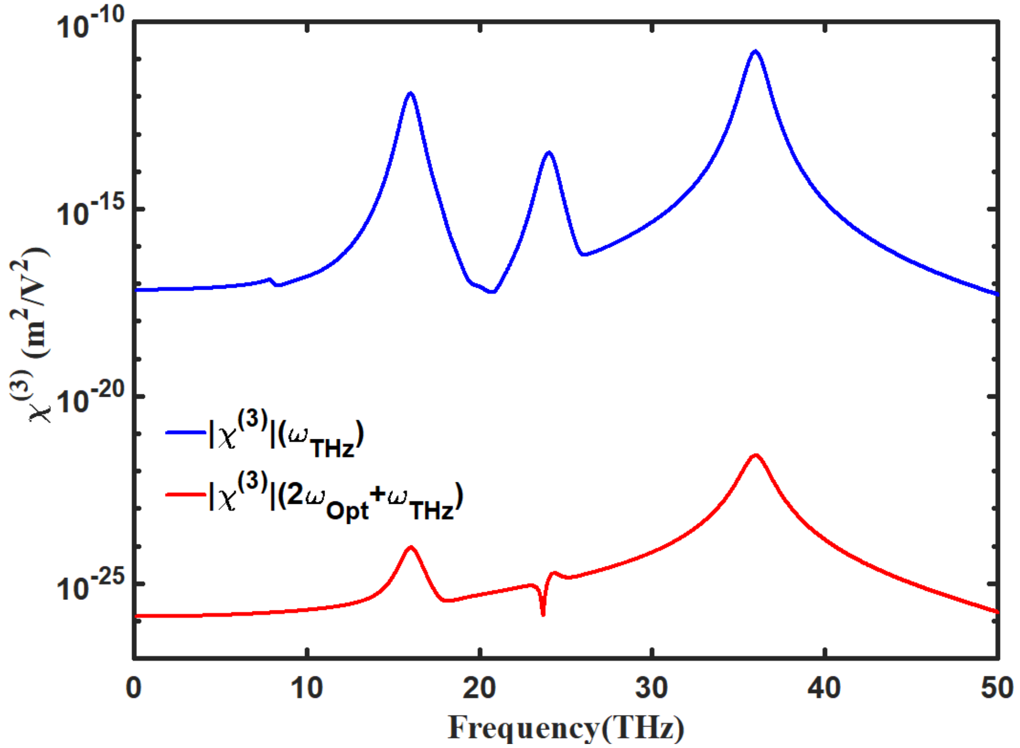

Figure 4.6: The plot of the third-order susceptibilities corresponding to the self-action effects (blue) and TFISH (red) with three resonances included. As expected from comparing Eqs. (4.23) and (4.24), each resonance in TFISH is related to the corresponding resonance in the self-action effects by a factor proportional to the product of the factors $\omega_{0,\mathrm{i}}^6/\omega_{\mathrm{Opt}}^6$ and $1/\mathrm{Q}_\mathrm{i}^3$, where $\omega_{0,i}$ and Q_i denote the resonance frequency and quality factor of the i-th resonance, respectively. In the TFISH spectrum, the resonance at 24 THz is the sum of the contributions from the resonances at 37.2 THz and 24 THz.

In Fig. 4.6, the absolute value of the third-order susceptibilities obtained from Eqs. (4.23) and (4.24) are plotted on a semi-log scale. We can see in Fig. 4.6, the susceptibility of the TFISH spectrum at its dominant resonance at 37.2 THz is equal to $3 \times 10^{-22}\ \mathrm{m}^2/\mathrm{V}^2$ which is close to the the TFISH experimental value $5.5 \times 10^{-22}\mathrm{m}^2/\mathrm{V}^2$, presented in the manuscript [74]. With the inclusion of multiple resonances, deriving a straightforward relationship similar to $\omega_0^8/\omega_{\mathrm{Opt}}^8$ becomes even more complicated, as

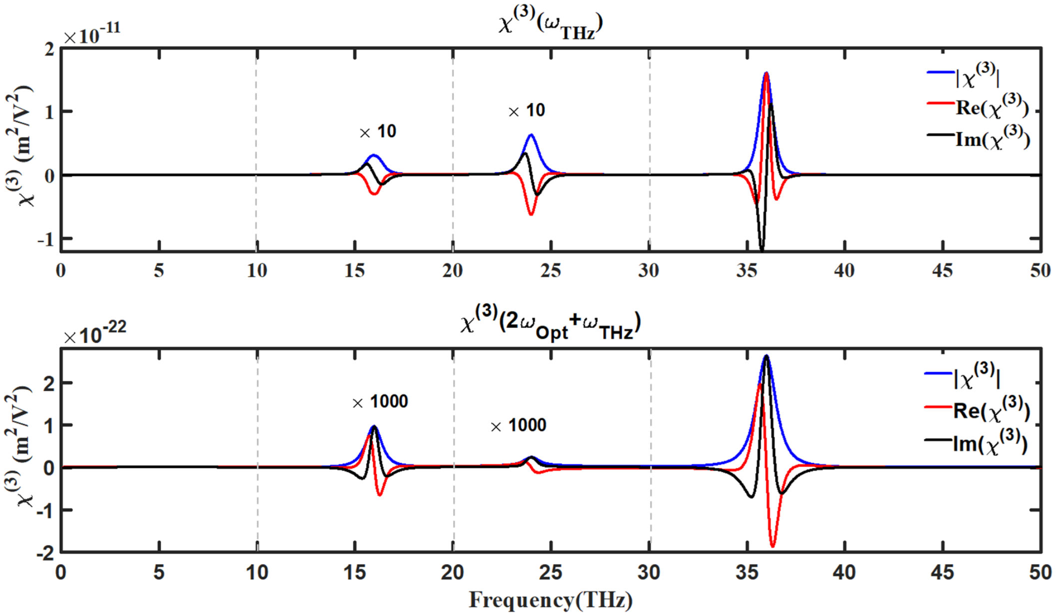

Figure 4.7: The absolute value, real and imaginary parts of the nonlinear susceptibility of the THz self-action (top) and TFISH (bottom) with the inclusion of three resonances

the total susceptibility at frequency $\omega_{\rm THz}$ is the sum of the contributions from each resonance. One should notice that each resonance in TFISH is related to the corresponding resonance in the self-action effects by a factor proportional to the product of the factors $\omega_{0,\rm i}^6/\omega_{\rm Opt}^6$ and $1/Q_i^3$, where $\omega_{0,i}$ and Q_i are the resonance frequency and quality factor of the same resonance, respectively. In Fig. 4.7, the absolute value, real and imaginary parts of the nonlinear susceptibilities of the THz self-action and TFISH described by Eqs. (4.23) and (4.24) are plotted.

4.3 THz-induced Kerr Nonlinearity

For the case of the THz induced Kerr nonlinearity, many of the steps and calculations are similar to the calculations performed in the previous part. (The in-detail calculations are included in the Appendix of this thesis.) However, the frequency of interest in the calculations is ω_{Opt} instead of $2\omega_{\mathrm{Opt}} + \omega_{\mathrm{THz}}$. Thus, the third-order correction term for the THz Kerr effect is given by

$$\begin{aligned} x^{(3)}(\omega_{\mathrm{Opt}}) = \Bigg[& \frac{4a^2\alpha^3}{(\omega_0^2 - \omega_{\mathrm{THz}}^2 - 2i\gamma\omega_{\mathrm{THz}})(\omega_0^2 - \omega_{\mathrm{THz}}^2 + 2i\gamma\omega_{THz})\omega_0^2} \\ & \times \frac{(2\omega_0^2 - \omega_{\mathrm{Opt}}^2 - 2i\gamma\omega_{\mathrm{Opt}})}{(\omega_0^2 - \omega_{\mathrm{Opt}}^2 - 2i\gamma\omega_{\mathrm{Opt}})^3} \\ & + \frac{3b\alpha^3}{(\omega_0^2 - \omega_{\mathrm{THz}}^2 - 2i\gamma\omega_{\mathrm{THz}})(\omega_0^2 - \omega_{\mathrm{THz}}^2 + 2i\gamma\omega_{\mathrm{THz}})} \\ & \times \frac{1}{(\omega_0^2 - \omega_{\mathrm{Opt}}^2 - 2i\gamma\omega_{\mathrm{Opt}})^2} \Bigg] |E_{\mathrm{THz}}|^2 E_{\mathrm{Opt}}. \end{aligned} \tag{4.25}$$

Consequently, the nonlinear susceptibility corresponding to the THz-field-induced Kerr effect is given by

$$\begin{aligned} & \chi^{(3)}(\omega_{\mathrm{Opt}}, \omega_{\mathrm{Opt}}, -\omega_{\mathrm{THz}}, \omega_{\mathrm{THz}}) = \\ & \Bigg[\frac{qN}{3} \frac{4a^2\alpha^3}{(\omega_0^2 - \omega_{\mathrm{THz}}^2 - 2i\gamma\omega_{\mathrm{THz}})(\omega_0^2 - \omega_{\mathrm{THz}}^2 + 2i\gamma\omega_{\mathrm{THz}})\omega_0^2} \\ & \times \frac{(2\omega_0^2 - \omega_{\mathrm{Opt}}^2 - 2i\gamma\omega_{\mathrm{Opt}})}{(\omega_0^2 - \omega_{\mathrm{Opt}}^2 - 2i\gamma\omega_{\mathrm{Opt}})^3} \\ & + \frac{qN}{3} \frac{3b\alpha^3}{(\omega_0^2 - \omega_{\mathrm{THz}}^2 - 2i\gamma\omega_{\mathrm{THz}})(\omega_0^2 - \omega_{\mathrm{THz}}^2 + 2i\gamma\omega_{\mathrm{THz}})(\omega_0^2 - \omega_{\mathrm{Opt}}^2 - 2i\gamma\omega_{\mathrm{Opt}})^2} \Bigg] = \\ & \Bigg[\frac{qN}{3} \frac{4a^2\alpha^3}{(\omega_0^2 - \omega_{\mathrm{THz}}^2 - 2i\gamma\omega_{\mathrm{THz}})(\omega_0^2 - \omega_{\mathrm{THz}}^2 + 2i\gamma\omega_{\mathrm{THz}})\omega_0^2} \frac{1}{\omega_{\mathrm{Opt}}^4} \\ & - \frac{3\big[(n_0^{\omega \ll \omega_0})^2 - 1\big]^2}{32N\hbar\pi^2} \frac{\omega_0^{11}}{(\omega_0^2 - \omega_{THz}^2 - 2i\gamma\omega_{\mathrm{THz}})^3} \\ & \times \frac{1}{\omega_{\mathrm{Opt}}^4(\omega_0^2 - \omega_{\mathrm{THz}}^2 + 2i\gamma\omega_{\mathrm{THz}})} \Bigg]. \end{aligned} \tag{4.26}$$

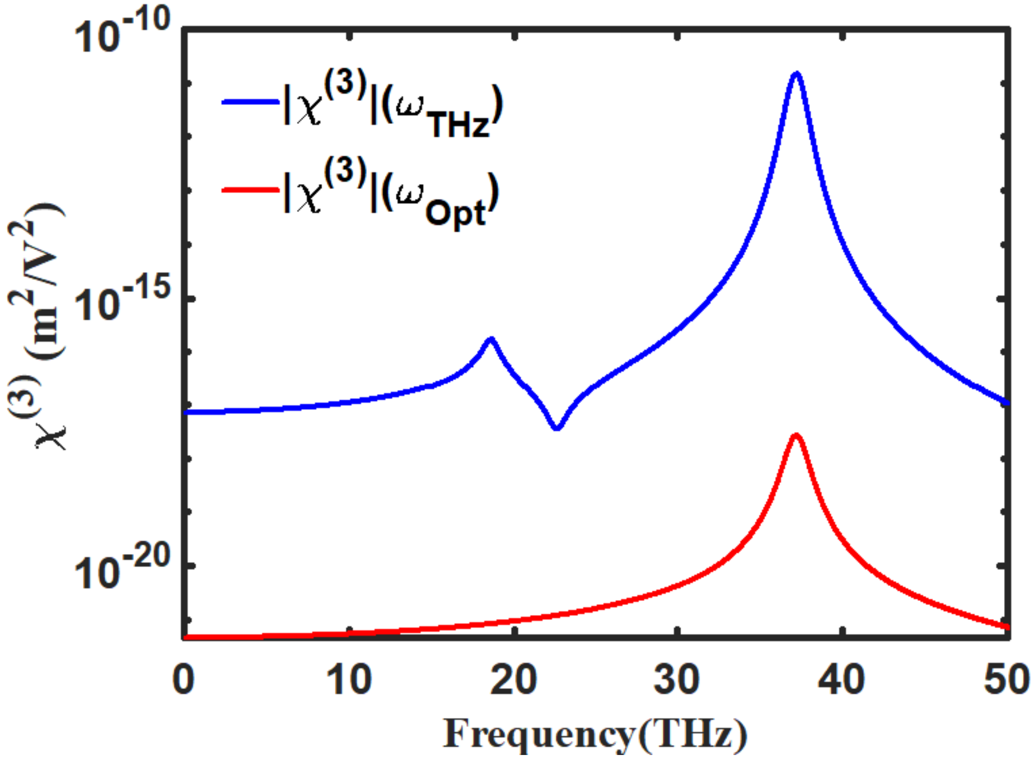

Figure 4.8: Third-order susceptibility corresponding to self-action effects (blue) and THz-induced Kerr effect (red)

Fig. 4.8 shows the absolute value of the third-order susceptibilities for the THz nonlinear refractive index and THz-induced Kerr effect at the optical range on a semi-log scale. Fig. 4.9 maps the susceptibility values provided in Table 1.2 to their corresponding probe frequencies. It clearly shows the three distinctive ranges of numbers for these effects. Among the plotted data, silicon is an interesting case to examine. Using the first terms in Eqs. (4.21) and (4.22), and removing the similar coefficients, the susceptibilities are given as

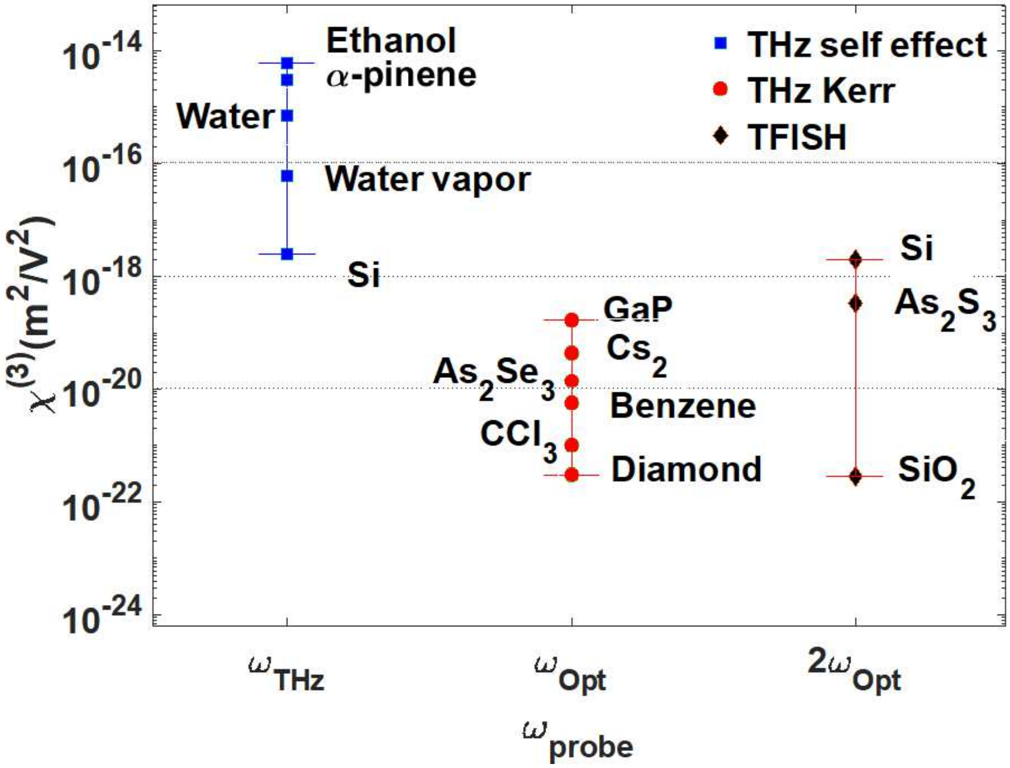

Figure 4.9: Reported susceptibility values for different THz-induced nonlinear effects. The values for the THz self-effect (blue) is well separated from the values for the THz-induced Kerr effect (red) and TFISH (black) by several orders of magnitude.

$$\begin{aligned}\chi^{(3)}(\omega_{\mathrm{THz}},\omega_{\mathrm{THz}},-\omega_{\mathrm{THz}},\omega_{\mathrm{THz}}) &= \frac{K}{(\omega_0^2-\omega_{\mathrm{THz}}^2-2i\gamma\omega_{\mathrm{THz}})^3(\omega_0^2-\omega_{\mathrm{THz}}^2+2i\gamma\omega_{\mathrm{THz}})}\\ &\times\frac{(3\omega_0^2-8\omega_{\mathrm{THz}}^2-8i\gamma\omega_{\mathrm{THz}})}{\omega_0^2(\omega_0^2-4\omega_{\mathrm{THz}}^2-4i\gamma\omega_{\mathrm{THz}})},\end{aligned}\tag{4.27}$$

$$\begin{aligned}\chi^{(3)}(2\omega_{\mathrm{Opt}}+\omega_{\mathrm{THz}}) &= \frac{K}{(\omega_0^2-\omega_{\mathrm{THz}}^2-2i\gamma\omega_{\mathrm{THz}})(\omega_0^2-\omega_{\mathrm{Opt}}^2-2i\gamma\omega_{\mathrm{Opt}})^3}\\ &\times\frac{(3\omega_0^2-9\omega_{\mathrm{Opt}}^2-10i\gamma\omega_{\mathrm{Opt}})}{(\omega_0^2-4\omega_{\mathrm{Opt}}^2-4i\gamma\omega_{\mathrm{Opt}})^2}.\end{aligned}\tag{4.28}$$

In order to find the ratio between Eqs. (4.27) and (4.28), we need to evaluate the expressions under the following assumptions: $\omega_{\text{Opt}} = 375$ THz, $\omega_{\text{THz}} \approx 1$ THz. Silicon has a single dominant resonance at $\lambda_0 = 300$ nm [93]. Thus, $\omega_0 = \frac{8}{3}\omega_{\text{Opt}}$. It is now possible to simplify and evaluate the expressions in Eqs. (4.27) and (4.28):

$$\chi^{(3)}(\omega_{\text{THz}}, \omega_{\text{THz}}, -\omega_{\text{THz}}, \omega_{\text{THz}}) = \frac{3K}{\omega_0^{10}}, \tag{4.29}$$

$$\chi^{(3)}(2\omega_{\text{Opt}} + \omega_{\text{THz}}) = \frac{2.11K}{\omega_0^8 \omega_{\text{Opt}}^2} = \frac{15K}{\omega_0^{10}}. \tag{4.30}$$

Thus, the ratio of the susceptibilities are calculated as

$$\frac{\chi^{(3)}(\omega_{\text{THz}}, \omega_{\text{THz}}, -\omega_{\text{THz}}, \omega_{\text{THz}})}{\chi^{(3)}(2\omega_{\text{Opt}} + \omega_{\text{THz}})} = 0.2. \tag{4.31}$$

It can be concluded from Fig. 4.9 that this ratio for Si is equal to 0.6.

4.4 Conclusions

In this chapter, we categorized the reported THz-induced third-order effects into three main groups based on the frequency of the probe beam. The THz-induced nonlinear refractive index n_2 at the THz frequencies, represented by $\chi^{(3)}(\omega_{\text{THz}}, \omega_{\text{THz}}, \omega_{\text{THz}}, -\omega_{\text{THz}})$, TFISH generation expressed as $\chi^{(3)}(2\omega_{\text{Opt}} + \omega_{\text{THz}}, \omega_{\text{Opt}}, \omega_{\text{Opt}}, \omega_{\text{THz}})$, and, finally, THz-induced Kerr effect in the optical frequencies described by $\chi^{(3)}(\omega_{\text{Opt}}, \omega_{\text{THz}}, -\omega_{\text{THz}}, \omega_{\text{Opt}})$, have probe beams at the frequencies ω_{Opt}, $2\omega_{\text{Opt}}$ and ω_{THz}, respectively. Then, we derived expressions that relate the third-order susceptibilities corresponding to TFISH and THz-induced Kerr effect to the nonlinear susceptibility corresponding THz self-effects. We concluded that, despite the fact that all three effects are caused by the contribution from the vibrational modes, it is the frequency of the probe beam that determines the order of the corresponding third-order susceptibility. After deriving the expression for each effect, we showed that the values of the susceptibility for TFISH and THz-Kerr effects are related to the the values of the susceptibility for THz self-action by a factor dependent on the resonance frequency and the frequency of the probe beam. Furthermore, we calculated the TFISH susceptibility of $\mathrm{SiO_2}$ at its resonance frequency, which agrees with the reported experimental value in Ref. [74]. This work establishes the relationship between different third-order THz-induced nonlinear effects and is of great importance for the consistency of the reported values.

Chapter 5

CONCLUSION

5.1 Conclusions

In this doctoral thesis, first we explored the literature on the nonlinear behaviour of different materials at THz frequencies. In the process, three main questions arose: How large is the nonlinearity of the solids at THz frequencies? Are the current approximations able to extract the nonlinear refractive index dispersion from THz nonlinear TDS data? Finally, what is the relation between the THz-induced effects at THz frequencies and optical frequencies? In this work, we study and explore nonlinear THz spectroscopy of solid samples from different aspects and try to answer the above questions.

First, we modified a previously established theoretical model for the nonlinear refractive index of crystalline quartz at the THz frequencies by including additional vibrational resonances. This model predicted a nonlinear refractive index several orders of magnitude larger than the typical values at the optical frequencies [62]. The inclusion of the additional resonances allowed a better agreement between the theoretical prediction and the experimental measurements. Then, through the THz nonlinear time-domain spectroscopy, we measured the nonlinear refractive index of quartz at the THz frequencies, which had a good agreement with our theoretical model.

Furthermore, we presented a simple method to model the propagation of a broadband

THz pulse in a nonlinear medium with a nonlinear refractive index dispersion using a spectral solution to the wave equation based on Fourier analysis. This method is a useful tool to investigate the effects of the nonlinear dispersion on the propagation of ultrashort THz pulses in a straightforward fashion. Furthermore, based on the same model, we derive an expression to extract the nonlinear refractive index dispersion for broadband sources and compare it with the approximate methods previously proposed: monochromatic approximation and sharp-resonance approximation. We perform a simulation on a sample with linear absorption and an arbitrary dispersion for nonlinear refractive index, and successfully extract the dispersion from the simulated propagation output. Through this, we are able to factor out the effect of the spectral shape of the broadband THz pulse.

Finally, we derived a relationship between the nonlinear susceptibility corresponding to the THz self-action and THz field-induced second harmonic (TFISH) generation and THz-induced Kerr effect. As a result, we are able to explain the scaling factor between the values reported for the susceptibilities corresponding these effect in the experimental works. We concluded that although all three effects are caused by the vibrational modes, it is the frequency at which the effect is sensed that determines the magnitude of the susceptibility. In other words, the frequency of the probe beam is the distinctive factor in these three effects.

5.2 Future Outlook

5.2.1 THz Nonlinear Spectroscopy of Semiconductors

At the THz frequencies, semiconductors have a similar optical behavior to the behavior of metals in the visible/NIR range [94]. Their complex permittivity is modelled by Drude-Lorentz model as

$$\varepsilon_r(\omega) = \varepsilon_\infty - \frac{\omega_p^2}{\omega^2 + i\gamma_p\omega} + \frac{A_L\omega_L}{\omega_L^2 - \omega^2 - i\gamma_L\omega}, \tag{5.1}$$

where ε_∞ is the background permittivity, caused by high-frequency resonances (electronic interband resonances), while the second term is the Drude term, where ω_p is the plasma frequency and γ_p is the damping constant. Drude model describes the resistivity of the conducting material with the scattering of the carriers inside the material and models the metallic behavior of the semiconductor. The last term is the Lorentz term describing the contribution of the vibrational modes to the permittivity of the semiconductor and is similar to the Lorentz model we used in Chapter 2 and Chapter 4, where ω_L is the resonance frequency, γ_L is the damping frequency, and A_L is the oscillator's amplitude. The plasma frequency of the semiconductors falls in the range of $9 - 75$ THz. However, due to the significant background permittivity ($\sim 10 - 16$), the frequency at which the sign of the permittivity changes is lower than the plasma frequency ω_p and is called the reduced plasma frequency, calculated as

$$\omega_p^{\text{reduced}} = \frac{\omega_p}{\sqrt{\varepsilon_\infty}}. \tag{5.2}$$

For the un-doped InSb, the background permittivity is $\varepsilon_\infty \approx 15$ and $\omega_p \approx 2\pi \times 9$ THz. This implies that the sign of InSb permittivity changes at the reduced plasma frequency

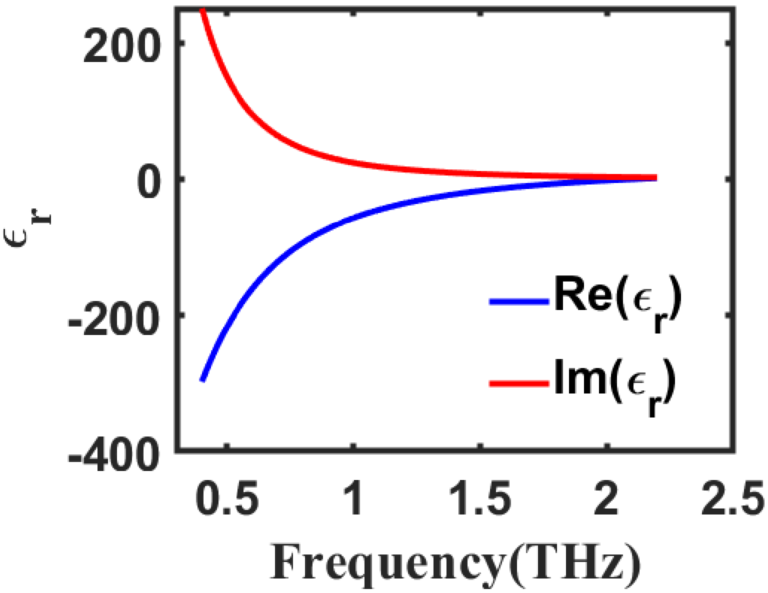

Figure 5.1: The complex permittivity function of InSb. The blue curve shows the real part of the permittivity, while the red curve represents its imaginary part.

$\omega_p^{\text{reduced}} \approx 2\pi \times 2.2$ THz, which is a frequency range accessible by the available THz sources. Fig. 5.1 shows the real and imaginary parts of permittivity of the un-doped InSb [94].

Metals at low THz frequencies are highly conductive with a negative permittivity of large magnitude. The Drude-like behavior of the un-doped InSb at low THz frequencies makes it a suitable candidate to replace the metals in the plasmonic devices [95]. Several studies have been carried out on the linear characterization of different semiconductors using THz-TDS in reflective configurations [94, 96]. Furthermore, nonlinear effects such as THz-induced impact ionisation and inter-valley scattering in semiconductors have been previously reported [26, 40, 41, 42, 43]. However, to the best of our knowledge, the nonlinear optical properties of the semiconductors in the THz frequency range, such as the third-order nonlinear effects discussed in this thesis, have not been reported. One would expect a Drude-like semiconductor such as InSb to show a strong nonlinear response near its plasmonic frequency range. Thus, nonlinear characterization of semiconductor thin-films at the THz frequencies in the transmission configuration would be a major contribution to the field of nonlinear THz optics and THz nonlinear devices.

5.2.2 Effective Medium Theory and Composite Materials at the THz Frequencies

The growing list of applications for the photonic technologies comes with the need for new optical materials with specific properties. They are used for improving the lasers gain, engineering the nonlinear response of materials, and tailoring the material dispersion for phase matching, to name a few [97]. Optical metamaterials are artificially engineered structures made of metals and dielectrics that are designed to show the electromagnetic properties that are not available in nature but are not forbidden by Maxwell's equations like negative refractive index [98]. A special group of metamaterials is composite materials that are hybrid optical materials achieved by intermixing two or more homogeneous constituent materials in scales much smaller than the optical wavelength, so that on a macroscopic level, the electromagnetic wave sees the structure as a homogeneous material. Therefore, like all other homogeneous optical materials, the structure can be described by two electromagnetic parameters: ε and μ. The relation between the resultant parameters and the constituent materials is described through the effective medium theory.

Many different models have been developed for different structure geometries: Maxwell Garnett, Bruggeman and layered structures, as shown in Fig. 5.2 [99, 100]. As shown

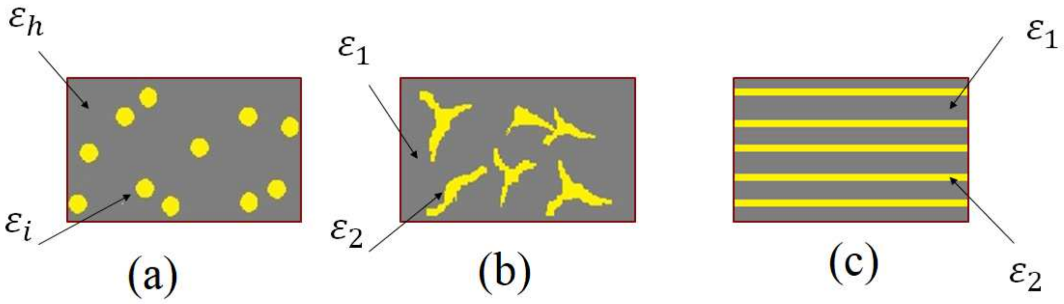

Figure 5.2: Composite material geometries. (a) Maxwell-Garnett structure: very small spheres of inclusion material are embedded inside a host material. (b) Bruggeman structure: Two constituent materials are embedded in each other to form an effective medium. (c) Layered structure: sets of alternating thin layers.

in the figure, there are three main composite geometries. The first structure is Maxwell Garnet, where very small spherical or oval-shaped particles of inclusion material are embedded in a host material. Bruggeman is the second structure, where two different materials are embedded in an effective medium. Finally, the third one is layered structure where planar layers of materials are stacked alternatingly over each other. Of the three groups mentioned, the latter one is of particular interest for its fabrication simplicity.

In a layered composite structure, the effective permittivity is the weighted average of the two constituent materials and is calculated as

$$\varepsilon_{\text{eff}} = (1 - f)\varepsilon_1 + f\varepsilon_2. \tag{5.3}$$

The validity of effective medium theory in this structure could be verified by the transfer matrix formalism [38, 101]. Consider three layers of different thicknesses and complex refractive indices, as depicted in Fig. 5.3. At each intersection, we have the

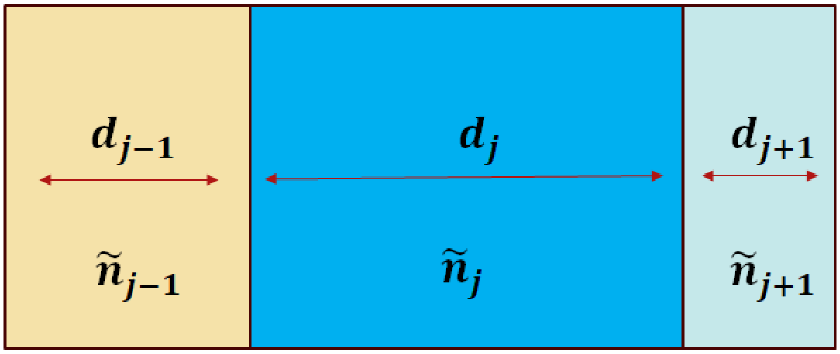

Figure 5.3: A schematic of three stacked layers. Each layer is described by its thickness and its complex refractive index.

continuity of the tangential electric and magnetic fields as follows:

$$E_j^{||} = E_{j+1}^{||} \tag{5.4}$$

$$H_j^{||} = H_{j+1}^{||}, \tag{5.5}$$

where E_{j-1}, $E_j^{||}$, H_{j-1} and $H_j^{||}$ are the tangential electric and magnetic fields at the j-th interface. One should note that the fields are the sums of the tangential fields of the forward and backward travelling waves. Thus, the relationship between the incident and reflected fields are given by

$$E_j^i e^{-ik_j d_j} + E_j^r = E_{j+1}^i + E_{j+1}^r e^{-ik_{j+1} d_{j+1}}, \tag{5.6}$$

$$H_j^i e^{-ik_j d_j} - H_j^r = H_{j+1}^i - H_{j+1}^r e^{-ik_{j+1} d_{j+1}}, \tag{5.7}$$

where $k_j = \tilde{n}_j k_0$ is the complex propagation constant for the j-th layer, and d_j is the thickness of the j-th layer. Since we assume that the materials are nonmagnetic, we are more interested to find the relation for the electric fields. The relation between the magnetic field and electric field for a propagating wave is given as

$$H_j = \frac{E_j}{\eta_j}, \tag{5.8}$$

where $\eta_j = \sqrt{\frac{\mu}{\varepsilon}} = \frac{120\pi}{\sqrt{\varepsilon_r}}$ is the wave impedance in the j-th layer. Substituting Eq. (5.8) in Eqs. (5.6) and (5.7), we obtain the relation between the incident wave coming from the previous interface and the reflected and transmitted waves at the current interface:

$$E_j^i e^{-ik_j d_j} + E_j^r = E_{j+1}^i + E_{j+1}^r e^{-ik_{j+1} d_{j+1}}; \tag{5.9}$$

$$\frac{E_j^i}{\eta_j} e^{-ik_j d_j} - \frac{E_j^r}{\eta_j} = \frac{E_{j+1}^i}{\eta_{j+1}}^{i} - \frac{E_{j+1}^r}{\eta_{j+1}} e^{-ik_{j+1} d_{j+1}}. \tag{5.10}$$

These relations can be written in matrix form as

$$\begin{bmatrix} E_j^i \\ E_j^r \end{bmatrix} = M_j \begin{bmatrix} E_{j+1}^i \\ E_{j+1}^r \end{bmatrix}. \tag{5.11}$$

Finally, the transfer matrices at each layer should be multiplied to obtain the total cascaded transfer matrix. The relation between the incident, reflected and transmitted fields in an $N + 1$ layer structure is given by

$$\begin{bmatrix} E_1^i \\ E_1^r \end{bmatrix} = M_{\text{tot}} \begin{bmatrix} E_{N+1}^i \\ 0 \end{bmatrix} = \prod_{j=1}^{N} M_j \begin{bmatrix} E_{N+1}^i \\ 0 \end{bmatrix}. \tag{5.12}$$

Now that the transfer matrix method is established, we can use it to simulate a multilayer structure and compare the results with an effective medium bulk structure, as depicted in Fig. 5.4.

The reflectivity and transmittivity spectra for a structure of 24 bi-layers of InSb and Al_2O_3 with the periodicity of 5 microns and filling factor of InSb $f = 0.1$ are depicted in Fig. 5.5 and compared with the responses from the equivalent effective bulk medium. We observe a very close agreement between the two sets of responses. We can see that the transmittivity (red) spectra obtained from the transfer matrix method and the effective medium theory completely overlap. The reflectivity spectral response calculated

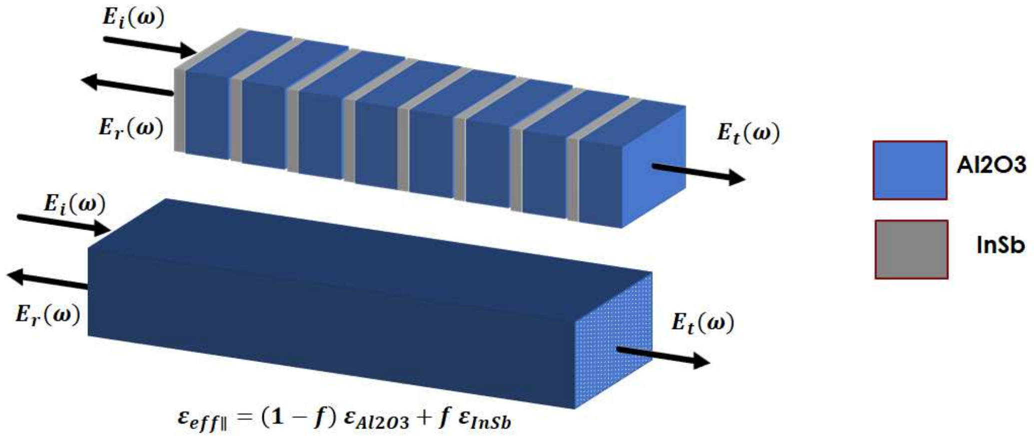

Figure 5.4: A multi-layer structure of InSb and $\mathrm{Al_2O_3}$ bi-layers and the bulk effective medium.

from the matrix formalism (blue dashed-line) follows the response obtained from effective medium theory very closely. The minor discrepancy is rooted in the fact that the multi-layer structure modeled by the transfer matrix is not symmetrical. Consequently, the scattering matrix is not symmetric anymore, meaning that it is important that the field is applied from which side. For an exact overlap, one could calculate the reflectivity responses from both ends of the structure, $\mathrm{R_1}$ and $\mathrm{R_2}$, and then express the reflectivity as the geometric average of these responses calculated as $\mathrm{R} = \sqrt{\mathrm{R_1 R_2}}$ [102].

Linear characterization of the composite materials including semiconductor layers would be a major contribution to the field of THz-TDS. Moreover, the effective medium theory enables the engineering of the optical properties of the materials in THz frequencies by changing the fill factor. Developing THz composite materials with optical properties exceeding those of the constituents can enable new applications.

Given that the effective medium theory extends to the nonlinear susceptibility [103]

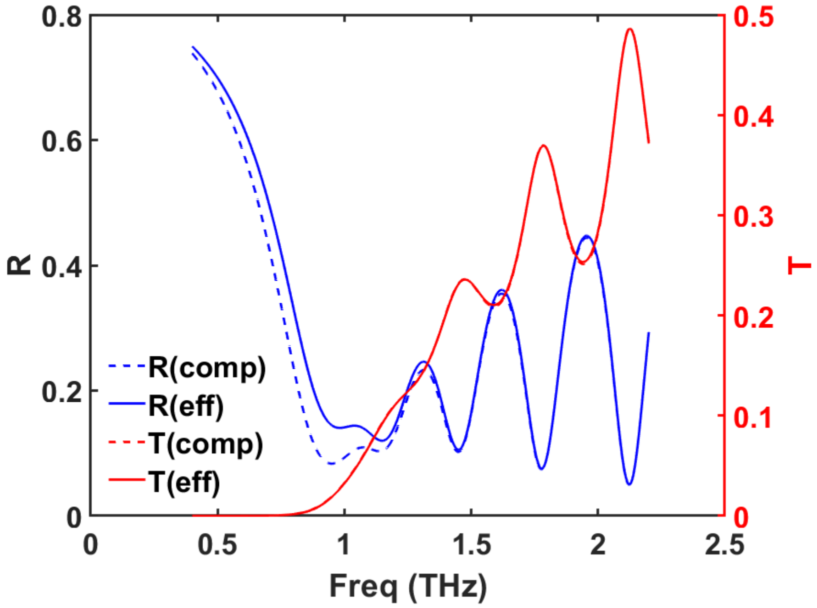

Figure 5.5: Reflectivity and transmittivity spectra of a structure with 24 bi-layers of InSb and $\mathrm{Al_2O_3}$, with the periodicity of 5 microns and InSb filling factor of $f = 0.1$.

and the large nonlinearity of Drude-like materials around their plasmonic frequency range, one expects that the effective third-order susceptibility of a layered structure with fill-factor of f for a semiconductor like InSb can be estimated as $\chi^{(3)}_{\mathrm{comp}} \approx f\chi^{(3)}_{\mathrm{InSb}}$. However, compared to the equivalent bulk InSb, the composite material has a larger transmission. Fig. 5.6 compares the transmission of a structure of 24 bi-layers of InSb and $\mathrm{Al_2O_3}$, with the periodicity of 5 microns and InSb filling factor of $f = 0.1$ and a single InSb slab with the thickness equal to the total amount of InSb in the composite $d_{\mathrm{InSb}} = 0.1 \times 120 = 12\ \mu\mathrm{m}$. We can see that the amount of the transmitted power of the composite material at 1.5 THz is 10 times larger than that exhibited by InSb slab. One can conclude that composite materials can enable accessing the very strong nonlinear response coming from the semiconductors while avoiding the strong absorption.

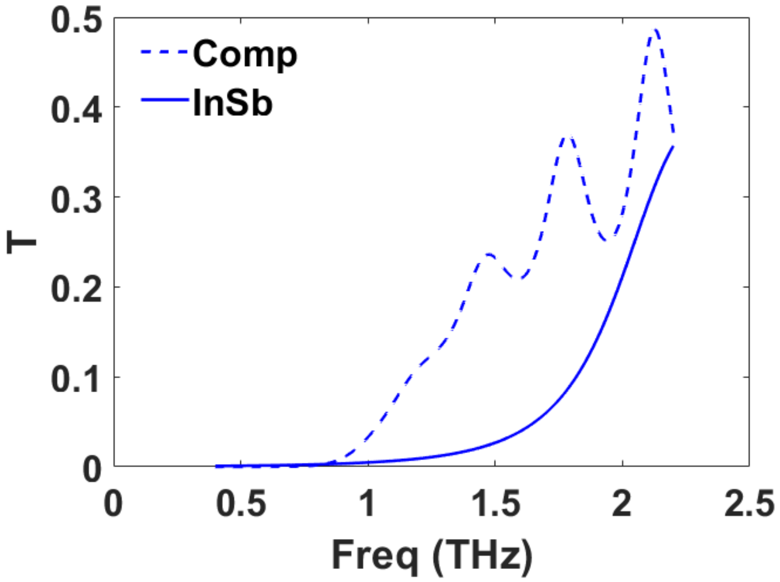

Figure 5.6: The transmission spectra of a structure with 24 bi-layers of InSb and $\mathrm{Al_2O_3}$, with the periodicity of 5 microns (dashed lines) and InSb filling factor of $f = 0.1$ and the equivalent InSb slab with the thicknes of 12 microns (solid lines).

Ref. [101] proposed a design procedure for a similar problem in a copper-silica composite within optical frequencies. A carefully designed composite material with semiconductor inclusions would benefit from a nonlinear response significantly stronger than the other solid materials and a tailored optical response in the THz frequency range.

5.2.3 Nonlinear Spectroscopy of Solids with Different Structures

As a continuation to the works performed in Chapter 2 and Chapter 3, there are other candidate materials for the exploration of the third-order nonlinear interactions at the THz frequencies. For example, exploring the nonlinear response of other crystalline solids with different crystal structures could be of interest. For example, THz-induced nonlinear birefringence in a sapphire sample is of great interest for further exploration.

Finally, one can examine the nonlinear response of chalcogenide glasses. Strong THz-induced Kerr effect has been previously reported for this group of glasses [57]. Other groups of effects, per the discussion in Chapter 4, would be interesting to explore in these materials.

REFERENCES

[1] X. Yang, X. Zhao, K. Yang, Y. Liu, Y. Liu, W. Fu, and Y. Luo, "Biomedical applications of terahertz spectroscopy and imaging," *Trends in Biotechnology*, vol. 34, p. 810–824, Oct. 2016.

[2] J. F. Federici, B. Schulkin, F. Huang, D. Gary, R. Barat, F. Oliveira, and D. Zimdars, "Thz imaging and sensing for security applications—explosives, weapons and drugs," *Semiconductor Science and Technology*, vol. 20, p. S266, jun 2005.

[3] K. S, Y. M, A. Rawson, and S. C. K, "Recent advances in terahertz time-domain spectroscopy and imaging techniques for automation in agriculture and food sector," *Food Analytical Methods*, vol. 15, p. 498–526, Oct. 2021.

[4] E. Pickwell and V. P. Wallace, "Biomedical applications of terahertz technology," *Journal of Physics D: Applied Physics*, vol. 39, p. R301, aug 2006.

[5] L. Afsah-Hejri, P. Hajeb, P. Ara, and R. J. Ehsani, "A comprehensive review on food applications of terahertz spectroscopy and imaging," *Comprehensive Reviews in Food Science and Food Safety*, vol. 18, p. 1563–1621, Aug. 2019.

[6] X.-C. Zhang and J. Xu, *Introduction to THz wave photonics*. New York: Springer, 2010. OCLC: ocn428029012.

[7] P. Jepsen, D. Cooke, and M. Koch, "Terahertz spectroscopy and imaging – modern techniques and applications," *Laser & Photonics Reviews*, vol. 5, no. 1, pp. 124–166, 2011.

[8] M. Tani, S. Matsuura, K. Sakai, and S. ichi Nakashima, "Emission characteristics of photoconductive antennas based on low-temperature-grown gaas and semi-insulating gaas," *Appl. Opt.*, vol. 36, pp. 7853–7859, Oct 1997.

[9] S. Winnerl, F. Peter, S. Nitsche, A. Dreyhaupt, B. Zimmermann, M. Wagner, H. Schneider, M. Helm, and K. Kohler, "Generation and detection of thz radiation with scalable antennas based on gaas substrates with different carrier lifetimes," *IEEE Journal of Selected Topics in Quantum Electronics*, vol. 14, no. 2, pp. 449–457, 2008.

[10] M. Stellmacher, J.-P. Schnell, D. Adam, and J. Nagle, "Photoconductivity investigation of the electron dynamics in GaAs grown at low temperature," *Applied Physics Letters*, vol. 74, pp. 1239–1241, 03 1999.

[11] M. Kress, T. Löffler, S. Eden, M. Thomson, and H. G. Roskos, “Terahertz-pulse generation by photoionization of air with laser pulses composed of both fundamental and second-harmonic waves,” *Opt. Lett.*, vol. 29, pp. 1120–1122, May 2004.

[12] X. Xie, J. Dai, and X.-C. Zhang, “Coherent control of thz wave generation in ambient air,” *Phys. Rev. Lett.*, vol. 96, p. 075005, Feb 2006.

[13] Y.-S. Lee, *Principles of terahertz science and technology*. New York, NY: Springer, 2009.

[14] E. Matsubara, M. Nagai, and M. Ashida, “Coherent infrared spectroscopy system from terahertz to near infrared using air plasma produced by 10-fs pulses,” *J. Opt. Soc. Am. B*, vol. 30, pp. 1627–1630, Jun 2013.

[15] I. Babushkin, W. Kuehn, C. Köhler, S. Skupin, L. Bergé, K. Reimann, M. Woerner, J. Herrmann, and T. Elsaesser, “Ultrafast spatiotemporal dynamics of terahertz generation by ionizing two-color femtosecond pulses in gases,” *Phys. Rev. Lett.*, vol. 105, p. 053903, Jul 2010.

[16] A. Nahata, D. H. Auston, T. F. Heinz, and C. Wu, “Coherent detection of freely propagating terahertz radiation by electro-optic sampling,” *Applied Physics Letters*, vol. 68, no. 2, pp. 150–152, 1996.

[17] J. Hebling, K.-L. Yeh, M. C. Hoffmann, B. Bartal, and K. A. Nelson, “Generation of high-power terahertz pulses by tilted-pulse-front excitation and their application possibilities,” *J. Opt. Soc. Am. B*, vol. 25, pp. B6–B19, Jul 2008.

[18] Y. J. Ding and W. Shi, “Efficient thz generation and frequency upconversion in gap crystals,” *Solid-State Electronics*, vol. 50, no. 6, pp. 1128–1136, 2006. Special Issue: ISDRS 2005.

[19] T. Tanabe, K. Suto, J. Nishizawa, K. Saito, and T. Kimura, “Tunable terahertz wave generation in the 3- to 7-THz region from GaP,” *Applied Physics Letters*, vol. 83, pp. 237–239, 07 2003.

[20] I. Katayama, R. Akai, M. Bito, E. Matsubara, and M. Ashida, “Electric field detection of phase-locked near-infrared pulses using photoconductive antenna,” *Opt. Express*, vol. 21, pp. 16248–16254, Jul 2013.

[21] Y. C. Shen, P. C. Upadhya, H. E. Beere, E. H. Linfield, A. G. Davies, I. S. Gregory, C. Baker, W. R. Tribe, and M. J. Evans, “Generation and detection of ultrabroadband terahertz radiation using photoconductive emitters and receivers,” *Applied Physics Letters*, vol. 85, pp. 164–166, 07 2004.

[22] N. Karpowicz, J. Dai, X. Lu, Y. Chen, M. Yamaguchi, H. Zhao, X.-C. Zhang, L. Zhang, C. Zhang, M. Price-Gallagher, C. Fletcher, O. Mamer, A. Lesimple, and K. Johnson, "Coherent heterodyne time-domain spectrometry covering the entire "terahertz gap"," *Applied Physics Letters*, vol. 92, p. 011131, 01 2008.

[23] Q. Wu, M. Litz, and X. Zhang, "Broadband detection capability of ZnTe electro-optic field detectors," *Applied Physics Letters*, vol. 68, pp. 2924–2926, 05 1996.

[24] Q. Wu and X.-C. Zhang, "7 terahertz broadband GaP electro-optic sensor," *Applied Physics Letters*, vol. 70, pp. 1784–1786, 04 1997.

[25] H. Hirori, A. Doi, F. Blanchard, and K. Tanaka, "Single-cycle terahertz pulses with amplitudes exceeding 1 mv/cm generated by optical rectification in linbo3," *Applied Physics Letters*, vol. 98, no. 9, p. 091106, 2011.

[26] S. Ašmontas, S. Bumelienė, J. Gradauskas, R. Raguotis, and A. Sužiedėlis, "Impact ionization and intervalley electron scattering in insb and inas induced by a single terahertz pulse," *Scientific Reports*, vol. 10, p. 10580, Jun 2020.

[27] K. Fan, H. Y. Hwang, M. Liu, A. C. Strikwerda, A. Sternbach, J. Zhang, X. Zhao, X. Zhang, K. A. Nelson, and R. D. Averitt, "Nonlinear terahertz metamaterials via field-enhanced carrier dynamics in gaas," *Phys. Rev. Lett.*, vol. 110, p. 217404, May 2013.

[28] *Terahertz Spectroscopy and Imaging*. Springer Berlin Heidelberg, 2013.

[29] Y. Lu, Y. Huang, J. Cheng, R. Ma, X. Xu, Y. Zang, Q. Wu, and J. Xu, "Nonlinear optical physics at terahertz frequency," *Nanophotonics*, 2024.

[30] H. A. Hafez, S. Kovalev, J.-C. Deinert, Z. Mics, B. Green, N. Awari, M. Chen, S. Germanskiy, U. Lehnert, J. Teichert, Z. Wang, K.-J. Tielrooij, Z. Liu, Z. Chen, A. Narita, K. Müllen, M. Bonn, M. Gensch, and D. Turchinovich, "Extremely efficient terahertz high-harmonic generation in graphene by hot dirac fermions," *Nature*, vol. 561, pp. 507–511, Sep 2018.

[31] J. Chen, Y. Chen, H. Zhao, G. J. Bastiaans, and X.-C. Zhang, "Absorption coefficients of selected explosives and related compounds in the range of 0.1–2.8 thz," *Opt. Express*, vol. 15, pp. 12060–12067, Sep 2007.

[32] Y. Peng, C. Shi, X. Wu, Y. Zhu, and S. Zhuang, "Terahertz imaging and spectroscopy in cancer diagnostics: A technical review," *BME Frontiers*, vol. 2020, p. 2547609, Sep 2020.

[33] H. Lindley-Hatcher, R. I. Stantchev, X. Chen, A. I. Hernandez-Serrano, J. Hardwicke, and E. Pickwell-MacPherson, “Real time thz imaging—opportunities and challenges for skin cancer detection,” *Applied Physics Letters*, vol. 118, no. 23, p. 230501, 2021.

[34] T. Kleine-Ostmann and T. Nagatsuma, “A review on terahertz communications research,” *Journal of Infrared, Millimeter, and Terahertz Waves*, vol. 32, pp. 143–171, Feb 2011.

[35] N. Krumbholz, T. Hochrein, N. Vieweg, T. Hasek, K. Kretschmer, M. Bastian, M. Mikulics, and M. Koch, “Monitoring polymeric compounding processes inline with thz time-domain spectroscopy,” *Polymer Testing*, vol. 28, no. 1, pp. 30–35, 2009.

[36] K. Krügener, M. Schwerdtfeger, S. F. Busch, A. Soltani, E. Castro-Camus, M. Koch, and W. Viöl, “Terahertz meets sculptural and architectural art: Evaluation and conservation of stone objects with t-ray technology,” *Scientific Reports*, vol. 5, p. 14842, Oct 2015.

[37] S. Busch, M. Weidenbach, M. Fey, F. Schäfer, T. Probst, and M. Koch, “Optical properties of 3d printable plastics in the thz regime and their application for 3d printed thz optics,” *Journal of Infrared, Millimeter, and Terahertz Waves*, vol. 35, no. 12, pp. 993–997, 2014.

[38] . Ulaby, Fawwaz T. (Fawwaz Tayssir), *Fundamentals of applied electromagnetics*. Sixth edition. Boston : Prentice Hall, [2010] ©2010, [2010]. Includes bibliographical references (pages [487]-488) and index.

[39] J. Neu and C. A. Schmuttenmaer, “Tutorial: An introduction to terahertz time domain spectroscopy (THz-TDS),” *Journal of Applied Physics*, vol. 124, p. 231101, 12 2018.

[40] M. C. Hoffmann, J. Hebling, H. Y. Hwang, K.-L. Yeh, and K. A. Nelson, “Impact ionization in insb probed by terahertz pump—terahertz probe spectroscopy,” *Phys. Rev. B*, vol. 79, p. 161201, Apr 2009.

[41] C. Lange, T. Maag, M. Hohenleutner, S. Baierl, O. Schubert, E. R. J. Edwards, D. Bougeard, G. Woltersdorf, and R. Huber, “Extremely nonperturbative nonlinearities in gaas driven by atomically strong terahertz fields in gold metamaterials,” *Phys. Rev. Lett.*, vol. 113, p. 227401, Nov 2014.

[42] A. T. Tarekegne, K. Iwaszczuk, M. Zalkovskij, A. C. Strikwerda, and P. U. Jepsen, “Impact ionization in high resistivity silicon induced by an intense terahertz field enhanced by an antenna array,” vol. 17, p. 043002, apr 2015.

[43] S. Tani, F. m. c. Blanchard, and K. Tanaka, “Ultrafast carrier dynamics in graphene under a high electric field,” *Phys. Rev. Lett.*, vol. 109, p. 166603, Oct 2012.

[44] O. Schubert, M. Hohenleutner, F. Langer, B. Urbanek, C. Lange, U. Huttner, D. Golde, T. Meier, M. Kira, S. W. Koch, and R. Huber, “Sub-cycle control of terahertz high-harmonic generation by dynamical bloch oscillations,” *Nature Photonics*, vol. 8, pp. 119–123, Feb 2014.

[45] X. Chai, X. Ropagnol, S. M. Raeis-Zadeh, M. Reid, S. Safavi-Naeini, and T. Ozaki, “Subcycle terahertz nonlinear optics,” *Phys. Rev. Lett.*, vol. 121, p. 143901, Oct 2018.

[46] P. Gaal, K. Reimann, M. Woerner, T. Elsaesser, R. Hey, and K. H. Ploog, “Nonlinear terahertz response of n-type gaas,” *Phys. Rev. Lett.*, vol. 96, p. 187402, May 2006.

[47] X. Li, T. Qiu, J. Zhang, E. Baldini, J. Lu, A. M. Rappe, and K. A. Nelson, “Terahertz field-induced ferroelectricity in quantum paraelectric srtio3,” *Science*, vol. 364, no. 6445, pp. 1079–1082, 2019.

[48] F. Blanchard, J. E. Nkeck, L. Guiramand, S. Zibod, K. Dolgaleva, T. Arikawa, and K. Tanaka, “Two-dimensional space–time terahertz memory in bulksrtio3,” *Optica*, vol. 9, pp. 980–986, Sep 2022.

[49] P. Rasekh, A. Safari, M. Yildirim, R. Bhardwaj, J.-M. Ménard, K. Dolgaleva, and R. W. Boyd, “Terahertz nonlinear spectroscopy of water vapor,” *ACS Photonics*, vol. 8, no. 6, pp. 1683–1688, 2021.

[50] A. Tcypkin, M. Zhukova, M. Melnik, I. Vorontsova, M. Kulya, S. Putilin, S. Kozlov, S. Choudhary, and R. W. Boyd, “Giant third-order nonlinear response of liquids at terahertz frequencies,” *Phys. Rev. Applied*, vol. 15, p. 054009, May 2021.

[51] M. C. Hoffmann, N. C. Brandt, H. Y. Hwang, K.-L. Yeh, and K. A. Nelson, “Terahertz kerr effect,” *Applied Physics Letters*, vol. 95, no. 23, p. 231105, 2009.

[52] A. N. Tcypkin, M. V. Melnik, M. O. Zhukova, I. O. Vorontsova, S. E. Putilin, S. A. Kozlov, and X.-C. Zhang, “High kerr nonlinearity of water in thz spectral range,” *Opt. Express*, vol. 27, pp. 10419–10425, Apr 2019.

[53] K. J. G. Francis, M. L. P. Chong, Y. E, and X.-C. Zhang, “Terahertz nonlinear index extraction via full-phase analysis,” *Opt. Lett.*, vol. 45, pp. 5628–5631, Oct 2020.

[54] M. Zhang, W. Xiao, C. Zhang, and L. Zhang, “Terahertz kerr effect of liquids,” *Sensors*, vol. 22, no. 23, 2022.

[55] P. Zalden, L. Song, X. Wu, H. Huang, F. Ahr, O. D. Mücke, J. Reichert, M. Thorwart, P. K. Mishra, R. Welsch, R. Santra, F. X. Kärtner, and C. Bressler, “Molecular polarizability anisotropy of liquid water revealed by terahertz-induced transient orientation,” *Nature Communications*, vol. 9, p. 2142, May 2018.

[56] V. Balos, N. K. Kaliannan, H. Elgabarty, M. Wolf, T. D. Kühne, and M. Sajadi, “Time-resolved terahertz–raman spectroscopy reveals that cations and anions distinctly modify intermolecular interactions of water,” *Nature Chemistry*, vol. 14, pp. 1031–1037, Sep 2022.

[57] M. Zalkovskij, A. C. Strikwerda, K. Iwaszczuk, A. Popescu, D. Savastru, R. Malureanu, A. V. Lavrinenko, and P. U. Jepsen, “Terahertz-induced kerr effect in amorphous chalcogenide glasses,” *Applied Physics Letters*, vol. 103, no. 22, p. 221102, 2013.

[58] W.-Q. He, C.-M. Gu, and W.-Z. Shen, “Direct evidence of kerr-like nonlinearity by femtosecond z-scan technique,” *Opt. Express*, vol. 14, pp. 5476–5483, Jun 2006.

[59] M. Sajadi, M. Wolf, and T. Kampfrath, “Terahertz-field-induced optical birefringence in common window and substrate materials,” *Opt. Express*, vol. 23, pp. 28985–28992, Nov 2015.

[60] Y. Wei, J. Le, L. Huang, and C. Tian, “Efficient generation of intense broadband terahertz pulses from quartz,” *Applied Physics Letters*, vol. 122, 02 2023. 081105.

[61] V. Balos, M. Wolf, S. Kovalev, and M. Sajadi, “Optical rectification and electro-optic sampling in quartz,” *Opt. Express*, vol. 31, pp. 13317–13327, Apr 2023.

[62] K. Dolgaleva, D. V. Materikina, R. W. Boyd, and S. A. Kozlov, “Prediction of an extremely large nonlinear refractive index for crystals at terahertz frequencies,” *Phys. Rev. A*, vol. 92, p. 023809, Aug 2015.

[63] A. N. Tcypkin, S. E. Putilin, M. S. Kulya, M. Siddiqui, S. Choudhary, J. Zhao, V. G. Bespalov, R. Boyd, X. C. Zhang, and S. A. Kozlov, “Measurement of the nonlinear refractive index in znse crystal by modified methodof z-scan in the terahertz spectral range,” in *2017 42nd International Conference on Infrared, Millimeter, and Terahertz Waves (IRMMW-THz)*, pp. 1–1, 2017.

[64] M. Melnik, I. Vorontsova, S. Putilin, A. Tcypkin, and S. Kozlov, “Methodical inaccuracy of the z-scan method for few-cycle terahertz pulses,” *Scientific Reports*, vol. 9, p. 9146, Jun 2019.

[65] A. Couairon, E. Brambilla, T. Corti, D. Majus, O. de J. Ramírez-Góngora, and M. Kolesik, "Practitioner's guide to laser pulse propagation models and simulation," *The European Physical Journal Special Topics*, vol. 199, pp. 5–76, Nov 2011.

[66] A. A. Drozdov, S. A. Kozlov, A. A. Sukhorukov, and Y. S. Kivshar, "Self-phase modulation and frequency generation with few-cycle optical pulses in nonlinear dispersive media," *Phys. Rev. A*, vol. 86, p. 053822, Nov 2012.

[67] P. Rasekh, M. Saliminabi, M. Yildirim, R. W. Boyd, J.-M. Ménard, and K. Dolgaleva, "Propagation of broadband thz pulses: effects of dispersion, diffraction and time-varying nonlinear refraction," *Opt. Express*, vol. 28, pp. 3237–3248, Feb 2020.

[68] P. Rasekh, "Kerr effect at the THz frequencies," 2020.

[69] S. Bodrov, Y. Sergeev, E. Burova, A. Korytin, A. Murzanev, A. Romashkin, and A. Stepanov, "Cubic nonlinearity of tellurite and chalcogenide glasses: Terahertz-field-induced second harmonic generation vs. optical kerr effect," *Applied Sciences*, vol. 12, no. 22, 2022.

[70] K. J. G. Francis, M. L. P. Chong, Y. E, and X.-C. Zhang, "Terahertz nonlinear index extraction via full-phase analysis," *Opt. Lett.*, vol. 45, pp. 5628–5631, Oct 2020.

[71] S. B. Bodrov, Y. A. Sergeev, A. I. Korytin, and A. N. Stepanov, "Terahertz-field-induced second optical harmonic generation from si(111) surface," *Phys. Rev. B*, vol. 105, p. 035306, Jan 2022.

[72] A. Woldegeorgis, T. Kurihara, B. Beleites, J. Bossert, R. Grosse, G. G. Paulus, F. Ronneberger, and A. Gopal, "THz induced nonlinear effects in materials at intensities above 26 GW/cm2," *Journal of Infrared, Millimeter, and Terahertz Waves*, vol. 39, pp. 667–680, Apr. 2018.

[73] M. Cornet, J. Degert, E. Abraham, and E. Freysz, "Terahertz kerr effect in gallium phosphide crystal," *Journal of the Optical Society of America B*, vol. 31, p. 1648, June 2014.

[74] B. Zhou, M. Rasmussen, S. Zibod, S. Yan, N. K. Noori, O. Nagy, Y. Ding, S. J. Lange, K. Dolgaleva, R. W. Boyd, and P. U. Jepsen, "Measurement of the dispersion of $\chi(3)$ of SiO_2 and SiN across the thz and far-infrared frequency bands," *Laser & Photonics Reviews*, Jul 2024.

[75] C. L. Davies, J. B. Patel, C. Q. Xia, L. M. Herz, and M. B. Johnston, "Temperature-dependent refractive index of quartz at terahertz frequencies," *Journal of Infrared, Millimeter, and Terahertz Waves*, vol. 39, pp. 1236–1248, Dec 2018.

[76] C. J. Winta, S. Gewinner, W. Schöllkopf, M. Wolf, and A. Paarmann, "Second-harmonic phonon spectroscopy of α-quartz," *Phys. Rev. B*, vol. 97, p. 094108, Mar 2018.

[77] T. Brabec and F. Krausz, "Intense few-cycle laser fields: Frontiers of nonlinear optics," *Rev. Mod. Phys.*, vol. 72, pp. 545–591, Apr 2000.

[78] G. Agrawal, *Nonlinear Fiber Optics*. Quantum electronics–principles and applications, Elsevier Science, 2012.

[79] S. Zibod, P. Rasekh, M. Yildrim, W. Cui, R. Bhardwaj, J.-M. Ménard, R. W. Boyd, and K. Dolgaleva, "Strong nonlinear response in crystalline quartz at thz frequencies," *Advanced Optical Materials*, vol. 11, no. 15, p. 2202343, 2023.

[80] O. Wada, D. Ramachari, C.-S. Yang, T. Uchino, and C.-L. Pan, "High refractive index properties of oxyfluorosilicate glasses and a unified dielectric model of silicate oxide glasses in the sub-terahertz frequency region," *Opt. Mater. Express*, vol. 10, pp. 607–621, Feb 2020.

[81] M. Naftaly and R. E. Miles, "Terahertz time-domain spectroscopy of silicate glasses and the relationship to material properties," *Journal of Applied Physics*, vol. 102, p. 043517, 08 2007.

[82] N. J. Tostanoski and S. K. Sundaram, "Universal power-law of terahertz optical properties of borosilicate, tellurite, and chalcogenide glass families," *Scientific Reports*, vol. 13, Feb. 2023.

[83] A. Ravagli, M. Naftaly, C. Craig, E. Weatherby, and D. Hewak, "Dielectric and structural characterisation of chalcogenide glasses via terahertz time-domain spectroscopy," *Optical Materials*, vol. 69, pp. 339–343, 2017.

[84] D. Cook, J. Chen, E. Morlino, and R. Hochstrasser, "Terahertz-field-induced second-harmonic generation measurements of liquid dynamics," *Chemical Physics Letters*, vol. 309, no. 3, pp. 221–228, 1999.

[85] P. C. M. Planken, H.-K. Nienhuys, H. J. Bakker, and T. Wenckebach, "Measurement and calculation of the orientation dependence of terahertz pulse detection in znte," *J. Opt. Soc. Am. B*, vol. 18, pp. 313–317, Mar 2001.

[86] T. Wang, K. Iwaszczuk, E. A. Wrisberg, E. V. Denning, and P. U. Jepsen, "Linearity of air-biased coherent detection for terahertz time-domain spectroscopy," *J. Infrared Millim. Terahertz Waves*, vol. 37, pp. 592–604, June 2016.

[87] I.-C. Ho, X. Guo, and X.-C. Zhang, "Design and performance of reflective terahertz air-biased-coherent-detection for time-domain spectroscopy," *Opt. Express*, vol. 18, pp. 2872–2883, Feb 2010.

[88] A. Tomasino, R. Piccoli, Y. Jestin, S. Delprat, M. Chaker, M. Peccianti, M. Clerici, A. Busacca, L. Razzari, and R. Morandotti, "Invited Article: Ultra-broadband terahertz coherent detection via a silicon nitride-based deep subwavelength metallic slit," *APL Photonics*, vol. 3, p. 110805, 11 2018.

[89] A. Tomasino, A. Mazhorova, M. Clerici, M. Peccianti, S.-P. Ho, Y. Jestin, A. Pasquazi, A. Markov, X. Jin, R. Piccoli, S. Delprat, M. Chaker, A. Busacca, J. Ali, L. Razzari, and R. Morandotti, "Solid-state-biased coherent detection of ultra-broadband terahertz pulses," *Optica*, vol. 4, pp. 1358–1362, Nov 2017.

[90] A. Nguyen, K. J. Kaltenecker, J.-C. Delagnes, B. Zhou, E. Cormier, N. Fedorov, R. Bouillaud, D. Descamps, I. Thiele, S. Skupin, P. U. Jepsen, and L. Bergé, "Wavelength scaling of terahertz pulse energies delivered by two-color air plasmas," *Opt. Lett.*, vol. 44, pp. 1488–1491, Mar 2019.

[91] M. Clerici, M. Peccianti, B. E. Schmidt, L. Caspani, M. Shalaby, M. Giguère, A. Lotti, A. Couairon, F. m. c. Légaré, T. Ozaki, D. Faccio, and R. Morandotti, "Wavelength scaling of terahertz generation by gas ionization," *Phys. Rev. Lett.*, vol. 110, p. 253901, Jun 2013.

[92] R. W. Boyd, *Nonlinear optics*. Academic Press is an imprint of Elsevier, 2020.

[93] M. N. Polyanskiy, "Refractiveindex.info database of optical constants," *Scientific Data*, vol. 11, p. 94, Jan. 2024.

[94] J. Chochol, K. Postava, M. Čada, M. Vanwolleghem, M. Mičica, L. Halagačka, J.-F. Lampin, and J. Pištora, "Plasmonic behavior of iii-v semiconductors in far-infrared and terahertz range," *Journal of the European Optical Society-Rapid Publications*, vol. 13, May 2017.

[95] S. Maier, *Plasmonics - Fundamentals and Applications*. Springer, 2007.

[96] T.-I. Jeon and D. Grischkowsky, "Characterization of optically dense, doped semiconductors by reflection THz time domain spectroscopy," *Applied Physics Letters*, vol. 72, pp. 3032–3034, 06 1998.

[97] K. Dolgaleva and R. W. Boyd, "Local-field effects in nanostructured photonic materials," *Adv. Opt. Photon.*, vol. 4, pp. 1–77, Mar 2012.

[98] W. Cai and V. Shalaev, *Optical Metamaterials*. Springer New York, 2010.

[99] G. A. Niklasson, C. G. Granqvist, and O. Hunderi, "Effective medium models for the optical properties of inhomogeneous materials," *Appl. Opt.*, vol. 20, pp. 26–30, Jan 1981.

[100] R. J. Gehr and R. W. Boyd, "Optical properties of nanostructured optical materials," *Chemistry of Materials*, vol. 8, no. 8, pp. 1807–1819, 1996.

[101] R. S. Bennink, Y.-K. Yoon, R. W. Boyd, and J. E. Sipe, "Accessing the optical nonlinearity of metals with metal–dielectric photonic bandgap structures," *Opt. Lett.*, vol. 24, pp. 1416–1418, Oct 1999.

[102] D. R. Smith, D. C. Vier, T. Koschny, and C. M. Soukoulis, "Electromagnetic parameter retrieval from inhomogeneous metamaterials," *Phys. Rev. E*, vol. 71, p. 036617, Mar 2005.

[103] S. Suresh, O. Reshef, M. Z. Alam, J. Upham, M. Karimi, and R. W. Boyd, "Enhanced nonlinear optical responses of layered epsilon-near-zero metamaterials at visible frequencies," *ACS Photonics*, vol. 8, no. 1, pp. 125–129, 2021.

Appendix

THz Kerr vs THz n_2

We provide a theoretical model to express the relation between the THz-induced third-order susceptibility corresponding to self-action effects and third-order susceptibility corresponding to THz -induced Kerr effect.

Theoretical model:

The theoretical modeling starts with anharmonic oscillator as described in Ref. : [62]

$$\ddot{x} + 2\gamma\dot{x} + \omega_0^2 x + ax^2 + bx^3 = \alpha E(t), \tag{6.13}$$

where x is the ion displacement from the equilibrium position, γ is damping factor, ω_0 is the resonance frequency, $E(t)$ is the applied field and a and b are the second- and third-order nonlinear coefficients, respectively. For simplicity, we assume there is a dominant resonance at 37.2 THz. The parameter α on the right-hand side of Equation (6.13) is determined as $\alpha = q/m$, where q and m are the effective electric coupling strength and effective reduced mass of the mode, respectively. We assume that the applied field is given by

$$E(t) = E_{THz}e^{-i\omega_{THz}t} + E_{Opt}e^{-i\omega_{Opt}t} + c.c.. \tag{6.14}$$

where the field has two frequency components, one in THz range and the other in the optical range. Applying perturbation theory and introducing the expansion parameter $0 \le \lambda \le 1$, we seek a solution to Equation (6.13) in the form of power series of λ.

$$x(t) = \lambda x^{(1)}(t) + \lambda^2 x^{(2)}(t) + \lambda^3 x^{(3)}(t) + \cdots \tag{6.15}$$

where the first-order, second-order and third-order ion deviation are given as [92]:

$$x^{(1)}(t) = x^{(1)}(\omega_{THz})e^{-i\omega_{THz}t} + x^{(1)}(\omega_{Opt})e^{-i\omega_{Opt}t} + c.c., \tag{6.16a}$$

$$x^{(2)}(t) = \sum_p x^{(2)}(\omega_p)e^{-i\omega_p t} + c.c., \tag{6.16b}$$

$$x^{(3)}(t) = \sum_q x^{(3)}(\omega_q)e^{-i\omega_q t} + c.c., \tag{6.16c}$$

respectively. The second-order correction term oscillation has frequencies denoted by $\omega_p = \omega_j + \omega_k$, where ω_j and ω_k would take any values of $\pm\ \omega_{THz}$ and $\pm\ \omega_{Opt}$. In the same manner, $\omega_q = \omega_l + \omega_m + \omega_n$ is the oscillation frequency of the third-order correction term, where $\omega_l,\ \omega_m$ and $\omega_n$would take any values of $\pm\ \omega_{THz}$ and $\pm\ \omega_{Opt}$. After substituting x in Equation (6.13), we sort and split the terms with respect to the power of λ into three equations:

$$\ddot{x}^{(1)} + 2\gamma\dot{x}^{(1)} + \omega_0^2 x^{(1)} = \alpha E, \tag{6.17a}$$

$$\ddot{x}^{(2)} + 2\gamma\dot{x}^{(2)} + \omega_0^2 x^{(2)} + a[x^{(1)}]^2 = 0, \tag{6.17b}$$

$$\ddot{x}^{(3)} + 2\gamma\dot{x}^{(3)} + \omega_0^2 x^{(3)} + 2ax^{(1)}x^{(2)} + b[x^{(1)}]^3 = 0. \tag{6.17c}$$

Equation (4.5a) gives the steady-state solution at the fundamental frequencies in the form :

$$x^{(1)}(\omega_{THz}) = \frac{\alpha E_{THz}}{\omega_0^2 - \omega_{THz}^2 - 2i\gamma\omega_{THz}} \tag{6.18a}$$

$$x^{(1)}(\omega_{Opt}) = \frac{\alpha E_{Opt}}{\omega_0^2 - \omega_{Opt}^2 - 2i\gamma\omega_{Opt}} \tag{6.18b}$$

Substituting Equations (4.6a and 4.6b) in Equation (4.5b), we find the second-order correction terms for the components oscillating at the frequencies $2\omega_{THz}$ and $2\omega_{Opt}$:

$$x^{(2)}(2\omega_{THz}) = -\frac{a\alpha^2 E_{THz}^2}{(\omega_0^2 - \omega_{THz}^2 - 2i\gamma\omega_{THz})^2(\omega_0^2 - 4\omega_{THz}^2 - 4i\gamma\omega_{THz})} \tag{6.19a}$$

$$x^{(2)}(2\omega_{Opt}) = -\frac{a\alpha^2 E_{Opt}^2}{(\omega_0^2 - \omega_{Opt}^2 - 2i\gamma\omega_{Opt})^2(\omega_0^2 - 4\omega_{Opt}^2 - 4i\gamma\omega_{Opt})} \tag{6.19b}$$

The optical rectification terms at frequency 0 induced by THz and optical beams are obtained as:

$$x^{(2)}(0, \omega_{THz}, -\omega_{THz}) = -2\frac{a\alpha^2 E_{THz}^2}{(\omega_0^2 - \omega_{THz}^2 - 2i\gamma\omega_{THz})(\omega_0^2 - \omega_{THz}^2 + 2i\gamma\omega_{THz})\omega_0^2}, \tag{6.20a}$$

$$x^{(2)}(0, \omega_{Opt}, -\omega_{Opt}) = -2\frac{a\alpha^2 E_{Opt}^2}{(\omega_0^2 - \omega_{Opt}^2 - 2i\gamma\omega_{Opt})(\omega_0^2 - \omega_{Opt}^2 + 2i\gamma\omega_{Opt})\omega_0^2}. \tag{6.20b}$$

Finally, the solution at frequencies $\omega_{Opt} \pm \omega_{THz}$ is given by:

$$x^{(2)}(\omega_{Opt} \pm \omega_{THz}) = -2\frac{a\alpha^2 E_{Opt}E_{THz}}{(\omega_0^2 - \omega_{Opt}^2 - 2i\gamma\omega_{Opt})^2(\omega_0^2 - \omega_{THz}^2 \mp 2i\gamma\omega_{THz})}, \tag{6.21}$$

where the approximation $\omega_{Opt} \pm \omega_{THz} \approx \omega_{Opt}$ is used.

Knowing all the second-order correction terms, we could plug $x^{(2)}(t)$ into Equation (6.17c) and find the third-order correction-terms. There are many frequency components resulting from the third-order processes described in Equation (6.17c). However, there are two frequenies of direct interest in this study, ω_{THz} :

$$\begin{aligned} x^{(3)}(\omega_{THz}) = \Bigg[& \frac{2a^2\alpha^3}{(\omega_0^2 - \omega_{THz}^2 - 2i\gamma\omega_{THz})^3(\omega_0^2 - \omega_{THz}^2 + 2i\gamma\omega_{THz})} \frac{(3\omega_0^2 - 8\omega_{THz}^2 - 8i\gamma\omega_{THz})}{\omega_0^2(\omega_0^2 - 4\omega_{THz}^2 - 4i\gamma\omega_{THz})} \\ & + \frac{3b\alpha^3}{(\omega_0^2 - \omega_{THz}^2 - 2i\gamma\omega_{THz})^3(\omega_0^2 - \omega_{THz}^2 + 2i\gamma\omega_{THz})} \Bigg] |E_{THz}|^2 E_{THz} \end{aligned} \tag{6.22}$$

and ω_{Opt}:

$$\begin{aligned} x^{(3)}(\omega_{Opt}) = \Bigg[& \frac{4a^2\alpha^3}{(\omega_0^2 - \omega_{THz}^2 - 2i\gamma\omega_{THz})(\omega_0^2 - \omega_{THz}^2 + 2i\gamma\omega_{THz})\omega_0^2} \frac{(2\omega_0^2 - \omega_{Opt}^2 - 2i\gamma\omega_{Opt})}{(\omega_0^2 - \omega_{Opt}^2 - 2i\gamma\omega_{Opt})^3} \\ & + \frac{3b\alpha^3}{(\omega_0^2 - \omega_{THz}^2 - 2i\gamma\omega_{THz})(\omega_0^2 - \omega_{THz}^2 + 2i\gamma\omega_{THz})(\omega_0^2 - \omega_{Opt}^2 - 2i\gamma\omega_{Opt})^2} \Bigg] |E_{THz}|^2 E_{Opt} \end{aligned} \tag{6.23}$$

In Equation (6.22) the first bracket represents the THz-induced correction term, while the second bracket shows the optically induced nonlinear term, which could be ignored with controlling the intensity of probe beam. The relation between nonlinear susceptibility and deviation is given by

$$P_{NL} = Nqx^{(3)} = 3\chi^{(3)}|E|^2 E. \tag{6.24}$$

Thus, the nonlinear susceptibility is expressed as :

$$\chi^{(3)}(\omega_{THz},\omega_{THz},-\omega_{THz},\omega_{THz}) = \frac{qN}{3}\frac{\alpha^3}{(\omega_0^2-\omega_{THz}^2-2i\gamma\omega_{THz})^3(\omega_0^2-\omega_{THz}^2+2i\gamma\omega_{THz})} \tag{6.25}$$

$$\left[2a^2\frac{(3\omega_0^2-8\omega_{THz}^2-8i\gamma\omega_{THz})}{\omega_0^2(\omega_0^2-4\omega_{THz}^2-4i\gamma\omega_{THz})}+3b\right]$$

The calculation for a is straightforward, as presented in Ref.[62] The direct process contribution to the susceptibility at low frequencies is given as:

$$\chi_{Direct}^{(3),\omega\ll\omega_0} = -\frac{qN}{3}\frac{3b\alpha^3}{\omega_0^8} = \frac{1}{\frac{3\pi}{n_0}}n_{2,v}^{(2)} = -\frac{1}{\frac{3\pi}{n_0}}\frac{3\pi}{n_0}\frac{2N|\mu|^4}{3\hbar^3\omega_0^3} = \frac{2N|\mu|^4}{3\hbar^3\omega_0^3}, \tag{6.26}$$

where dipole moment μ is related to linear susceptibility via:[92]

$$\chi^{(1)} = \frac{N}{3\hbar}\sum_n|\mu_n a|^2\left[\frac{1}{(\omega_{na}-\omega)-i\gamma}+\frac{1}{(\omega_{na}+\omega)+i\gamma}\right] \tag{6.27}$$

In the low frequency regime, the Equation (4.15) is simplified into

$$\chi^{(1),\omega\ll\omega_0} = \frac{2N|\mu|^2}{3\hbar\omega_0} \tag{6.28}$$

Plugging (6.28) into (6.25), and replacing $\chi^{(1),\omega\ll\omega_0}$ with $\frac{1}{4\pi}\left[(n_0^{\omega\ll\omega_0})^2-1\right]$, where $n_0^{\omega\ll\omega_0}$ is calculated as presented in Ref.[62], we have:

$$\chi_{Direct}^{(3),\omega\ll\omega_0} = -\frac{qN}{3}\frac{3b\alpha^3}{\omega_0^8} = \frac{3(\chi^{(1),\omega\ll\omega_0})^2}{2N\hbar\omega_0} = -\frac{3\left[(n_0^{\omega\ll\omega_0})^2-1\right]^2}{2N\hbar\omega_0(4\pi)^2} = -\frac{3\left[(n_0^{\omega\ll\omega_0})^2-1\right]^2}{32N\hbar\omega_0\pi^2}, \tag{6.29}$$

For THz frequencies $\omega_{THz} \ll \omega_0$, the ratio between the direct process (second) and cascaded process (first) terms in the first bracket is given as:

$$\frac{\chi^{(3)}(\omega_{THz})_{Direct}}{\chi^{(3)}(\omega_{THz})_{Cascaded}} = \frac{3b}{2a^2}\frac{\omega_0^2(\omega_0^2-4\omega_{THz}^2-4i\gamma\omega_{THz})}{(3\omega_0^2-8\omega_{THz}^2-8i\gamma\omega_{THz})}\Bigg|_{(\omega_{THz}\ll\omega_0)} = \frac{b\omega_0^2}{2a^2} = \frac{-3.27\times10^{-11}}{2.24\times10^{-9}} \approx -0.015, \tag{6.30}$$

meaning that at THz frequencies $\omega_{THz} \ll \omega_0$, the direct contribution could be neglected with respect to cascaded process. However, for the frequencies close to the resonance frequency, we need to derive a frequency-dependent expression for the direct contribution. Equation (6.27) has the general form of:

$$\chi^{(1)}(\omega) = \frac{2N|\mu|^2\omega_0}{3\hbar(\omega_0^2-\omega^2-2i\gamma\omega)} = \chi^{(1),\omega\ll\omega_0}\frac{\omega_0^2}{(\omega_0^2-\omega^2-2i\gamma\omega)} = \frac{1}{4\pi}\left[(n_0^{\omega\ll\omega_0})^2-1\right]\frac{\omega_0^2}{(\omega_0^2-\omega^2-2i\gamma\omega)} \tag{6.31}$$

Substituting Equation (6.31), into Equation(6.29), we obtain:

$$(\frac{qN}{3})3b\alpha^3 = -\frac{3(\chi^{(1),\omega\ll\omega_0})^2}{2N\hbar\omega_0} = -\frac{3\big[(n_0^{\omega\ll\omega_0})^2-1\big]^2}{32N\hbar\pi^2}\frac{\omega_0^{11}}{(\omega_0^2-\omega^2-2i\gamma\omega)^2}, \tag{6.32}$$

Substituting Equation (6.32) into Equation (6.25), the third-order susceptibility as a function of frequency is calculated as:

$$\begin{aligned}\chi^{(3)}(\omega_{THz},\omega_{THz},-\omega_{THz},\omega_{THz}) &= \frac{1}{(\omega_0^2-\omega_{THz}^2-2i\gamma\omega_{THz})^3(\omega_0^2-\omega_{THz}^2+2i\gamma\omega_{THz})} \\ &\left[\frac{qN\alpha^3}{3}\times 2a^2\frac{(3\omega_0^2-8\omega_{THz}^2-8i\gamma\omega_{THz})}{\omega_0^2(\omega_0^2-4\omega_{THz}^2-4i\gamma\omega_{THz})}+\frac{qN\alpha^3}{3}\times 3b\right] \\ &= \frac{1}{(\omega_0^2-\omega_{THz}^2-2i\gamma\omega_{THz})^3(\omega_0^2-\omega_{THz}^2+2i\gamma\omega_{THz})} \\ &\left[\frac{qN\alpha^3}{3}\times 2a^2\frac{(3\omega_0^2-8\omega_{THz}^2-8i\gamma\omega_{THz})}{\omega_0^2(\omega_0^2-4\omega_{THz}^2-4i\gamma\omega_{THz})}-\frac{3\big[(n_0^{\omega\ll\omega_0})^2-1\big]^2}{32N\hbar\pi^2}\frac{\omega_0^{11}}{(\omega_0^2-\omega^2-2i\gamma\omega)^2}\right]\end{aligned} \tag{6.33}$$

Now, using Equations (6.23) and (6.32), the nonlinear susceptibility corresponding to THz field induced Kerr- effect is given by:

$$
\begin{aligned}
\chi^{(3)}(\omega_{Opt},\omega_{Opt},-\omega_{THz},\omega_{THz}) = \Bigg[& \frac{qN}{3}\frac{4a^2\alpha^3}{(\omega_0^2-\omega_{THz}^2-2i\gamma\omega_{THz})(\omega_0^2-\omega_{THz}^2+2i\gamma\omega_{THz})\omega_0^2} \\
& \frac{(2\omega_0^2-\omega_{Opt}^2-2i\gamma\omega_{Opt})}{(\omega_0^2-\omega_{Opt}^2-2i\gamma\omega_{Opt})^3} \\
& +\frac{qN}{3}\frac{3b\alpha^3}{(\omega_0^2-\omega_{THz}^2-2i\gamma\omega_{THz})(\omega_0^2-\omega_{THz}^2+2i\gamma\omega_{THz})(\omega_0^2-\omega_{Opt}^2-2i\gamma\omega_{Opt})^2}\Bigg] = \\
& \Bigg[\frac{qN}{3}\frac{4a^2\alpha^3}{(\omega_0^2-\omega_{THz}^2-2i\gamma\omega_{THz})(\omega_0^2-\omega_{THz}^2+2i\gamma\omega_{THz})\omega_0^2}\frac{1}{\omega_{Opt}^4} \\
& -\frac{3\big[(n_0^{\omega\ll\omega_0})^2-1\big]^2}{32N\hbar\pi^2}\frac{\omega_0^{11}}{(\omega_0^2-\omega_{THz}^2-2i\gamma\omega_{THz})^3}\frac{1}{\omega_{Opt}^4(\omega_0^2-\omega_{THz}^2+2i\gamma\omega_{THz})}\Bigg]
\end{aligned}
\tag{6.34}
$$